Fiber tracking and fiber architecture description in cardiac DT-MRI

Hongying Li

Numéro d'ordre : 2013-???-???

Année 2013

THÈSE

Délivrée par

L'INSTITUT NATIONAL DE SCIENCES APPLIQUÉES DE LYON
Spécialité : Image et systèmes

DIPLÔME DE DOCTORAT

(arrêté du 7 aout 2006)

ÉCOLE DOCTORALE : ÉLECTRONIQUE, ÉLECTROTECHNIQUE, AUTOMATIQUE

Soutenue publiquement le 21/11/2013 par

Hongying LI

Fiber tracking and fiber architecture description in cardiac DT-MRI

Jury

Nicole VINCENT	Professeur, Université Paris Descartes	Rapporteur
Michel DESVIGNES	Professeur, Grenoble-INP	Rapporteur
Pierre-Simon JOUK	Professeur, CHU de Grenoble	Examinateur
Yves USSON	Chargé de recherche, CNRS	Examinateur
Pierre CROISILLE	Professeur - Praticien Hospitalier, CHU St-Etienne	Examinateur
Isabelle E. MAGNIN	Directeur de recherche INSERM	Examinateur
Marc ROBINI	Maître de Conférences, INSA de Lyon	Co-directeur de thèse
Yue-Min ZHU	Directeur de Recherche, CNRS	Directeur de thèse

Résumé

La connaissance de l'architecture tridimensionnelle (3D) des fibres est cruciale dans la compréhension de la fonction du cœur humain. L'imagerie par résonance magnétique du tenseur de diffusion (IRM-DT) est une technique permettant de mesurer la diffusion des molécules d'eau dans des tissus humains, et donc d'étudier de manière non-invasive l'architecture 3D des fibres du cœur humain. Dans l'IRM-TD cardiaque, la tractographie des fibres est essentielle pour représenter et visualiser l'architecture des fibres, mais souvent utilisée qualitativement comme une dernière étape qui consiste à visualiser sur l'écran l'architecture myocardique obtenue à partir des données IRM-TD. Cependant, cette visualisation qualitative n'est pas suffisante pour décrire de manière objective et complète l'architecture des fibres. L'objectif de cette thèse est de développer de nouvelles approches pour la tractographie et pour la description quantitative de l'architecture des fibres cardiaques du cœur humain en IRM-TD cardiaque.

Les travaux de cette thèse se focalisent sur trois axes. Le premier est le développement d'un algorithme de tractographie probabiliste, qui prend en compte la corrélation spatiale des fibres pendant le suivi des fibres myocardiques. Les résultats expérimentaux montrent que la méthode proposée est robuste au bruit. Les fibres produites sont plus régulières et plus lisses, et la configuration des fibres cardiaques est plus facile à observer. Le second axe concerne une nouvelle notion de dépliement de fibres pour décrire les fibres du cœur humain, qui sont souvent complexes dans l'espace 3D. L'idée est d'analyser cette architecture 3D dans un espace réduit à deux dimensions (2D), en utilisant une technique d'apprentissage de variété. L'approche de dépliement proposée permet la description quantitative de l'architecture 3D de fibres cardiaques dans un plan 2D. Les résultats montrent qu'il est beaucoup plus facile d'observer et d'étudier les caractéristiques des fibres cardiaques après les avoir dépliées, et qu'il semble exister des formes de fibres caractéristiques du cœur humain. Le dernier axe consiste en la fusion de fibres, qui est obtenue en moyennant les fibres selon une grille. Cette approche fournit des architectures de fibres simplifiée à différentes échelles, et permet de mieux mettre en évidence la configuration des fibres cardiaques.

Abstract

It is important to study the cardiac fiber architecture in order to understand the heart function. Diffusion tensor MRI (DT-MRI) is the only noninvasive technique that allows studying cardiac fiber architecture in vivo. Tractography is essential in representing and visualizing cardiac fiber architecture in DT-MRI, but is often employed qualitatively.

The motivation of this thesis is to develop technique for studying the cardiac fiber architecture from the fiber tracts provided by the tractography process in cardiac DT-MRI. Our goal is to develop tractography algorithm and approaches for the quantitative description of cardiac fiber architecture.

My work is composed of three main axis. The first is the development of a probabilistic tractography algorithm, which takes fiber spatial correlation into accounts in tracing fibers. Experimental results show that the proposed method is meaningfully more robust to noise than the streamlining method, and produces more regular and smoother fibers,

which enables cardiac fiber configurations to be more clearly observed. The second concerns a new framework, namely cardiac fiber unfolding, which is an isometric mapping. Our fiber unfolding framework allows the quantitative description of three dimensional cardiac fiber architecture in a two dimensional plan. Our experimental results show that fiber tract pattern can be observed much easier by unfolding them in a plane, and several cardiac fiber patterns were found. The last axis consists in merging fibers, which is achieved by averaging fibers according to a grid. This fiber merging approach provide simplified fiber architecture at different scale as output that highlights the cardiac fiber configuration.

INSA Direction de la Recherche - Ecoles Doctorales – Quinquennal 2011-2015

SIGLE	ECOLE DOCTORALE	NOM ET COORDONNEES DU RESPONSABLE
CHIMIE	**CHIMIE DE LYON** **http://www.edchimie-lyon.fr** Insa : R. GOURDON	M. Jean Marc LANCELIN Université de Lyon – Collège Doctoral Bât ESCPE 43 bd du 11 novembre 1918 69622 VILLEURBANNE Cedex Tél : 04.72.43 13 95 directeur@edchimie-lyon.fr
E.E.A.	**ELECTRONIQUE, ELECTROTECHNIQUE, AUTOMATIQUE** **http://edeea.ec-lyon.fr** Secrétariat : M.C. HAVGOUDOUKIAN eea@ec-lyon.fr	M. Gérard SCORLETTI Ecole Centrale de Lyon 36 avenue Guy de Collongue 69134 ECULLY Tél : 04.72.18 60 97 Fax : 04 78 43 37 17 Gerard.scorletti@ec-lyon.fr
E2M2	**EVOLUTION, ECOSYSTEME, MICROBIOLOGIE, MODELISATION** **http://e2m2.universite-lyon.fr** Insa : H. CHARLES	Mme Gudrun BORNETTE CNRS UMR 5023 LEHNA Université Claude Bernard Lyon 1 Bât Forel 43 bd du 11 novembre 1918 69622 VILLEURBANNE Cédex Tél : 04.72.43.12.94 e2m2@biomserv.univ-lyon1.fr
EDISS	**INTERDISCIPLINAIRE SCIENCES-SANTE** **http://ww2.ibcp.fr/ediss** Sec : Safia AIT CHALAL Insa : M. LAGARDE	M. Didier REVEL Hôpital Louis Pradel Bâtiment Central 28 Avenue Doyen Lépine 69677 BRON Tél : 04.72.68 49 09 Fax :04 72 35 49 16 Didier.revel@creatis.uni-lyon1.fr
INFOMATHS	**INFORMATIQUE ET MATHEMATIQUES** http://infomaths.univ-lyon1.fr	M. Johannes KELLENDONK Université Claude Bernard Lyon 1 INFOMATHS Bâtiment Braconnier 43 bd du 11 novembre 1918 69622 VILLEURBANNE Cedex Tél : 04.72. 44.82.94 Fax 04 72 43 16 87 infomaths@univ-lyon1.fr
Matériaux	**MATERIAUX DE LYON** Secrétariat : M. LABOUNE PM : 71.70 –Fax : 87.12 Bat. Saint Exupéry Ed.materiaux@insa-lyon.fr	M. Jean-Yves BUFFIERE INSA de Lyon MATEIS Bâtiment Saint Exupéry 7 avenue Jean Capelle 69621 VILLEURBANNE Cédex Tél : 04.72.43 83 18 Fax 04 72 43 85 28 Jean-yves.buffiere@insa-lyon.fr
MEGA	**MECANIQUE, ENERGETIQUE, GENIE CIVIL, ACOUSTIQUE** Secrétariat : M. LABOUNE PM : 71.70 –Fax : 87.12 Bat. Saint Exupéry mega@insa-lyon.fr	M. Philippe BOISSE INSA de Lyon Laboratoire LAMCOS Bâtiment Jacquard 25 bis avenue Jean Capelle 69621 VILLEURBANNE Cedex Tél :04.72.43.71.70 Fax : 04 72 43 72 37 Philippe.boisse@insa-lyon.fr
ScSo	**ScSo*** M. OBADIA Lionel Sec : Viviane POLSINELLI Insa : J.Y. TOUSSAINT	M. OBADIA Lionel Université Lyon 2 86 rue Pasteur 69365 LYON Cedex 07 Tél : 04.78.69.72.76 Fax : 04.37.28.04.48 Lionel.Obadia@univ-lyon2.fr

*ScSo : Histoire, Geographie, Aménagement, Urbanisme, Archéologie, Science politique, Sociologie, Anthropologie

Contents

I Background

Chapter 1

Introduction

1.1 Importance of cardiovascular diseases

Cardiovascular disease (CVD) is a class of disease that affects the cardiovascular system, and is a leading cause of death in the world. An estimated 17.3 million people died from CVDs in 2008, representing 30% of all global deaths. Over 80% of CVD deaths take place in low- and middle-income countries [Organization (2011)]. The number of people who die from CVDs, mainly from heart disease and stroke, will increase to reach 23.3 million by 2030 [Organization (2011), Mathers and Loncar (2006)].

Cardiovascular diseases are not only a cause of mortality, but also a cause of morbidity (diseased state, disability, or poor health). As a result, high incident cardiovascular diseases is a major financial burden. For instance, in European Union (EU), overall CVD is estimated to cost the EU economy almost €196 billion a year. Of the total cost of CVD in the EU, around 54% is due to direct health care costs, 24% to productivity losses and 22% to the informal care of people with CVD [Nichols *et al.* (2012)].

Cardiac function is achieved by the contraction of cardiac muscle fibers, and involves the propagation of electrical impulse in the heart conduction system in the cardiac muscles. The spatial organization of the myocardial muscle fibers appears to be a fundamental property of the heart underlying global and segmental contractile function. A heart disease usually accompanies changes in cardiac muscles. An alteration of the anatomy of the heart due to a disease or therapy can lead to impaired heart function. Thus it is essential and

important to develop techniques that allow a better understanding of the structures and functions of the normal and pathological hearts in order to prevent, detect and treat cardiovascular diseases.

1.2 Towards a better understanding of the cardiac fiber architecture

In the early stage of learning heart anatomy and function, investigations are made mainly in histological dissection. At present, many modalities such as MRI, ultrasound imaging or X-ray imaging, provides extensive information on the anatomy and function of the heart. Among these imaging modalities, diffusion MRI is the only noninvasive investigation technique that allows the description of cardiac fiber architecture in vivo.

In diffusion MRI, tractography algorithms aim to find paths through the data field along which diffusion is least hindered, and reconstruct fiber tracts by assuming that the water diffusion direction is aligned with the direction of oriented tissues. It is the only noninvasive tool for identifying and measuring these pathways in vivo.

However, most recent studies in diffusion MRI focused on the development of algorithms to reconstruct myocardial fiber tracts from diffusion-weighted images; the tractography has been used qualitatively. There are few studies on the post processing of the reconstructed fiber tracts, such as the description of cardiac fiber architecture from these fiber tracts.

1.3 Overview and contributions

The research work presented in this thesis deals with the tracking of cardiac fibers and the description of cardiac fiber architecture.

Chapter 2 and 3 make up the context part of this work.

Chapter 2 *"Heart anatomy and DT-MRI"* describes the cardiovascular system and the cardiac models proposed in the literature. Then we introduce some cardiac imaging techniques that give access to information about the heart anatomy and function. We particularly focus more on diffusion tensor imaging, which is employed in our work to characterize cardiac fiber architecture.

Chapter 3 *"The state of the art of tractography and cardiac fiber architecture description"* presents existing tractography techniques and existing voxel-wise and fiber-wise cardiac fiber architecture description techniques in DT-MRI.

Chapter 4 to 6 constitute the contribution part of this work, and are followed by Chapter 7 addressing the conclusion and perspectives.

Chapter 4 *"A neighborhood-based probabilistic approach for fiber tracking in human cardiac DTI"* presents a probabilistic tractography technique, which takes fiber spatial correlation into accounts when tracking fibers. Experimental results show that the proposed method is significantly more robust to noise than the streamlining method, and that it produces more regular and smoother fibers, which enables cardiac fiber configurations to be more clearly observed.

Chapter 5 *"Cardiac fiber unfolding by manifold learning"* addresses a new framework for the analysis of cardiac fiber architecture, namely cardiac fiber unfolding. The unfolding is an isometric mapping and is performed by manifold leaning. Our fiber unfolding framework allows the quantitative description of three dimensional cardiac fiber architecture in a two-dimensional plan. The experimental results show that fiber tract pattern can be observed much easier by unfolding them onto a plane, and several cardiac fiber patterns were found.

Chapter 6 *"Towards a simplified cardiac fiber architecture - multiscale fiber merging"* describes a fiber architecture simplification approach, which is achieved by averaging fibers according to a grid. This fiber merging approach can provide simplified fiber architecture that highlights the cardiac fiber configuration at different scales.

Chapter 7 *"Conclusion and perspectives"* summarizes the contributions followed by the perspectives of the research work presented in this thesis.

Chapter 2

Heart anatomy and DT-MRI

2.1 Résumé

Le cœur est l'un des organes les plus importants du corps humain. Il sert la pompe musculaire qui distribue le sang dans tout le corps. Cette fonction cardiaque est obtenue par la contraction des fibres musculaires cardiaques, et il s'agit de la propagation de l'impulsion électrique dans le système de conduction cardiaque dans les muscles cardiaques.

Pour comprendre comment la structure du cœur influe sur ses caractéristiques électriques et mécaniques fonction, il est nécessaire de savoir l'architecture des fibres cardiaques, i.e., l'arrangement tridimensionnel de cardiomyocytes et la hiérarchie des tissus cardiaques.

Dans ce chapitre, nous présentons brièvement quelques modèles cardiaques existant dans la littérature, et des techniques d'imageries communes qui permettent l'étude de la structure du cœur. Nous concentrons plus particulièrement sur l'imagerie du tenseur de diffusion, qui est utilisée dans notre travail.

2.2 Abstract

Heart is one of the most important organs in the human body. Heart serves as a muscular pump that distributes blood throughout the body. This cardiac function is achieved by the contraction of cardiac muscle fibers, and involves the propagation of electrical impulse

in the heart conduction system in the cardiac muscles.

To understand how the structure of the heart influences its electrical and mechanical function, it is necessary to obtain detailed information about the cardiac fiber architecture, i.e., the three-dimensional arrangement of cardiomyocytes and the associated connective tissue hierarchy throughout the heart wall.

In this chapter, we briefly present some cardiac models reported in the literature of anatomical studies, and introduce most common imaging techniques that allow the observation of the heart anatomy and structure. We particularly focus more on diffusion tensor imaging, which is employed in our work for characterizing cardiac fiber architecture.

2.3 Human heart anatomy

2.3.1 Macroscopic level and function

The heart is a muscular pump that distributes blood throughout the body. Healthy adult human heart is about the size of a clenched fist, and has a mass of between 250 and 350 grams. It is located in the thorax, behind and slightly left of the breastbone, and with lungs on its left and right sides. The heart is surrounded by a sac called the pericardium. The pericardium protects the heart and anchors it to the surrounding structures. The pericardium is double-walled, and have two layers. Between the two layers, it is filled with fluid known as pericardium fluid, which allow them to slide easily without friction when the heart moves.

The heart is usually divided into four chambers (see Fig. 2.1): the two upper chambers of the heart are receiving chambers, and are called atrium; the bottom chambers are discharging chambers, and are called ventricles. The two right chambers, the right atrium (RA) and the right ventricle (RV), together are referred to as the right heart, and the two left chambers, the left atrium (LA) and left ventricle (LV), as the left heart. Each ventricle has a inlet valve and an outlet valve. These four valves ensure that blood flow travels through the heart only in one direction.

Fig. 2.2 shows the blood circulation in the human body.

2.3.2 Electrical conduction system of the heart

In the cardiovascular system, the heart serves as a muscular pump that makes blood flow. This cardiac function is achieved by the contraction of cardiac muscle fibers, which involves the propagation of electrical impulse in the heart conduction system and in the cardiac muscles.

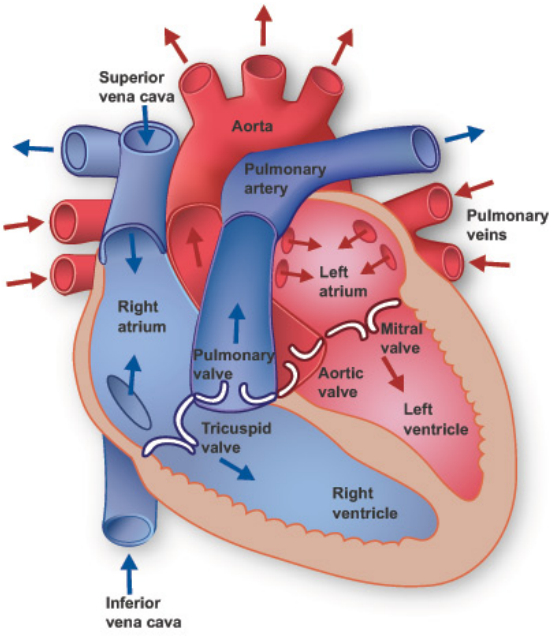

Figure 2.1: Anatomy of the human heart. De-oxygenated blood flows in the components colored in blue, the right ventricle, the right atrium, the superior vena cava and the pulmonary artery. Oxygenated blood flows in the components colored in red, the left ventricle, the left atrium, the pulmonary veins and the aorta. The single blood flow direction though the chambers is indicated by the arrows in the diagram, and is ensured by the valves. (From Texas Heart Institute Heart Information Center, http://www.texasheartinstitute.org/hic/anatomy/anatomy2.cfm.)

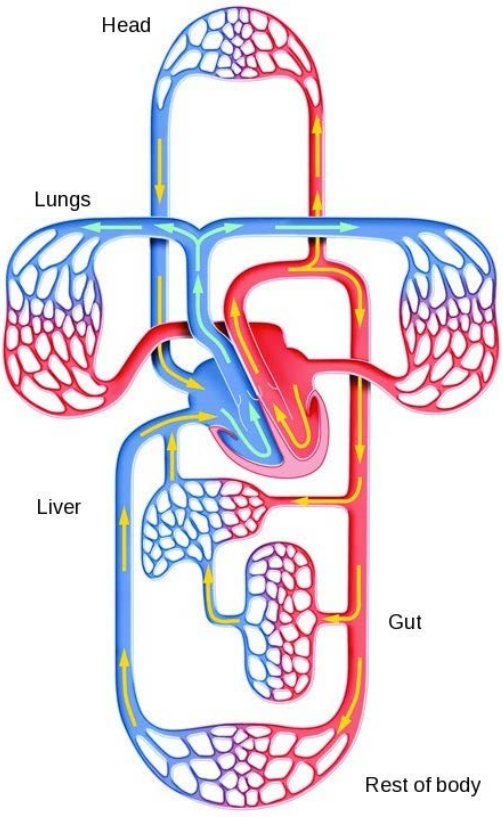

Figure 2.2: Diagram of blood circulation through out the human body. The blood flow is indicated by the yellow arrows on the diagram. The organs and veins that transport de-oxygenated blood are colored in blue; the organs and arteries that transport oxygenated blood are colored in red. De-oxygenated blood becomes oxygenated after picking up oxygen in the lungs; the oxygenated blood become de-oxygenated after the exchange of carbon dioxide and oxygen that takes place in the capillaries. (From http://www.clipart.dk.co.uk/428/subject/Biology/Double_circulation.)

The myocardium contracts after receiving the stimulation of the electrical impulse generated by the sinoatrial node of the heart. In the myocardium, the electrical impulse propagates mainly along the cardiac fibers, so does the contraction of myocardium. Thus the architecture of myocardium has an impact on the cardiac function.

2.3.3 Heart wall

The heart wall has three layers (see Fig. 2.3). The epicardium, which consists of a thin serous membrane, is the outermost layer of the heart wall, and is also the inner wall of the pericardium. The myocardium, the middle layer of the heart wall, is the thickest layer among the three layers, and is comprised of cardiac muscle which is squeezed and wrung as the heart beats. The endocardium is the inner layer of the heart wall. Its extensions merge with the inner lining of blood vessels, cover the flap of heart valves, and contract with the blood in the heart.

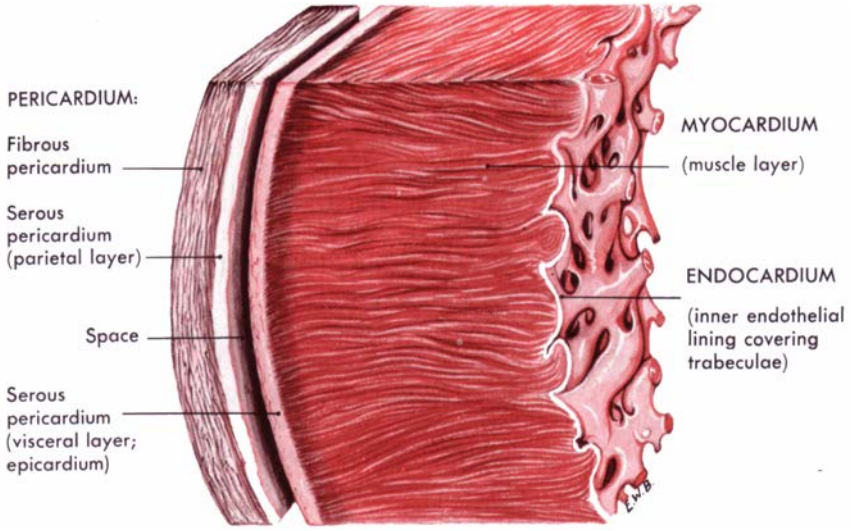

Figure 2.3: Section of heart wall showing the compoments of the outer pericaridum, muscle layer (myocardium), and inner lining (endocardium). (From http://histologyolm.stevegallik.org/node/347.)

The heart wall of the two ventricles are significantly thicker than the heart wall of the two atriums. And the heart wall of left ventricle is thicker than the heart wall of right ventricle. The thickness of heart wall of the chambers indicates the force needed during contraction. While the force is originated from the myocardium, which is composed of spontaneously contracting cardiac muscle fibers.

The cardiomyocyte is known as the basic constitute unit of myocardium It can be imaged by transmission electron micrography (see Fig. 2.5 for an example) and by phase-contrast monochromatic X-ray [Varray *et al.* (2013)] (see Fig. 2.6). A cardiomyocyte has a length that ranges from 50 to 150 μm and a diameter ranging from 10 to 20 μm. Cardiomyocytes

are firmly jointed end-to-end by intercalated discs. The intercalated disk allows for rapid propagation of electrical wave of depolarization between adjacent cardiomyocytes. The cardiac muscle fibers branch. As a result of fiber breaching feature, the cardiac muscle tissue is interwoven, and one stimulation that causes the contraction of one fiber will result in the contraction of a whole group of fibers. The branching cellular networks of cardiomyocytes with intercalated discs in between allow cardiac muscle cells to contract coordinately.

2.3.4 Cardiac architecture models

As stated in the above, the cardiac muscle in the myocardium contracts after receiving the stimulation of electrical impulses, and the heart beats. At the microscopic scale, the free propagation of electrical impulses between cardiomyocytes in every direction via intercalated disks makes sure that the myocardium functions as a single contractile unit. While at a larger scale, the spatial arrangement of cardiomyocytes influences the electrical and mechanical function of the heart [Spach *et al.* (1988)].

To understand how the structure of the heart influences its electrical and mechanical function, it is necessary to obtain detailed information about the cardiac architecture of myocardium, i.e., the three dimensional arrangement of cardiomyocytes and the associated connective tissue hierarchy throughout the heart wall.

Fig. 2.4 shows several mayor cardiac models in understanding the cardiac architecture. In the following, we will detail four cardiac architecture models among them.

Sheet model

LeGrice and co-workers studied the three-dimensional arrangement of ventricular muscle cells and the associated extracellular connective tissue matrix in dog hearts using scanning electron micrograph. They observed that cardiac muscle fibers were organized into an ordered laminar tissue sheets separated by extracellular connective tissues (see Fig. 2.7) and the distribution of the number of cardiomyocytes through the thickness of a muscle layer were highly consistent. Across a typical muscle layer, there are usually four cardiomyocytes that are uniformly connected to each other. The number of cardiomyocytes through a muscle layer varies from 1 to 12. While a branch that connects adjacent layers is generally one to two cardiomyocytes thick. Between adjacent layers, there are appreciable spaces. Thus the arrangement of cardiomyocytes in a muscle layer is compact, but is sparse between muscle layers. They state that ventricular myocardium is not a uniformly branching continuum but a laminar hierarchy. They present a sheet model to demonstrate the layered cardiac micro structure (see Fig. 2.8).

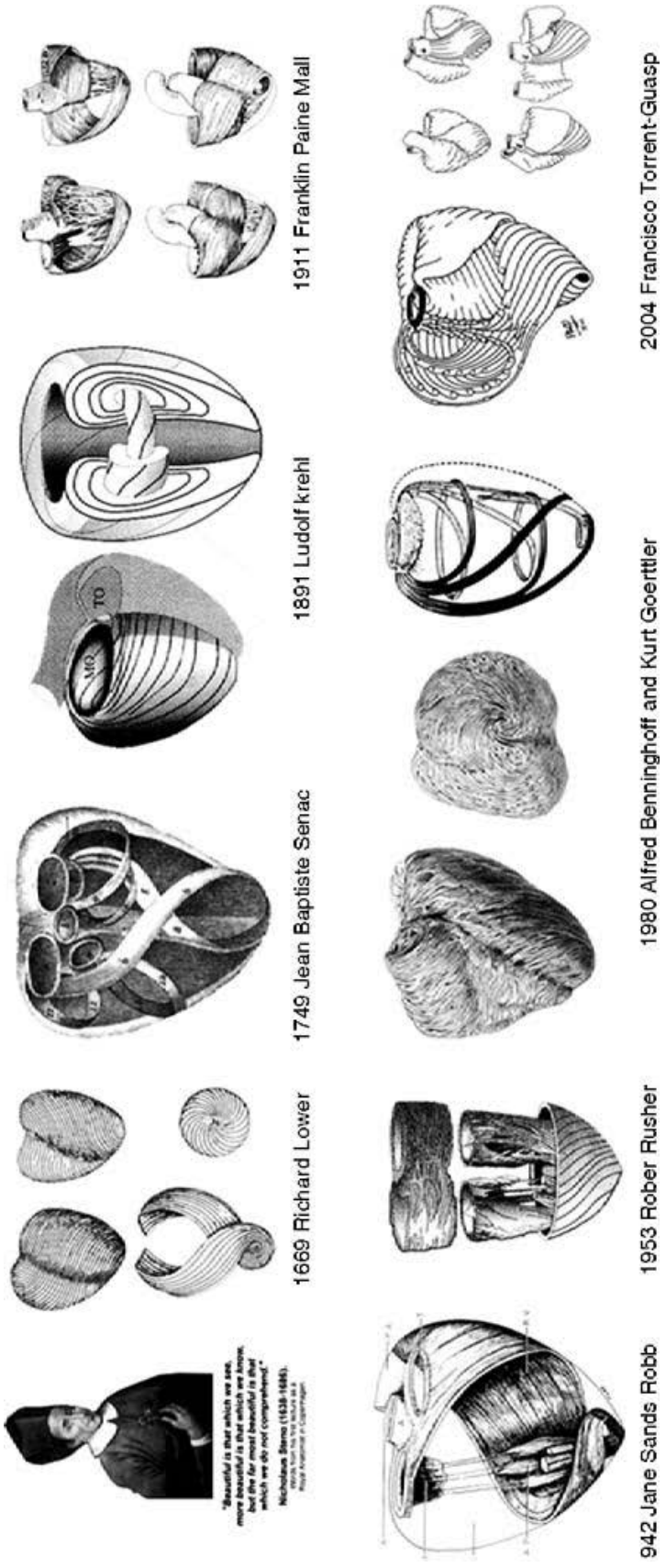

Figure 2.4: Illustration of mayor cardiac model contributions in understanding the ventricular myocardial architecture. (From [Kocica *et al.* (2006)].)

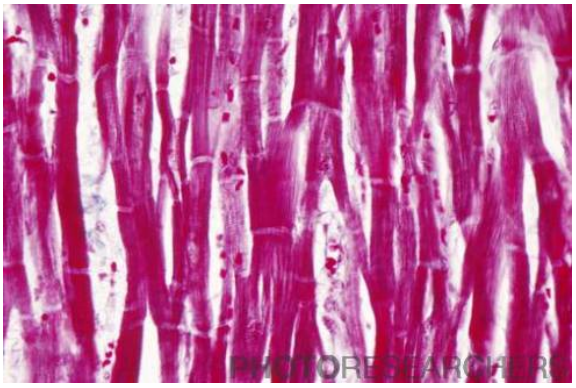

Figure 2.5: Transmission electron micrography (TEM) of a dissection of healthy human myocardium, seen in longitudinal section. Bundles of muscle fibers are stained, running vertically. Cardiomyocytes are joined end to end by intercalated discs, forming a continuous network which allows for efficient transmission and regulation of muscle contraction. (From http://www.images.sciencesource.com/.)

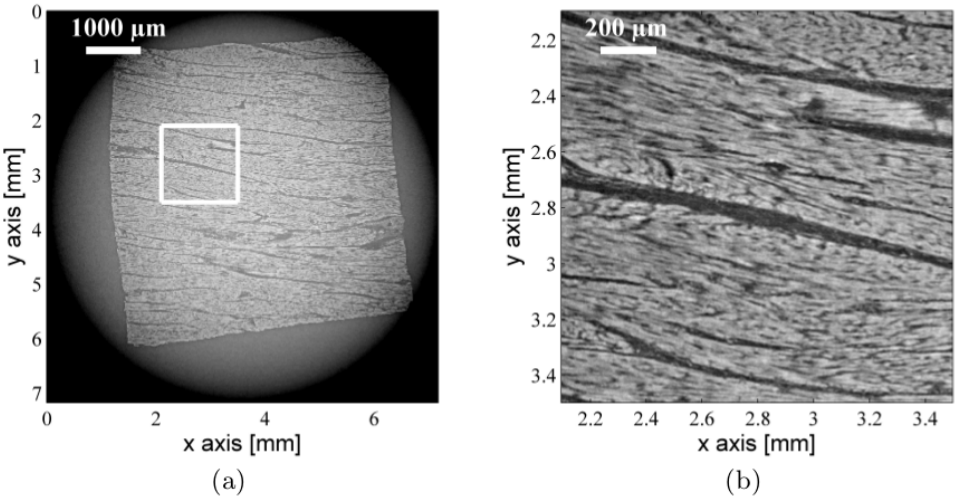

Figure 2.6: Phase-contrast monochromatic X-ray images of human heart tissue. (a) Example of a reconstructed slice of the human post left ventricular wall. (b) A zommed view of the region in the white box in (a). (From [Varray *et al.* (2013)].)

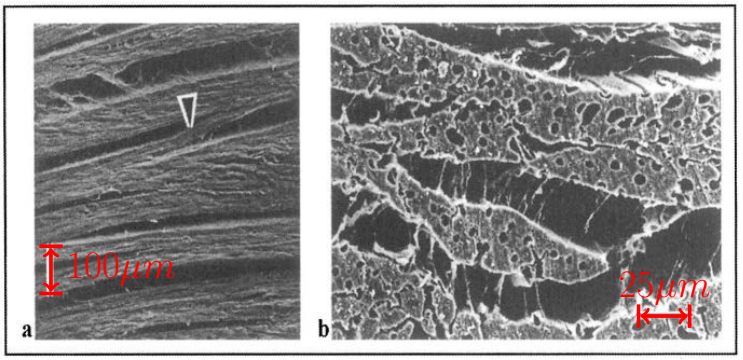

Figure 2.7: Scanning electron micrography of ventricular myocardium of the dog. (a) Tangential view of myocardium (parallel to epicardium surface) shows layered organization of cardiomyocytes. Arrow shows muscle bridge between sheets, and indicates branching of layers. (b) Transverse surface view of myocardium shows apillaries and permysial collagen connective tissue between adjacent sheets. (From [LeGrice *et al.* (1995), LeGrice *et al.* (2005)].)

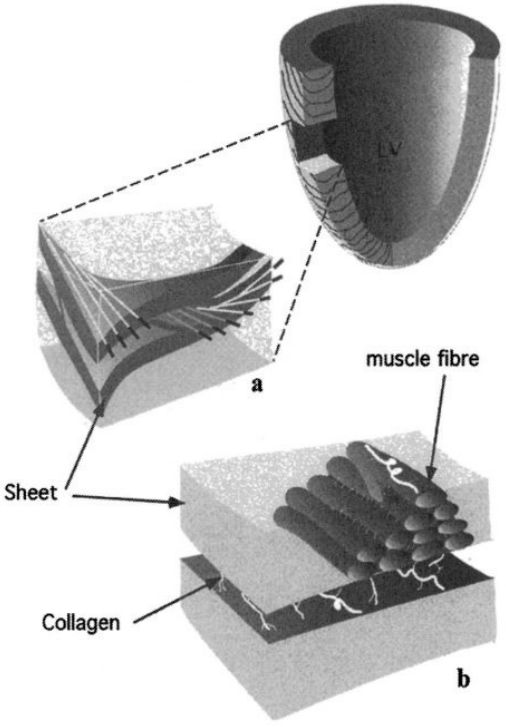

Figure 2.8: Schematic of cardiac micro structure. (a) The sheet structure of myocardium, with fiber angle varies from epicardium to endocardium. (b) Muscle fibers of three to four cardiomyocytes thick forming the cardiac layer, with extracellular collagen on the two sides for connecting adjacent layers. (From [LeGrice *et al.* (2005)].)

Helical ventricular myocardial band (HVMB) model

At macroscopic scale, Torrent-Guasp proposted the myocardial band concept of cardiac anatomy and function [Torrent-Guasp *et al.* (2005)] [Kocica *et al.* (2006)]. He observed that the ventricular myocardium could be seen as a continuous muscular band. The myocardial band is oriented spatially as a helix formed by basal and apical loops. Such a continuous muscle band exists in the ventricular myocardium of both right ventricle and left ventricle.

Fig. 2.9 shows the schematic representation of the ventricular myocardial band. The spatial configuration is shown as a helicoid. In [Francisco Torrent-Guasp and Mladen J. Kocica (2006)], Torrent-Guasp and J. Kocica detail the dissection method to obtain the myocardial band. Fig. 2.10 shows the consecutive stages for unwinding the ventricular myocardial band.

Though the theory of a helical ventricular myocardial band is still controversial [Anderson *et al.* (2009)], it has gained some favor in the medical community, and has influenced the surgical procedures in congestive heart failure [Gilbert *et al.* (2007)].

Anderson's cardiomyocyte mesh model

Rather than viewing the myocardium globally as a continuous band or focusing on the sheet-alike arrangement of cardiomyocytes in the sections of the myocardium, Anderson et al. [Anderson *et al.* (2009)] state that the cardiomyocytes are aggregated together as a three-dimensional meshwork within a supporting fibrous tissue matrix, instead of forming a continuous band, or being arranged as sheets. In the meshwork, there are two populations on observing the alignment of cardiomyocytes. The first population is aligned with their long axis of the aggregated cardiomyocytes tangential to the epicardial and endocardial surfaces. The second population is aligned with angles of intrusion across the ventricular wall. Fig. 2.11 shows the different orientations of cardiomyocytes aggregated in subepicardial, middle, and subendocardial layers of myocardium.

Geodesic model

In [Jouk *et al.* (2000)] Jouk et al. extend Streeter's geodesic model of the left ventricle [Streeter (1979)], and present a geodesic model of the cardiac fiber architecture of the entirety of the ventricular mass. They show that the fiber architecture of the heart can be conceptualized as myocardial fibers running like geodesics on a nested set of warped "pretzels" . Fig. 2.12 shows the schematic representation of the geodesic model.

Figure 2.9: Schematic representation of the spatial configuration of the ventricular myocardial band as a helicoid that consist of a basal loop and apical loop. (From [Torrent-Guasp *et al.* (2001)].)

Figure 2.10: The consecutive stages for unwinding the ventricular myocardial band (bovine heart). (From http://www.torrent-guasp.com/PAGES/VMBForm.htm.)

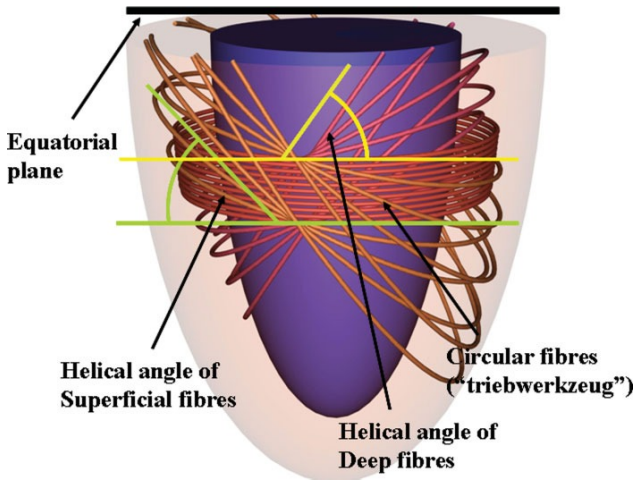

Figure 2.11: Illustration of the variation in angulation of the long axis of the aggregated cardiomyocytes within the varying depths of the ventricular wall. (From [Anderson *et al.* (2009)].)

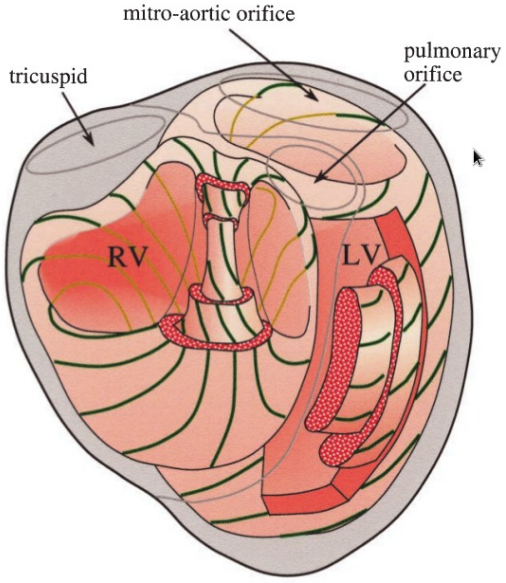

Figure 2.12: The geodesic model of the fiber architecture of the whole ventricular mass. The green lines denote the geodesic trajectories of the fibres on the nested "pretzels". (From [Jouk *et al.* (2000)].)

2.4 Cardiac imaging

By using imaging techniques we can visualize and quantitatively analysis anatomical structures and morphological abnormalities of the heart. Due to the inherent nature of cardiac function, temporal visualization of the cardiac anatomy allows a better assessment of cardiac motion and mechanical function, which can not be achieved by dissection. Beyond the cardiac anatomy and movement, the metabolic function of the heart can also be observed by the imaging technical. We briefly present here the most common imaging techniques that allow to observe the cardiac structure, anatomy and function metabolic by different physical principles.

2.4.1 Computed tomography (CT)

Computed tomography produce tomographic images or "slices" of the body by utilizing computer-processed X-rays. A three-dimensional image volumes of the body can be obtained by performing digital geometry processing on a large series of two-dimensional X-ray images that are taken around a single axis of rotation. Image intensity of a CT image reflect the amount of the attenuation of X-Rays after passing through the body, and the image contrast can be enhanced by using contrast mediums.

At present, multi detector CT has improved both temporal and spatial resolutions, and allows to make cardiac studies in just a few seconds. Spatial resolution by contemporary CT machines already outperforms the spatial resolution by magnetic resonance imaging. Cardiovascular computed tomography serves as an alternative for patients that have contraindications to cardiovascular MRI.

Although computed tomography provides the noninvasive assessment with high spatial resolution, repetitive use in daily practice are not encouraged especially in younger people or women of childbearing age, as it increases the risk of lung cancer and breast cancer.

Concerning the predominant disadvantages of contrast media application and the stochastic effect of the inevitable radiation exposure, performing CT only for analysis of LV mass is not suggested [Celebi *et al.* (2010)].

2.4.2 Positron emission tomography (PET)

PET is a non-invasive nuclear medical imaging technique. It is performed by detecting pairs of gamma rays emitted indirectly by a tracer. A tracer is a short-lived positron-emitting radionuclide, and is usually chemically incorporated into a biologically active molecule. After the injection of the tracer into the patent body (usually the blood circulation system), a waiting period is needed. When fluorodeoxyglucose (FDG), an analogue of glucose, is used as the molecule tracer, this waiting period is typically an hour. Scan can

be conducted after the active molecule becomes concentrated in tissues of interest. PET produces three-dimensional images of tracer concentration within the body, which can indicate the functional processes in the body. Using PDG as the molecule tracer in PET, namely PDG-PET, is the most common type of PET scan in standard medical care. The concentrations image provided by PDG-PET indicates tissue metabolic activity by virtue of the regional glucose uptake, and thus it can explore the spreading of cancer.

In cardiology, PET can be used to detect a various of heart diseases, such as hibernating myocardium and atherosclerosis, by providing the myocardial tissue metabolic activity.

PET scanning is non-invasive, but it involve radiation exposure of a total dose around 5–7 mSv. It is more expensive than CT and MRI.

2.4.3 Single photon emission computed tomography (SPECT)

SPECT imaging is a nuclear tomographic imaging technique. It is performed by directly detecting the gamma radiation of the injected tracer using a gamma camera. Multiple two dimensional images are acquired from multiple angles by a gamma camera. A three dimensional data set can be reconstructed from the two dimensional images to provide a true three dimensional distribution of a radionuclide. A tracer need to be delivered into the patient before performing SPECT. The tracer can be either thallium-201 or technetium-99 m and is usually injected into the bloodstream of the patient.

Because SPECT permits accurate localization in 3D space, it is performed when a true 3D representation is necessary, such as in functional cardiac imaging and brain imaging. It is also favored when there is suspected or known coronary artery disease in patients.

SPECT has several limitations. It is relatively very expensive, and it is not practical when serial evaluation is essential. It involves radiation exposure. With limited image resolution, the partial volume effect would make the measurement of small heart inaccurate.

2.4.4 Echocardiography

Echocardiography, also named as cardiac ultrasound or cardiac echo, is about the ultrasound imaging of the heart. In echocardiography, standard two-dimensional, three-dimensional, and Doppler ultrasound are usually used to create images.

Echocardiography can create ultrasound images of heart structures. By using Doppler ultrasound, it can provide additional information on the cardiac wall motion and the blood flow in the heart, and thus it can provide assessment for the analysis of regional contraction and heart pumping capacity.

Echocardiography is portable and relatively inexpensive when compared with other imaging modalities. It can produce image non-invasively in real-time. These advantages make it one of the most widely used diagnostic tests in cardiology.

2.4.5 Polarized light microscopy

In [Jouk *et al.* (1995)] Jouk et al. present the polarized light microscopy approach to characterize the orientation of cardiomyocytes. This method is assessed by 3D imaging of the nuclear of the cardiomyocytes in fluorescence using confocal scanning laser microscopy. By using the uniaxial polarizing properties of myocardium, this approach provides quantitative three dimensional cardiomyocyte orientation information in the form of maps of the azimuth and elevation angles. Later in [Jouk *et al.* (2000)], this imaging technique was used to study the three dimensional cartography of the myocardium of the fetal human heart.

2.4.6 Magnetic resonance imaging (MRI)

MRI measures the relaxation of spins of nuclei of atoms after magnetic excitation. Usually the hydrogen-1 is chosen as the imaging atom because the body tissue contains lots of water. MRI is especially useful in imaging tissues with many hydrogen nuclei and little density contrast, such as brain, muscles, hearts, and tumors. MRI images have a better contrast, and are of more details when imaging soft tissues of the body than the images produced by CT or X-rays.

MRI produces images by using the property of nuclear magnetic resonance (NMR), and does not involve in ionizing radiation. MRI is noninvasive, and reproducible. The image produced is of high temporal resolution and excellent soft tissue contrast without the need for contrast medium injection. Thus the measurement by MRI is well suited to the needs of clinical examinations of the heart.

The versatility of MRI modalities provides a various of measurements. Notably diffusion MRI can provide information for the characterization of tissue. And it can be used to detect myocardial fibrosis.

In the research work presented in this thesis, we characterize the cardiac fiber architecture by the assessment of diffusion tensor magnetic resolution imaging (DT-MRI or DTI), one largely available diffusion MRI modality in clinical. We will particularly focus more on DT-MRI in the following.

2.5 Diffusion magnetic resonance imaging (Diffusion MRI)

Diffusion MRI is about the non-invasive mapping of the random movement of water molecules inside the biological tissue, in vivo or ex vivo. During the random movement of water molecules in the body, they may encounter different obstacles, such as cell membranes, proteins, macromolecules, fibers. Thus this water molecule movement varies depending on the tissue and on pathological changes, e.g., intracellular edema, abscesses, tumors. The measurement of this restricted diffusion of water molecules can provides useful structural information about tissues, such as neural tract, and heart muscle. By observing the water diffusion we can describe tissue structure indirectly.

DT-MRI is the most commonly available diffusion MRI modality. DT-MRI dates back to the early 1980s, and has largely contributed to the establishment a functional brain mapping before being applied to the study of the heart in 1995. Over the past 15 years, TD-MRI has become a common modality in diffusion MRI used in clinical and research.

In this section, we first introduce the important concepts on diffusion MRI, and then go into the details of DT-MRI.

2.5.1 Principles of diffusion magnetic resonance imaging

Here we give a brief overview fundamental principles of diffusion magnetic resonance imaging.

Basic physics NMR

Atoms consist of a nucleus and a electrons shell. In the nucleus, there are positive electrical charged protons (hydrogen nuclei, ^{1}H), which possess a spin. A proton with a moving electrical charge makes itself an electrical current, and induces a magnetic field as a result.

When protons are put in an external magnetic field, they process around the magnetic field lines, and they align either parallel (pointing up) or anti-parallel (pointing down) depending on the difference in energy levels (see Fig. 2.13). The speed of the precession, i.e., the precession frequency, is proportional to the strength of the magnetic field in which protons are placed. This relationship is described by the Larmor equation:

$$\omega_0 = \gamma \mathbf{B}_0 \tag{2.1}$$

where ω_0 is precession frequency in Hz or MHz, $\mathbf{B}_0$ is the strength of the external magnetic field in Tesla (T), and γ is the gyro-magnetic ratio that depends on the material (e.g., the value for protons is 42.5 MHz/T).

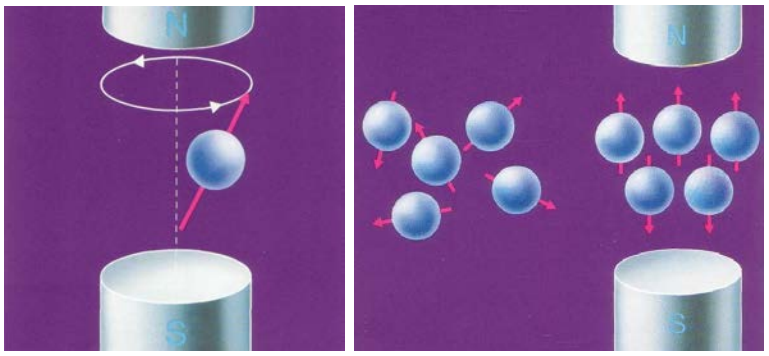

(a) (b)

Figure 2.13: (a) A proton processes around the magnetic field line when it is put in an strong external magnetic field. (b) Protons normally align randomly, but they align either parallel or anti-parallel to the magnetic field line when they are put in a strong external magnetic field. (From [Chavhan (2007)].)

The magnetic fields of anti-parallel and parallel protons cancel each others. As there are more parallel protons on the lower energy level, the summation of the magnetic field of these protons is a magnetic field longitudinal to the external field (with zero transversal magnetization, $M_{xy} = 0$.).

The magnetic field induced by protons can be measured indirectly by first sending a short radio wave, namely a radio frequency (RF) pulse, to the protons. The RF pulse exchanges energy with the protons if it has the same frequency as the proton precession, and lifts some protons to higher energy level to be anti-parallel to the magnetic field, and then results in a decrease of the longitudinal magnetization M_z. The RF pulse also cause all protons precess in phase, and establishes a new transversal magnetization M_{xy} that moves in phase with the precessing protons. This moving transversal magnetization M_{xy} will induces an electrical current in an antenna with the same precession frequency.

As soon as the RF pulse is switched off, the whole system relaxes, and goes back to its original state. This involves two independent relaxation processes. (1) Protons start to hand over the energy to their surroundings, the so-called lattice, and to go back to lower state of energy. Then the longitudinal magnetization M_z increases, and finally goes back to its original value. This process is called longitudinal relaxation, or spin-lattice-relaxation. The so-called T1-curve describes the longitudinal relaxation (see Fig. 2.14). The "longitudinal relaxation time", T1, is the time constant. (2) Protons process out of phase as a result of the inhomogeneity of the external magnet field and the inhomogeneity of the local magnet field within the tissues. And the transversal magnetization M_{xy} decreases with time. This process is called transversal relaxation, or spin-spin-relaxation, described by T2-curve (Fig. 2.15).

The changing magnetic moment can induce an electrical current in the antenna, which was the signal that we receive and use in forming MR images. This type of signal is called

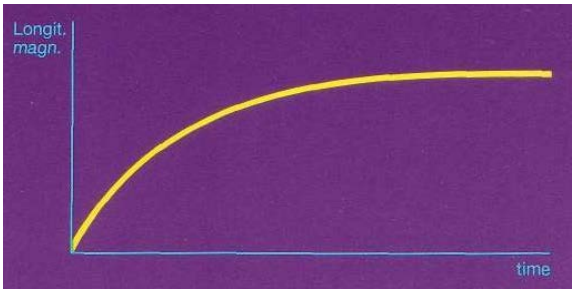

Figure 2.14: T1-curve, longitudinal magnetization M_z vs. time. (From [Chavhan (2007)].)

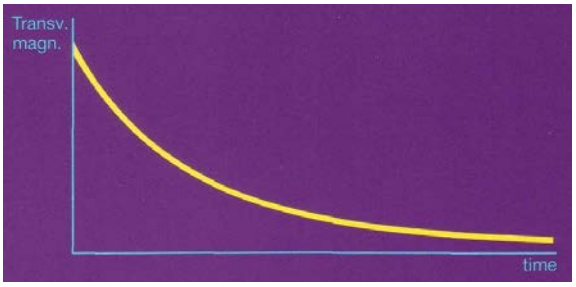

Figure 2.15: T2-curve, transversal magnetization M_{xy} vs. time. (From [Chavhan (2007)].)

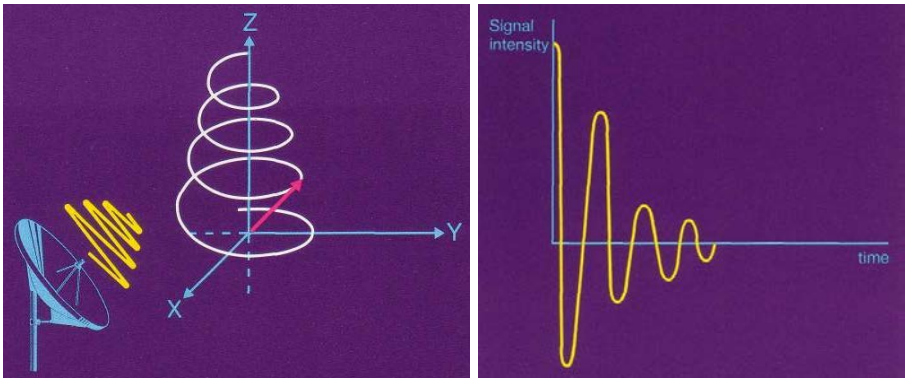

(a) (b)

Figure 2.16: (a) Illustration of the relaxation of the sum of the longitudinal and transversal magnetization. (b) The sum the longitudinal and transversal magnetization changes with time, and induces an electrical current in the antenna, the MR signal. The signal is of greatest magnitude immediately after the RF pulse is switched off and then decreases. (From [Chavhan (2007)].)

a free induction decay (FID) signal (see Fig. 2.16).

Space encoding

In practice, we impose additional magnetic fields, i.e., slice selecting gradient, frequency encoding gradient, and phase encoding gradient, to locate the position of the MR signal. When a patient are put in a magnetic field that has a different strength at each point, in the patient's cross section, protons in different places precesses with different frequencies. Thus MR signal from different locations have different frequencies. By the frequency we can assign a MR signal to a certain location, and thus we can make a picture out of this electrical current.

Spin echo sequence

We can use a RF pulse sequence to obtain the MR signal, and the pulse sequence can contains different pulses, e.g., 90° or 180° pulses. For example in Fig. 2.17, we can send 90° RF pulse two times. After sending the first 90° RF pulse, and waiting a certain time TR (i.e., time to repeat), we send another 90° RF pulse. In this experiment, the difference in signal intensity depends on the difference in the longitudinal magnetization before sending the second 90° pulses, which is related to the difference in T1 between the tissues. We produce the so-called T1 weighted image, and differentiate the tissues A and B.

Instead of sending another 90° RF pulse, we can send a 180° RF pulse after a certain time TE/2 (i.e. time of echo), which makes the protons turn around and precess in exactly the opposite direction. After another TE/2, the protons are nearly in phase again, which results in a stronger transversal magnetization, and thus in a stronger signal again, which is called an echo. We can send 180° RF pulse multi times to obtain multi echoes (see Fig. 2.18). From echo to echo the intensity of the signal goes down due to the so-called T2-effects. The image is called T2-weighted image, and this type of sequence is called a spin echo sequence, which consists of a 90° RF pulse and a 180° RF pulse (causing the echo). Note that by choosing different TR and TE, we cannot only produce T2 weighted, but also T1 weighted and proton density weighted images. Fig. 2.19 illustrates a spin echo pulse sequence.

Also we can use a different way to refocus the dephasing spins: instead of a 180° RF pulse, we apply a magnetic field gradient, with the same strength, but in opposite direction. In this case the echo is called a gradient echo.

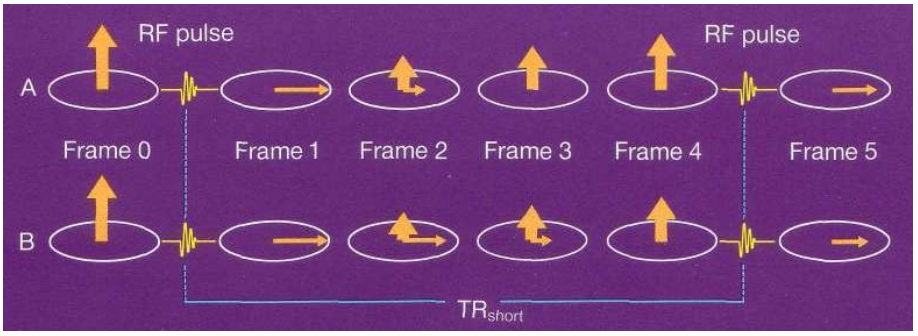

Figure 2.17: Send another RF pulse after a short TR. The signal can differentiates tissue A and tissue B by the difference of T1 between these two tissues. (From [Chavhan (2007)])

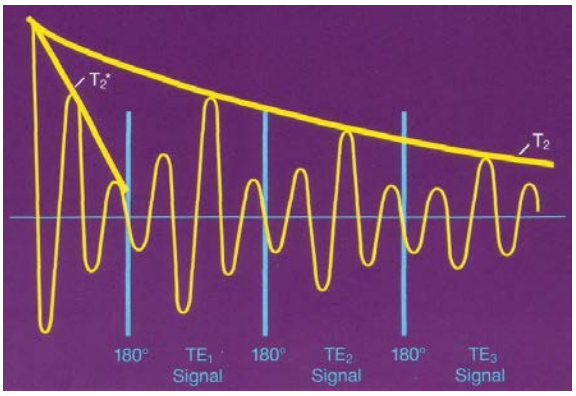

Figure 2.18: By sending multi 180° RF pulses, we can obtain multi echo. (From [Chavhan (2007)].)

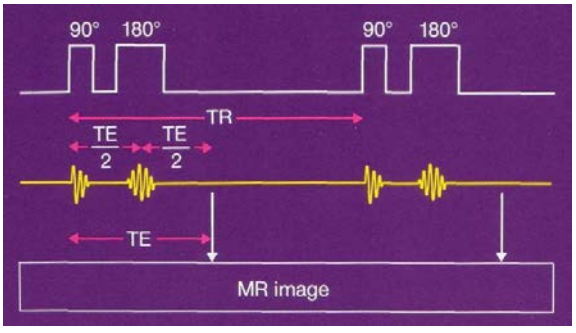

Figure 2.19: Illustration of a spin echo pulse sequence. (From [Chavhan (2007)].)

Diffusion physics

Diffusion is a microscopic phenomenon of random motion, or Brownian motion, of molecule or particle in a fluid. It results from the thermal agitation of molecules which migrate at random. It is discovered by Robert Brown [Brown (1828)]. A typical diffusion phenomenon is the process which takes place after introducing a drop of ink into a jar of water. The ink remains concentrated at first, over time it spreads radially. Finally the liquid becomes uniform, but diffusion still continues, just with no net flux. This mixing process takes place without stirring or other fluid motion.

The macroscopic process of diffusion is described by Fick's first law [Fick (1855)], which relates the net diffusive flux to the concentration field through the relationship

$$\mathbf{J} = -D\nabla\phi \tag{2.2}$$

where $\mathbf{J}$ is the net diffusion flux, D is called the "diffusion coefficient", ϕ is the particle concentration, ∇ is the gradient operator (with respect to the position $\mathbf{x}$).

The above macroscopic equation refers to the diffusion of one substance in another. When there is only one type of molecules or particles, this Brownian motion still takes place though there is no concentration gradient. The diffusion coefficient of a species in the absence of a chemical potential is defined as self-diffusion coefficient.

Using a probabilistic framework, Einstein derive an explicit relationship between the mean-squared displacement of the ensemble of particles undergoing diffusion, and the classical diffusion coefficient, D, appearing in the Fick's law (2.2), the so-called "Einstein's equation" [Einstein (1956)]:

$$D = \frac{1}{6t}\langle \mathbf{r}^T\mathbf{r}\rangle \tag{2.3}$$

where $\langle \mathbf{r}^T\mathbf{r}\rangle$ is the mean-squared displacement of the ensemble particles form their starting points over a time t, and D is the diffusion coefficient. It shows $\langle \mathbf{r}^T\mathbf{r}\rangle$ is directly proportional to the observation time t.

Diffusion pulse sequence

Almost any MRI pulse sequence can be modified to become sensitive to diffusion by applying appropriate magnetic field gradients. The basics for diffusion weighting were introduced by Stejskal and Tanner in 1965 [Stejskal and Tanner (1965)]. Fig. 2.20 shows an simple diffusion weighting pulse sequence basing on a spin echo sequence. After excitation, and before signal sampling, the application of a bipolar gradient adds to each spin's precession a positive phase proportional to its average position (along the direction of the gradient) during the first gradient lobe, and a negative phase proportional to its average position during the second lobe. The sum of these phases is related to the difference be-

tween these two positions. The bipolar gradient has no net effect on spins which do not move; they are completely "in phase" after its application. If there is spin displacement as a result of Brownian motion, the signal is attenuated exponentially by the product of the diffusion coefficient D and a factor b which is a function of the diffusion-weighting gradients, i.e.

$$f(x,y) = M_0(1 - e^{-\mathrm{TR}/T2})e^{-\mathrm{TE}/T2}e^{-bD} \tag{2.4}$$

where M_0 is the "spin density" in that pixel, $T1$ and $T2$ are the time constants of spins in the tissue at that location that vary with different tissues, and TR and TE are parameters to alter image contrast. In general, the diffusion coefficient for any direction is estimated by collecting two sets of data; one, I_1, with the diffusion-weighting gradient amplitude set to 0, such that $b = 0$, and the second, I_2, with a non-zero diffusion-weighting gradient in the desired direction of measurement. The diffusion coefficient that reflects diffusion in one direction can be estimated by [Le Bihan *et al.* (1986)] [Stejskal and Tanner (1965)]:

$$\bar{D} = \frac{\mathrm{Log}(I_1/I_2)}{b}. \tag{2.5}$$

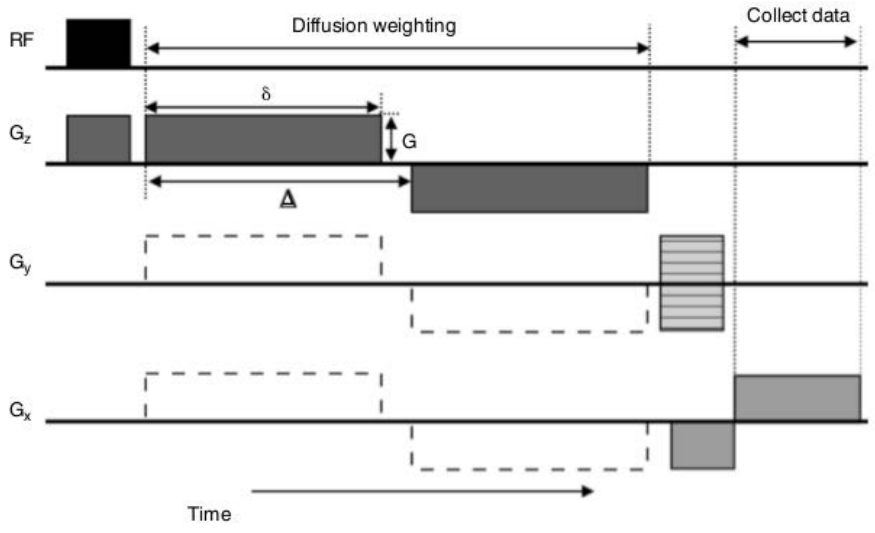

Figure 2.20: A simple diffusion weighting pulse sequence. The dotted lines on Gx and Gy denote that diffusion weighting can be applied along any gradient direction (or combination of directions). (From [Pipe (2009)].)

2.5.2 Diffusion tensor imaging (DTI)

In biological systems, water diffusion is influenced by the micro-structure and physical property of tissues. Water tends to diffuse along ordered biological structures, and the diffusion is anisotropic. The measured diffusion coefficient D will depends on the direction in which we measure it. In this case the diffusion can be model as tensor $\mathbf{D}$ [Basser

et al. (1994)]. Then the Einstein's equation in (2.3) can be generalized to the diffusion tensor [Tuch *et al.* (2003)]

$$\mathbf{D} = \frac{1}{6t}\langle \mathbf{r}^T \mathbf{r} \rangle, \tag{2.6}$$

where the diffusion tensor $\mathbf{D}$ is a 2nd-order tensor, symmetric, and positive definite, i.e.,

$$\mathbf{D} = \begin{pmatrix} D_{xx} & D_{xy} & D_{xz} \\ D_{xy} & D_{yy} & D_{yz} \\ D_{xz} & D_{yz} & D_{zz} \end{pmatrix} = \lambda_1 \mathbf{e}_1 \mathbf{e}_1^T + \lambda_2 \mathbf{e}_2 \mathbf{e}_2^T + \lambda_3 \mathbf{e}_3 \mathbf{e}_3^T.$$

The diffusion tensor $\mathbf{D}$ characterizes displacements in three dimension, can be viewed as the three-dimensional covariance matrix of displacements in a given time. It can be easily visualized as an ellipsoid (see Fig. 2.21), where the directions of axes correspond to the eigenvectors of diffusion tensor and the lengths of axes depend on the eigenvalues of the diffusion tensor $\mathbf{D}$.

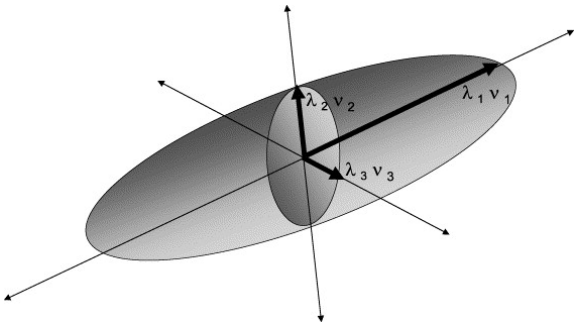

Figure 2.21: The ellipsoid representation of a diffusion tensor $\mathbf{D}$. The directions of ellipsoid axes correspond to the eigenvectors of diffusion tensor and the lengths of axes depend on the eigenvalues of the diffusion tensor (the axes are scaled according to the square root of the eigenvalues.).

In [Basser and Le Bihan (1992)], Basser and Le Bihan show that a tensor can be estimated from a series of (log-transformed) diffusion weighted signals using linear regression. We first calculat a scaling 3×3 matrix, b-matrix. It is in analogy to the scalar b-factor that is used when estimating the scalar diffusion coefficient D [Mattiello *et al.* (1997)]. Then for anisotropic media, Eq. (2.5) is rewritten as

$$\frac{I_2}{I_1} = \exp \begin{pmatrix} -b_{xx}D_{xx} & -b_{yy}D_{yy} & -b_{zz}D_{zz} \\ -2b_{xy}D_{xy} & -2b_{xz}D_{xz} & -2b_{yz}D_{yz} \end{pmatrix}. \tag{2.7}$$

As there are six unknown elements to determine in the symmetric tensor (i.e., D_{xx}, D_{yy}, D_{zz}, D_{xy}, D_{xz}, D_{yz}), we need at least six simultaneous equations. Thus, we need at least six diffusion-encoding images and one additional non-diffusion-weighted image for estimating the elements of the tensor. And these diffusion-weighted images should be acquired with gradients applied in non-collinear and non-coplanar directions [Basser *et al.*

(1994)].

By denoting $\mathbf{X}$ as a vector of the log-transformed signal intensities, $\mathbf{B}$ as a matrix with the number of rows equal to the number of measurements of the signal, and six columns (containing the unique elements of the b-matrix for each measurement).

$$\mathbf{B} = \begin{pmatrix} b_{xx}^1 & 2b_{xy}^1 & 2b_{xz}^1 & b_{yy}^1 & 2b_{yz}^1 & b_{zz}^1 \\ b_{xx}^2 & 2b_{xy}^2 & 2b_{xz}^2 & b_{yy}^2 & 2b_{yz}^2 & b_{zz}^2 \\ \vdots & \vdots & \vdots & \vdots & \vdots & \vdots \\ b_{xx}^N & 2b_{xy}^N & 2b_{xz}^N & b_{yy}^N & 2b_{yz}^N & b_{zz}^N \end{pmatrix},$$

and $\mathbf{D}_v$ as the vector containin the six elements of the symmetric diffusion tensor $\mathbf{D}$, i.e.,

$$\mathbf{D}_v = \begin{pmatrix} D_{xx} & D_{xy} & D_{xz} & D_{yy} & D_{yz} & D_{zz} \end{pmatrix}^T,$$

then the relationship between the observed signals $\mathbf{X}$ and the elements of the diffusion tensor is:

$$\mathbf{X} = \mathbf{B}\mathbf{D}. \tag{2.8}$$

We can solve Eq. (2.8) via an ordinary least ordinary least squares (OLS) approach or a weighted linear least squares (WLS) approach [Basser *et al.* (1994)] [Arsigny *et al.* (2005)] [Kingsley (2006)b], i.e.,

$$\mathbf{D} = (\mathbf{B}^T\mathbf{B})^{-1}\mathbf{B}^T\mathbf{X}, \tag{2.9}$$

$$\mathbf{D} = (\mathbf{B}^T\Sigma^{-1}\mathbf{B})^{-1}\mathbf{B}^T\Sigma^{-1}\mathbf{X}. \tag{2.10}$$

Parameters derived from the diffusion tensor

There are several parameters derived from the diffusion tensor for characterizing the diffusion [Westin *et al.* (2002)] [Kingsley (2006)a]. The trace is the sum of the three diagonal elements of the diffusion tensor,

$$\mathrm{Tr}(D) = D_{xx} + D_{xy} + D_{xz} = \lambda_1 + \lambda_2 + \lambda_3.$$

The $\mathrm{Tr}(\mathbf{D})/3$ can be thought of as being equal to the orientationally averaged mean diffusivity, MD for short,

$$\mathrm{MD} = \frac{\mathrm{Tr}(\mathbf{D})}{3}.$$

Fractional anisotropy (FA) measures the fraction of the tensor that can be assigned to anisotropic diffusion,

$$\begin{aligned} \mathrm{FA} &= \sqrt{\frac{(\lambda_1-\lambda_2)^2+(\lambda_2-\lambda_3)^2+(\lambda_3-\lambda_1)^2}{2(\lambda_1^2+\lambda_2^2+\lambda_3^2)}} \\ &= \frac{\sqrt{3}}{\sqrt{2}}\frac{|\mathbf{D}-\frac{1}{3}\,\mathrm{trace}(\mathbf{D})\mathbf{I}|}{|\mathbf{D}|}. \end{aligned}$$

To indicate the form of the diffusion tensor, Westin et al. propose three tensor shape related indices [Westin *et al.* (2002)]. They are used to described the ellipsoid's "linearity" (C_L), "planarity" (C_P), "sphericity" (C_S), and are defined as

$$\begin{aligned} C_L &= \frac{\lambda_1-\lambda_2}{\lambda_1+\lambda_2+\lambda_3}, \\ C_P &= \frac{2(\lambda_2-\lambda_3)}{\lambda_1+\lambda_2+\lambda_3}, \\ C_S &= \frac{3\lambda_3}{\lambda_1+\lambda_2+\lambda_3}. \end{aligned}$$

Chapter 3

The state of the art of tractography and cardiac fiber architecture description

3.1 Résumé

Pour parvenir à une compréhension globale de la structure et la fonction cardiaque, des études expérimentales sont effectuées sur le coeur (sains et malade) de l'animal et de l'homme du niveau moléculaire au niveau de l'organ.

Les premières études sont faites principalement au moyen de la dissection histologique. Avec le développement des techniques d'imagerie, à l'heure actuelle, il existe des techniques destructrices qui peuvent fournir une description de l'architecture de la fibre cardiaque. Par exemple, la microscopie en lumière polarisée permet d'observer les orientations des fibres, et la micrographie par transmission électronique permet d'observer les cardiomyocytes. Mais il n'y a aucune technique d'investigation non invasive qui permet la description de l'architecture de fibres in vivo avant l'émergence de DT-MRI. Cette dernière permet la mesure du mouvement anisotrope des molécules d'eau dans le tissu fibreux. Les algorithmes de tractographie sont conçus pour reconstruire les fibres cardiaques.

Dans ce chapitre, nous présentons des algorithmes de tractographie existants dans DT-MRI et les techniques pour décrire l'architecture.

3.2 Abstract

To achieve a comprehensive understanding of the cardiac structure and function, experimental investigations are performed on animal and human hearts (health and disease), from the molecular to the organ levels.

The first investigations were conducted by histological dissection. With the development of imaging techniques, there are some destructive techniques that can provide a description of the cardiac fiber architecture: the polarized light microscopy allows the mapping of fiber orientations, and transmission electron micrography allows to observe cardiomyocytes. However no noninvasive investigation technique could allow the description of fiber architecture in vivo before the emerging of DT-MRI. DT-MRI provides the measurement of the anisotropic movement of water molecules in fibrous tissue. tractography algorithms are designed to reconstruct fiber tracts.

In this chapter, we present existing tractography algorithms and cardiac fiber architecture description techniques in DT-MRI.

3.3 Tractography

In diffusion MRI, tractography is a method for identifying fibrous pathways in the body, such as white matter bundles and muscles in the living human. Tractography is the only available non-invasive tool for identifying and measuring these pathways in vivo.

As introduced in Chapter 2, myocardial fibers play an important role in the functioning of the heart. Cardiac fibers form the substrate for the propagation of electrical impulse and contraction force in the heart [Chung *et al.* (2007)]. Cardiac fiber architecture is therefore central to understand both healthy and disease hearts. In this chapter we present the state of the art of tractography methods and cardiac fiber architecture description in DT-MRI.

Before going into details of the principles of tractography, we first clarify the terminology. In the tractography literature, when referring to a single "pathway" from tractography results, people often use the terms "tract", "path", "fiber", or "trajectory". Though these names are motivated by anatomy, they do not represent real anatomic fibers. Indeed, the usual DT-MRI voxel resolution is typically $2 \times 2 \times 2\,\mathrm{mm}^3$ and is much larger than the diameter of a single fiber tissue. Thus the tractography results have no direct correspondence to smaller features like individual fiber tissues.

In this thesis, when referring to a pathway output from tractography, we will use the terms "tract", "fiber tract", and "pathways", and we will also use the more common term "fiber" when there is no ambiguity. When referring to biological fiber tissue, we use the terms

"fiber tissue" or "myofiber". Now we move on to the description of general tractography processes.

3.3.1 Tractography principles

Diffusion tractography techniques rely on a fundamental diffusion property assumption: when fiber tissues align themselves along a common axis, the diffusion of water molecules will be hindered to a greater extent across this axis than along it. Hence, when we measure diffusion along many different orientations, we expect to see diffusion in preferred orientations that correspond to axial fiber orientations. In attempting to reconstruct fiber tracts, tractography algorithms aim to find paths through the data field along which diffusion is least hindered [Behrens and Jbabdi (2009)].

In a tractography process, we first calculate water diffusion directions from diffusion weighted images (DWIs). Under the above assumption, the water diffusion direction indicates the local fiber orientation. These fiber orientations are then connected and shown as curves, or "fiber tracts".

Fig. 3.1 shows the basic steps of tractography. Fig. 3.1 (a) shows a DWI volume of a human heart. For DT-MRI, the data set contains at least six diffusion weighted image volumes acquired for different diffusion encoding directions, and one additional non diffusion weighted image volume. From the DWI volumes, we can estimate local fiber orientations (see Fig. 3.1 (b)). These orientations are represented by the vectors with the corresponding DWI slice in the background, and they are arranged into three dimensional curves (that is, fiber tracts) as shown in Fig. 3.1 (c).

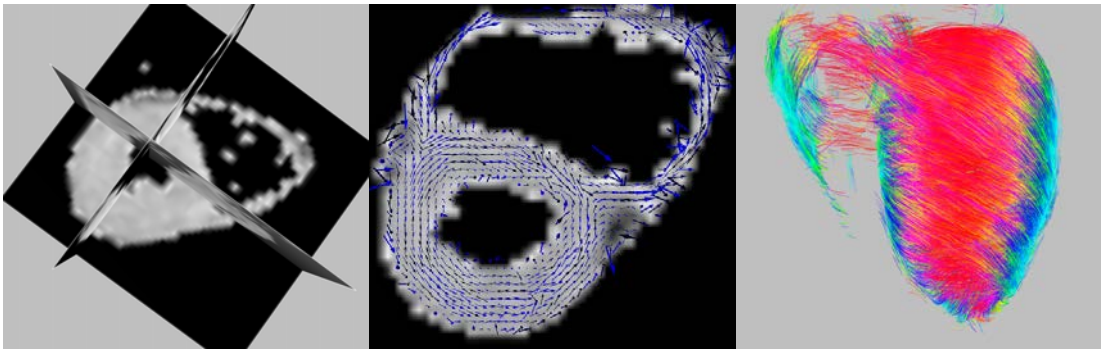

(a) (b) (c)

Figure 3.1: Basic steps of tractography. The first step is to estimate local fiber orientation from the DWIs (an example of which is shown in (a); the second step is to arrange the resulting vector field into three dimensional curves. An example of tractography result is displayed in (c).

3.3.2 DT-MRI tractography methods

Although diffusion tractography methods share the same fundamental assumption and the same objective, the adopted strategies can be quite different. Tractography algorithms can be local or global, deterministic or probabilistic, model-based or model-free; they may rely on simple or complex representations of water diffusion in body tissue.

Local tractography algorithms, such as fiber assignment by continuous tracking (FACT) [Mori *et al.* (1999)] and streamlining method [Basser *et al.* (2000)], assume that the computed water diffusions provide good estimates of the real water diffusion profiles; these estimated water diffusion directions are used directly in the curve propagation process to form fiber tracts. However real water diffusion in biological tissues is more complex than model-based water diffusion, and thus the estimated diffusion direction is susceptible to errors. In local tractography algorithms, curve propagation strategies tend to accumulate errors. Global tractography algorithms are designed to provide optimal fiber tracts under certain global energy minimization criteria, and thus to minimize the influence of measurement noise in the diffusion data. They form fibers globally to best fit the diffusion data instead of propagating a fiber tract step by step from an initial seed position.

A tractography algorithm can also be either deterministic or probabilistic. When we say that a tractography algorithm is deterministic, we mean that if we run the algorithm several times with the same initialization parameters on the same data set, we obtain the same fiber tracts. By contrast, repeated runs of the same probabilistic tractography algorithm produce different results. By repeatedly initializing a probabilistic algorithm at the same seed position, we can observe the variations of the fiber tracts, and hence characterize the probability of the existence of a fiber tract between two regions of interest.

Here, we focus on the tractography algorithms proposed in diffusion tensor imaging, and detail some of them.

Deterministic tractography

Early tractography algorithms, such as FACT, Streamline, and tensor line deflection (TEND), are local and deterministic. They are based on the assumption that diffusion tensors provide suitable estimates of the fiber orientation within each voxel, and they rely on curve propagation techniques to delineate fiber tracts.

Fiber assignment by continuous tracking (FACT) This method introduced by Mori et al in [Mori *et al.* (1999)] is the first successful tract reconstruction performed on a fixed rat brain [Mori *et al.* (1999)] [Mori and van Zijl (2002)].

Fig. 3.2 shows the simple curve propagation strategy of FACT. A fiber tract is constructed by first initializing a seed point, and then sequentially following the principal eigenvector

of the tensor at each voxel, (i.e., the eigenvector corresponding to the largest eigenvalue), until a termination condition is met. Note that the tract step length varies during the fiber tract propagation process.

Fig. 3.2 and Fig. 3.3 show simple curve propagation approaches.

These simple propagation approaches run very fast, but the reconstructed fiber tracts are flawed when the data resolution is low. In such cases, interpolation techniques create smoother fiber tracts and are more accurate when the curvature of a reconstructed line is steep with respect to imaging resolution. In [Conturo *et al.* (1999)], tractography is performed on interpolated DT-MRI data, using FACT [Mori *et al.* (1999)]. Interpolation can be alternatively performed on each coordinate of the principal eigenvector field or of the tensor field during propagation [Basser *et al.* (2000)].

Streamline method In [Basser (1998)] [Basser *et al.* (2000)], Basser et al. propose to represent white matter fiber tracts by a three dimensional streamline (i.e., a vector $\mathbf{r}(s)$ parameterized by the arc length s of the trajectory.

Fig. 3.4 illustrates the streamline representation of a fiber tract segment. The Frenet equation describes the evolution of $\mathbf{r}(s)$ as follows:

$$\frac{d\mathbf{r}(s)}{ds} = \mathbf{t}(s), \tag{3.1}$$

where $\mathbf{t}(s)$ is the unit tangent vector at $\mathbf{r}(s)$.

In [Basser *et al.* (2000)], the local tangent vector $\mathbf{t}(s)$ of a fiber tract is identified with the unit principal eigenvector at $\mathbf{r}(s)$, i.e.,

$$\mathbf{t}(s) = \boldsymbol{\varepsilon}_1(\mathbf{r}(s)), \tag{3.2}$$

where $\boldsymbol{\varepsilon}_1$ is the principal eigenvector of the diffusion tensor. This gives

$$\frac{d\mathbf{r}(s)}{ds} = \boldsymbol{\varepsilon}_\mathbf{1}(\mathbf{r}(s)). \tag{3.3}$$

This implicit three dimensional differential equation is solved for the fiber tract trajectory subject to an initial condition $\mathbf{r}(0) = \mathbf{r}_0$ that specifies a starting point (or seed point), on the fiber tract.

The computation can be performed using Euler's method, or higher order numerical method, such as the 4th-order Runge-Kutta method, or adaptive Runge–Kutta methods.

Tensor deflection (TEND) The TEND method proposed in [Lazar *et al.* (2003)] employs the fiber tract propagation strategy of FACT. But instead of using principal eigenvec-

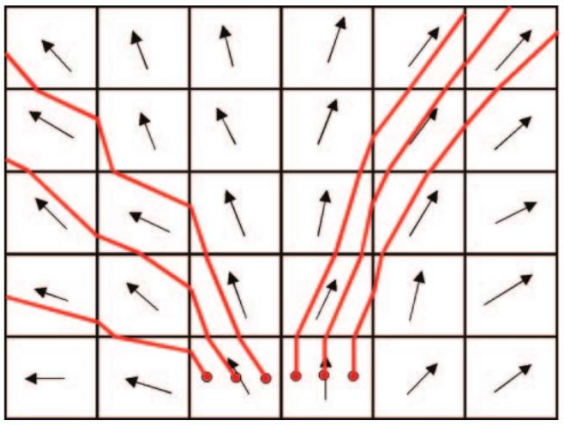

Figure 3.2: Illustration of the FACT algorithm. Arrows represent primary eigenvectors in each voxel. Red lines are FACT fiber tracts. (From [Mukherjee *et al.* (2008)]).

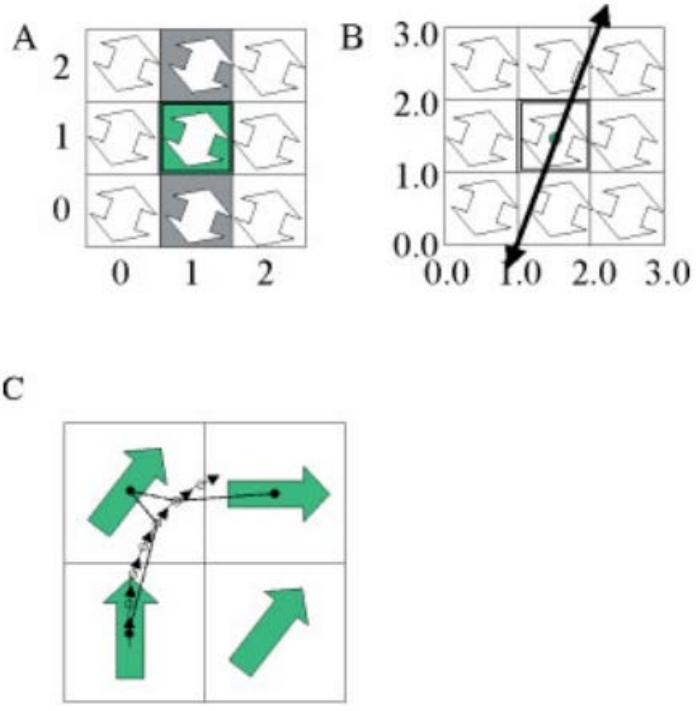

Figure 3.3: Illustrations of curve propagation approaches in deterministic tractography. (a) A curve is propagated simply by connecting pixels. (b) A curve is propagated in the continuous coordinate. (c) An interpolation curve propagation approach. (From [Mori and van Zijl (2002)].)

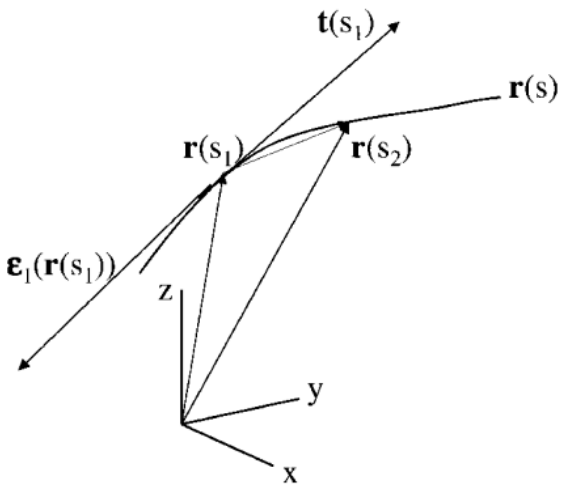

Figure 3.4: Three dimensional streamline representation of a fiber tract $\mathbf{r}(s)$. The local tangent vector $\mathbf{t}(s_1)$ is identified with the principal eigenvector $\boldsymbol{\varepsilon}_1(\mathbf{r}(s_1))$ of the diffusion tensor $\mathbf{D}$ at position $\mathbf{r}(s_1)$. (From [Basser *et al.* (2000)].)

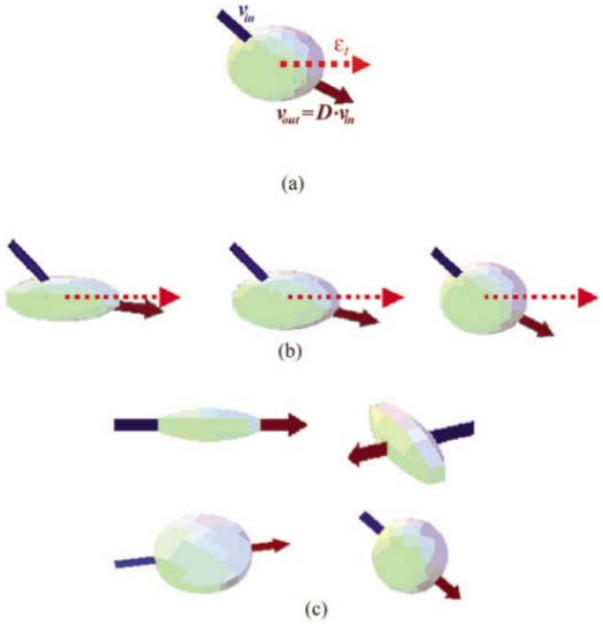

Figure 3.5: Tensor deflection for different tensor shape. (From [Lazar *et al.* (2003)].)

tors for fiber tract propagation, TEDN uses the tensorline propagation strategy [Weinstein *et al.* (1999)] to compute the step directions.

The tensorline propagation strategy uses the entire diffusion tensor to deflect the incoming vector direction to obtain the next step direction:

$$\mathbf{v}_{\text{out}} = \mathbf{D} \cdot \mathbf{v}_{\text{in}}, \tag{3.4}$$

where $\mathbf{v}_{\text{in}}$ is the incoming direction, $\mathbf{v}_{\text{out}}$ is new step direction for fiber tract propagation, and $\mathbf{D}$ is the diffusion tensor.

Fig. 3.5 illustrates how the shape of the tensor (or equivalently, the ratios between tensor eigenvalues λ_1, λ_2, and λ_3), affect $\mathbf{v}_{\text{out}}$. For example, when $\lambda_1 \gg \max(\lambda_2, \lambda_3)$, the output vector of the TEND algorithm is deflected towards the direction of the principal eigenvector (that is, $\mathbf{v}_{\text{out}} \approx \lambda_1 \alpha_1 \mathbf{e}_1$).

Seeding The three tractography methods presented above need initial seed positions to generate fiber tracts. The selection of appropriate seed points is usually performed by an operator; alternatively, all the voxels of the DWI data set are seeds. The second seed initialization strategy is called "brute-force", and is used in combination with tract-editing methods to identify tracts of interest. Regarding current DT-MRI resolution and the potential complexity of body tissue in the image, small changes in seed positions can lead to very different results. Therefore, the selection of anatomically appropriate regions is crucial. For the same reason, seed density must be set with caution when using "brute-force" seeding [Cheng *et al.* (2012)].

When to stop a fiber tract? A fiber tract should not propagate infinitely: it should stop when it reaches the anatomical region limit. While in the anatomical region, the propagation of a fiber tract should follow some criteria. A criterion use fractional anisotropy (FA): the propagation is stopped when a fiber tract goes through a voxel where the FA value is below a certain threshold. This criterion is chosen because regions with low FA tend to be associated with high uncertainty (in such regions, the principal eigenvector of the diffusion tensor is poorly estimated. Hence, using such an anisotropy criterion it is possible to avoid large errors along streamline paths.

Another common criterion for fiber tract termination is based on local curvature: when the angle change between successive propagation step directions is above a given threshold, the tract is not allowed to propagate further.

The motivation for this criterion is that a sudden direction change is likely to be caused by noise. It is also used to prevent a fiber tract from going backwards.

A criterion can also be set according to the coherence of fiber orientations within neigh-

boring voxels. In practice, it is possible to combine different criteria.

Errors Tractography processes are subject to errors. The three main causes of errors are the following [Behrens and Jbabdi (2009)]:

- Noise from imaging equipment and artifacts. In [Dietrich *et al.* (2007)], Dietrich et al. discuss the measurement of signal-to-noise ratios in MR images regarding the MRI system components.
- Diffusion modeling noise: a diffusion model may not fully characterize the water diffusion in complex body tissue.
- Integration errors in fiber tract propagation. In [Lazar and Alexander (2003)], Lazar and Alexander discussed the integration errors for different fiber tract propagation techniques.

These errors accumulate along fiber tract, produced by tractography algorithms based on line propagation techniques.

Global methods

Global tractography algorithms reduce the impact of error accumulation along fiber tracts by constructing them globally. Instead of propagating fiber tracts step by step from initial seeds, global tractography algorithms produce fiber tracts in one shot by optimizing a certain global objective. The global nature reduces sensitivity to noise and modeling errors.

Most global tractography algorithms, especially the ones proposed in the context of neurology, are designed to find connections between different anatomical regions [Mangin *et al.* (2002)] [Jbabdi *et al.* (2007)] [Iturria-Medina *et al.* (2007)] [Zalesky (2008)] [Fillard *et al.* (2009)] [Mangin *et al.* (2013)]. By contrast, in the context of cardiology, the goal is to estimate the cardiac muscle organization [Rohmer *et al.* (2007), Toussaint *et al.* (2010)]. Here, we focus on global algorithms that produce fiber tracts rather than connections between regions.

A global method combined with local methods The global reconstruction approach proposed by Reisert et al. [Reisert *et al.* (2009)] uses the ideas of both local and global methods. To combine their advantages: fast for local method, and no accumulated errors along fiber tracts for global method. This approach use local methods within a global optimization process; it provides a set of global optimum fiber tracts rather than the fiber tracts that connect specific regions.

Graph-based method Frindel et al. proposed a graph-based algorithm for assessing fiber tract organization globally in the human heart [Frindel *et al.* (2010)]. The tractography problem is formulated into a global problem of computing fiber tracts in a boolean-weighted undirected graph. The vertices of the graph are voxels of the diffusion tensor volume and the edges represent the possible connection of two neighboring voxels by a fiber bundle. Fiber tracts are formed by selecting the edges that best fit the data set under a global minimization process, and thus are produced in one shot for the whole data set rather than constructed fiber by fiber as in local algorithms (other global algorithms are proposed in [Iturria-Medina *et al.* (2007)] [Zalesky (2008)]; they need seed initialization).

In addition to rebustness to noise and modeling errors, the graph representation of fiber tracts, allows optimal balance between the density of fiber bundles and the amount of available data.

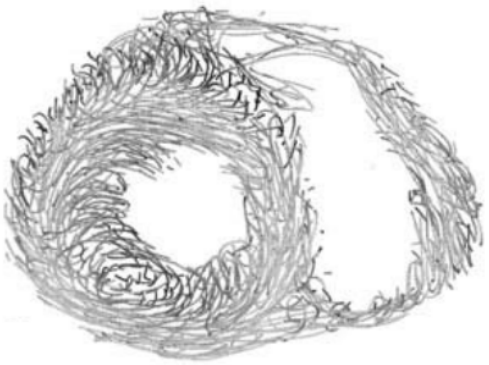

Figure 3.6: Small axis view of one slice of tractography results of a healthy human heart. (from [Frindel *et al.* (2010)])

Probabilistic tractography

Noise in DWI data introduces uncertainty in the estimated local fiber orientations, and hence errors in the tractography process. Deterministic tractography algorithms suffer from the noise because they use the tensor or the principal eigenvector directly to construct fiber tracts [Lazar and Alexander (2003)]. As stated above, seed initialization is crucial in tractography and a spatial bias induced by noise at one point in the middle of a fiber tract can also change the fiber tract greatly.

Probabilistic tractography algorithms model the uncertainty by providing results in the form of a probability distribution, rather than a single estimate of a fiber tract. They indicate the confidence interval of the estimates of fiber tracts arising from a seed point.

Many probabilistic tractography algorithms share similar deterministic techniques. (Note that they may suffer from the same limitations as deterministic algorithms, and a single

fiber tract provided by a probabilistic tractography algorithms is not more "accurate" than one obtained deterministically. Starting from a seed point, the fiber tract propagates in a similar way, but with each step direction selected at random from a local probability density function (PDF) of fiber orientations. The PDF indicates the uncertainty in the data set for fiber orientations. In other words, the direction for the next step propagation is drawn from a range of likely orientations according to some probabilities, and therefore is no longer unique.

By running a probabilistic tractography algorithm many times from one seed point, we can generate a bunch of fiber tracts to indicate the variability of fiber tracts resulting from noise and uncertainty in the data. By counting the number of fiber tracts that traverse each voxel, we can obtain a density map of fiber tracts, which can provide quantitative description of the connection between the seed and other voxels (see Fig. 3.7 for an example of such connection map.). The ability of providing an estimate of the precision of a constructed fiber tract is the main benefit of probabilistic tractography approaches in neural imaging [Tournier *et al.* (2011)]. This type of quantitative characterization is useful for the description of white matter connections between different brain regions [Behrens *et al.* (2003)] [Parker *et al.* (2003)]. However the probability values only reflect the confidence in the existence of connections between a seed and other voxels [Jones (2010)]. For cardiac imaging, it is also difficult to interpret the cardiac structure from a connection map or a too large number of fiber tracts.

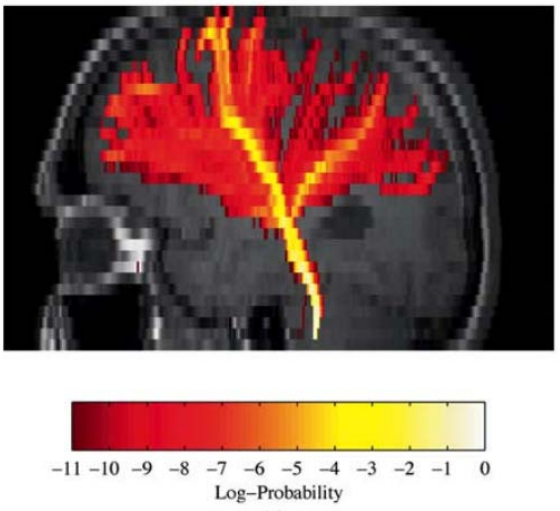

Figure 3.7: Probability connection map of brain white matter. (From [Friman *et al.* (2006)]).

Here we consider probabilistic approaches as tools for exploring potential fiber tracts rather than for quantitative connection studies, and we focus on how the local fiber orientation PDF is characterized.

A local fiber orientation PDF provides an estimate of fiber tract orientation. The accuracy

of fiber orientation PDF directly affects the quality of fiber tracts.

There exist a number of methods for the estimation of the fiber orientation PDF. In [Tournier *et al.* (2003)] and [Parker *et al.* (2003)], the fiber orientation density function is determined empirically from the local diffusion tensor. In [Cook *et al.* (2004)], the sphere Watson distribution [Mardia and Jupp (2009)] is used as the local fiber orientation PDF, and the parameters of the distribution are determined by the eigenvalues of the diffusion tensor. Behrens et al. [Behrens *et al.* (2003)] propose to estimate the fiber orientation PDF in the Bayesian framework. The estimated probability distributions are PDFs on parameters in a diffusion model given the data set. The parameters of the diffusion model are free and the probability distribution is obtained by Markov chain Monte Carlo sampling. In [Friman and Westin (2005)] and [Friman *et al.* (2006)], the authors propose to approximate the continuous PDF by a discrete one by evaluating the it at a sufficiently large number of points evenly spread over the unit sphere. Then, the local fiber orientation is sampled from the predefined directions according to the discrete PDF.

The probabilistic tractography algorithms presented above are parametric in the sense that they use a model to explain the data. There exist nonparametric approaches which do not make any assumptions regarding the noise and which implicitly take any source of variability in the results into account. Note that it is also possible to make no assumption on the underlying water diffusion profile in high angular resolution diffusion weighted magnetic resonance imaging (HARDI) [Tuch (2002)] [Tournier *et al.* (2004)].

In [Jones (2003)] [Lazar and Alexander (2005)] [Jones and Pierpaoli (2005)], bootstrap tractography algorithms are developed to estimate the uncertainty in tractography results. Without any a priori assumptions on the noise, random samples are generated for every voxel in the data set. Then fiber tracts are generated by deterministic tractography approaches on both the average and bootstrap DWI volumes. The probability of connection between two voxels is defined by the density of the fiber tracts between them.

3.4 Cardiac fiber architecture description

To achieve a comprehensive understanding of the cardiac structure and function of the heart, experimental investigations are performed on animal and human heart (health and disease), from the molecular to whole organ level. Pioneering investigations were performed by histological dissection, which only allows the macroscopic description of the heart, (see, e.g., in the study of helical ventricular myocardial band model of Torrent-Guasp [Torrent-Guasp *et al.* (2005)]). There are some destructive techniques that can provide finer description of cardiac architecture: polarized light microscopy allows the mapping of fiber orientations, and transmission electron micrography allows to observe cardiomyocytes. However no noninvasive investigation technique could describe in vivo fiber architecture before the emerging of DT-MRI.

Up to now, most cardiac DT-MRI studies were performed ex-vivo. In vivo cardiac DT-MRI remains challenging due to cardiac and respiratory motions. Recently, DT-MRI of moving organs greatly evolved, and now provides a mean to study in vivo cardiac fiber architecture. In [Dou *et al.* (2002)], a single cardiac phase encoding method is developed for imaging the beating heart. Stoeck et al. [Stoeck *et al.* (2012)] reconstructed three dimensional fiber tracts of a whole heart at peak systole and diastole using Local-look STEAM (stimulated-echo acquisition mode) with breath holding.

In the following, we present the existing techniques in DT-MRI for the quantification of cardiac fiber architecture.

3.4.1 Voxel-based cardiac fiber architecture description

Voxel-wise fiber information in cardiac DT-MRI is usually represented in the form of local fiber orientations. In addition to fiber angles, diffusion indices, such as fractional anisotropy, also reveal the properties of fiber structure. Early studies in cardiac DT-MRI validate the use of DT-MRI for the mapping of cardiac fibers. The results of later studies on diseased hearts suggest that DT-MRI is a valuable tool for determining cardiac pathological changes.

In [Garrido *et al.* (1994)] [Reese *et al.* (1995)], DT-MRI is used to characterize cardiac fiber orientations, under the hypothesis that the principal eigenvectors of diffusion tensors are parallel to local fiber orientations. This hypothesis is tested in the quantitative fiber orientation comparisons studies in [Hsu *et al.* (1998)] [Scollan *et al.* (1998)]. In [Hsu *et al.* (1998)], Hsu et al. compare DT-MRI fiber orientation mappings and histological measurements myocardia. Quantitative comparisons on point-by-point fiber angles and on transmural rotation of helix angles show an excellent correlation between the two methods.

In [Chen *et al.* (2003)], Chen et al. evaluate the microscopic structural change in the myocardia of rats after infarct surgery. In an infarcted myocardium, an increased water diffusivity (41% increase in trace values) and a decreased diffusion anisotropy (37% decrease in relative anisotropy index) are observed. The changes of diffusion anisotropy and regional angular deviation of the diffusion tensor show strong correlation with the microscopic fiber disorder determined by histological analysis.

In [Tseng *et al.* (2006)], Tseng et al. study the relationship between myofiber disorder and myocardial hypokinesis using DT-MRI. Regional disorder of fiber orientation and decrease of FA are found in hypertrophic cardiomyopathy.

In [Wu *et al.* (2009)], Wu et al. investigate the sequential changes of myocardial macro- and micro-structures from recent myocardial infarction to chronic myocardial infarction using DT-MRI. The infarct-adjacent zone shows an increase of mean diffusivity, a decrease

of fractional anisotropy and a decrease of mean helix angles comparing with the remote zone.

The helix angle, the angle that the tensor first eigenvector makes with the short axis plane (see Fig. 3.8), has been used to describe the cardiac fiber architecture. In studies of [Toussaint *et al.* (2010)] and [Lombaert *et al.* (2012)], the distribution along the transmural depth (from the epicardium to the endocardium) of the fiber helix angle and transverse angle are shown in the form of histograms. The helix angle of the average fiber orientation is found to be highly correlated to the transmural depth.

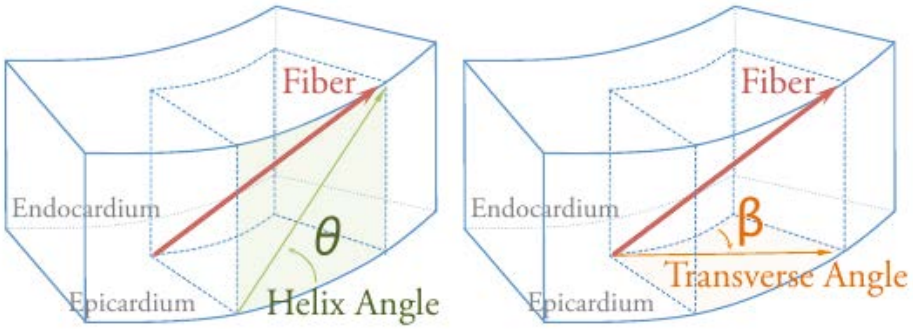

Figure 3.8: Illustration of the definitions of helix angle and transverse angle. The helix angle is the angle that local fiber orientation makes with the short axis plan on the tangent plane (displayed in green). The transverse angle is defined on the horizontal normal plane (displayed in orange). (From [Lombaert *et al.* (2012)].)

3.4.2 Tract-based cardiac fiber architecture description

By assuming the water diffuse more freely along fiber tissues, we can reconstruct fiber tracts using tractography techniques. Most cardiac tractography approaches [Zhukov and Barr (2003)] [Rohmer *et al.* (2006)b] [Rohmer *et al.* (2006)a] are direct applications of the tractography algorithms proposed for brain white-matter tracking; there are only a few approaches originally designed for the heart, e.g, the global graph approach by Frindel et al. [Frindel *et al.* (2010)] and the sheet reconstruction approach by Rohmer et al. [Rohmer *et al.* (2006)a] [Rohmer *et al.* (2007)]. Here, we present the existing cardiac tractography approaches and tract-based cardiac fiber architecture description techniques.

Cardiac tractography and its visualization

The cardiac tracking method of Zhukov et al. In [Zhukov and Barr (2003)], the authors reconstruct heart muscle fiber tracts in three dimension from DT-MRI data set for the first time using the tractography method proposed in [Zhukov and Barr (2002)]

(originally proposed for the brain white-matter tractography). Fiber tracts are visualized using the RGB - XYZ mapping schemes (Fig. 3.9 (a)).

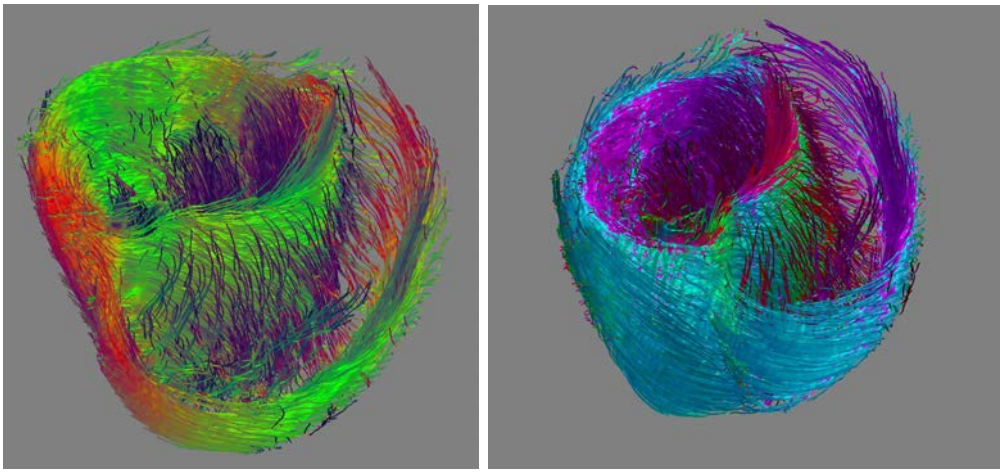

(a) (b)

Figure 3.9: Reconstruction of canine heart muscle fiber tracts using the MLS (moving least square) algorithm [Zhukov and Barr (2002)]. (a) Fiber tracts displayed using RGB-XYZ color scheme. (b) Clockwise spiral fiber tracts in the endocardium are shown in purple, and counterclockwise fiber tracts in the epicardium are shown in blue. (From [Zhukov and Barr (2003)].)

Graph-based global method of Frindel et al. Apart from direct applications of white matter tractography algorithms, a few algorithm were specifically proposed to study the cardiac architecture. As mentioned in previous section, Frindel et al. propose an automatic graph-based algorithm for assessing the global fiber tract organization of the human heart [Frindel *et al.* (2010)]. The tractography problem is formulated into a global problem of computing fiber tracts in a boolean-weighted undirected graph. Fiber tracts are formed by selecting the graph edges that best fit the data set under a global minimization process, and thus are produced in one shot for the whole data set without seed initialization.

Cardiac sheet tracking by Rohmer et al. Cardiac fibers are organized in layers (sheets) separated physically by cleavage surfaces, and water diffuses more freely inside cleavage planes than in their normal direction [Scollan *et al.* (1998)]. Histological measurements and DT-MRI assessments show that the main direction of diffusion is locally tangent to the fiber direction, the second eigenvector of the diffusion tensor is positioned inside the sheet, and the third is locally normal to the sheet [Helm *et al.* (2005)] (see Fig. 3.4.2). In [Rohmer *et al.* (2006)a] and [Rohmer *et al.* (2007)], Rohmer et al. proposed an algorithm to reconstruct the cardiac sheet structure from DT-MRI data of a human heart. The algorithm uses the two smallest eigenvectors of the tensor to recon-

struct the sheet as a surface. The structure of the reconstructed sheet compares well with histological measurements from apex to base transmural sections [LeGrice *et al.* (2001)]. Fig. 3.11 shows examples of reconstructed cardiac sheets with fiber tracts.

Cardiac fiber visualization Tractography of the heart mostly remains a highly qualitative technique due to the challenge in visualization and analysis the structure of fiber tracts.

In the cardiac tractography literature, cardiac fiber tracts obtained by tractography are usually visualized the RGB - XYZ mapping scheme [Zhukov and Barr (2003)] [Vilanova *et al.* (2006)] as shown in Fig. 3.9 (a).

In [Rohmer *et al.* (2006)b] and [Rohmer *et al.* (2006)a], the authors visualized fiber tracts by using thin tubes to increase three dimensional visual perception of the complex structure.

Inspired by techniques for the rendering of human hair, Peeters et al. [Peeters *et al.* (2006)] [Peeters *et al.* (2009)] propose to use line illumination and shadowing of fibers in order to improve the perception of the structure for dense sets of fiber tracts (see Fig. 3.12).

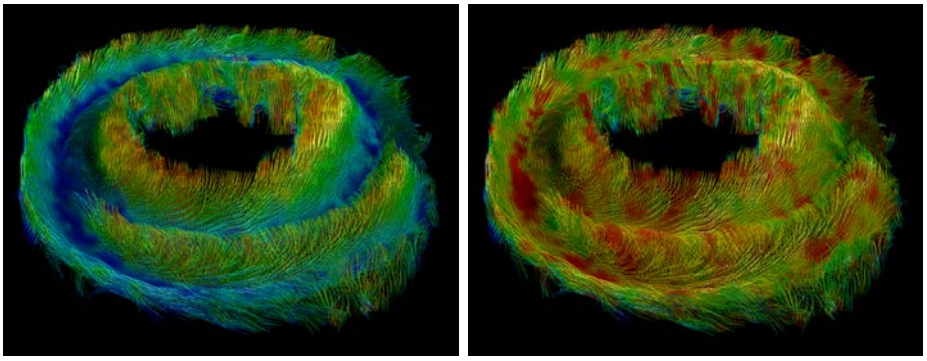

(a) (b)

Figure 3.10: Visualization of short fiber tracts with lighting and shadowing. (a) Fiber tracts are colored according to fiber orientations: blue indicates in-plane fiber tracts, red is out-of-plane. (b) Fiber tracts are colored according to FA: green indicates small values of FA and red indicates large values. (From [Peelers *et al.* (2006)].)

Fiber tract description

Statistics on fiber length and on fiber number In [Wu *et al.* (2007)], Wu et al. study the myocardial fiber pathway distribution. The distributions of the length and number of fibers are analyzed quantitatively as a function of the fiber helix angle in step of 9°. From the tractography results, they found that the majority of the fiber tracts are

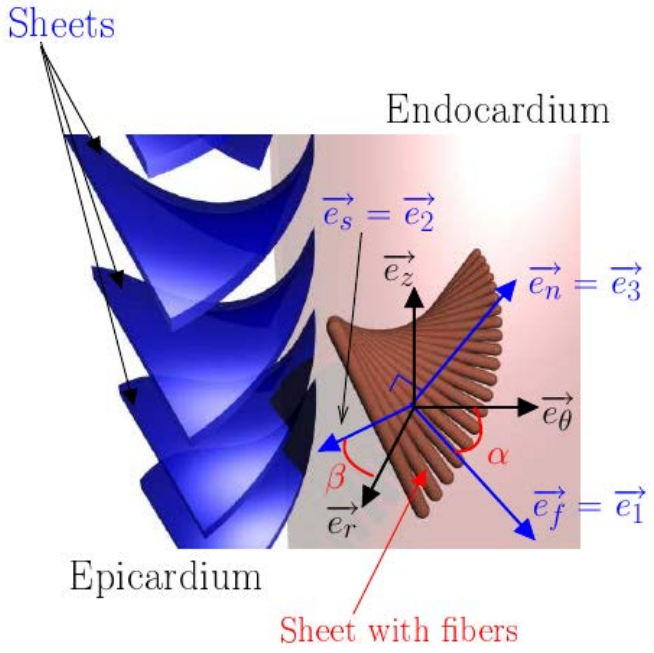

Figure 3.11: Illustration of fiber angle and sheet angle. $\mathbf{e}_1$, $\mathbf{e}_2$, and $\mathbf{e}_3$ are eigenvectors of the diffusion tensor with $\mathbf{e}_1$ associated to the largest eigenvalue, and $\mathbf{e}_3$ associated to the smallest eigenvalue. $(\mathbf{e}_r, \mathbf{e}_\theta, \mathbf{e}_z)$ are the cylindrical coordinates. $\mathbf{e}_f = \mathbf{e}_1$ is the fiber direction, $\mathbf{e}_s = \mathbf{e}_2$ is the sheet direction, and $\mathbf{e}_n$ is the normal component. α is the fiber angle and β the sheet angle. (from [Rohmer *et al.* (2006)a])

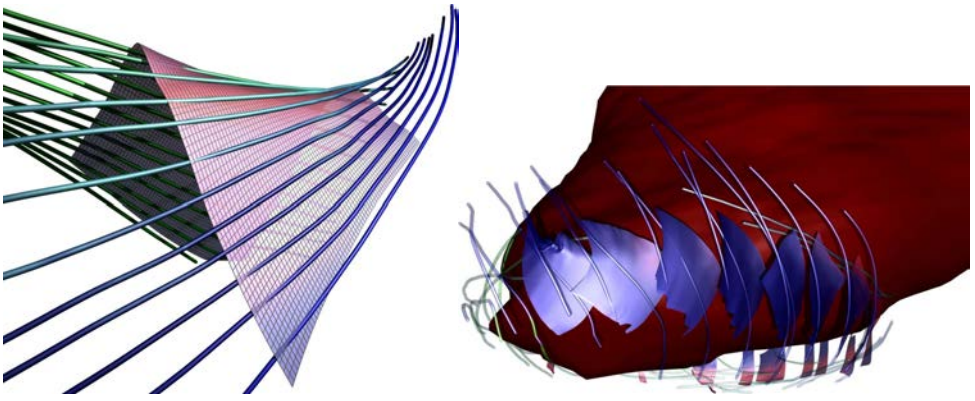

(a) (b)

Figure 3.12: Visualization of cardiac fibers and sheets. The fibers are located in sheets that have transmural structure. (a) A sheet of parameterized reconstructed surface with fibers (b) Reconstruction of the sheets in the apex shown with fibers. (From [Rohmer *et al.* (2006)a].)

in the middle myocardium, and run circumferentially with a small helix angle between $-20°$ and $20°$. The fiber tracts in the middle and upper left ventricle are generally longer than those near the apex.

Fiber tract clustering In [Frindel *et al.* (2009)b], a cardiac fiber clustering method is proposed to perform automatic classification of cardiac myofibers and to find inter-patient correspondences. Geometrical and topological clustering strategies and three fiber tract representation modes are compared. The results show that cardiac fiber traces can be partitioned differently depending on the choice of clustering strategies and fiber tract representation modes.

Fiber tract coherence In [Hlawitschka *et al.* (2010)] Hlawitschka et al. proposed a coherence measure for fiber tracts passing through a small neighborhood. This measure allows identification and segmentation of coherent fiber regions, and emphasizes regions where the behavior of fiber tracts changes. It is defined using infinitesimal deviations of neighboring fiber tracts and in terms of the deviation of fibers over a finite distance in practice (the distance provides a intuitive notion of scale in the assessment of coherence). The result provides a structural picture of data sets at a sub-voxel scale (see Fig. 3.13). Note that similar concepts have has been applied to visualize the coherence of motion among neighboring particles [Garth *et al.* (2007)]. The coherence measure is also studied in [Hlawatsch *et al.* (2011)] for DT-MRI data.

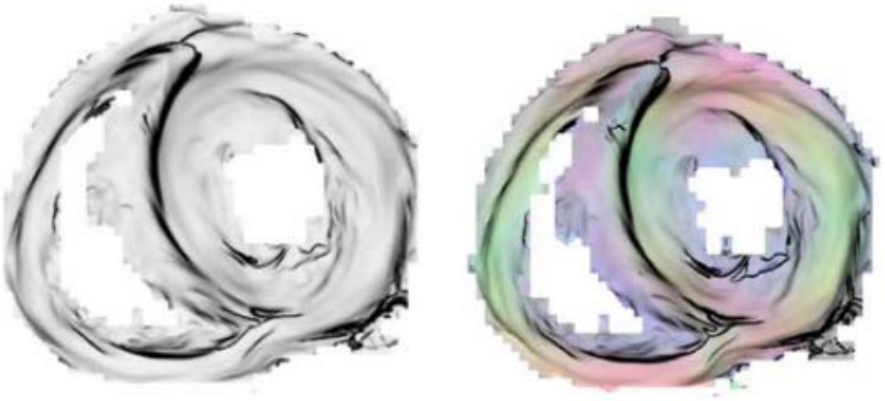

Figure 3.13: Two slice visualizations of a coherence map computed from the data set of a canine heart: on the left, shown in gray scale; on the right, colored by directional information. (from [Hlawitschka *et al.* (2010)])

Tractographic coherence index (TCI) The cardiac fiber helix angle varies from about $-70°$ in subepicardium to $70°$ in the subendocardium, and cardiac fibers in the midmyocardium are circumferential [LeGrice *et al.* (2001)]. In DT-MRI, the helix angle is usually defined voxel-wise by the inclination of the principal eigenvector with respect

to the short axis plane. The cardiac fiber helix angle is commonly used to describe the cardiac fiber architecture [Garrido *et al.* (1994), Reese *et al.* (1995)].

Rather than making observations in two dimension, Mekkaoui et al. [Mekkaoui *et al.* (2012)] introduced a tractography-based (or tract-based) quantitative framework to characterize the three dimensional fiber anatomy in the heart. The median, mean, maximum, or minimum helix angle along a fiber tract is assigned to fiber tracts to perform statistical fiber-wise classification. The tractographic coherence index (TCI) is derived in terms of these helix angles:

$$\mathrm{TCI} = \frac{\int_{\mathrm{endo}}^{\mathrm{epi}} (\mathrm{HA}_{\mathrm{med}}(x))^2 dx}{\int_{\mathrm{endo}}^{\mathrm{epi}} (\mathrm{HA}_{\mathrm{max}}(x) - \mathrm{HA}_{\mathrm{med}}(x))^2 dx + \int_{\mathrm{endo}}^{\mathrm{epi}} (\mathrm{HA}_{\mathrm{min}}(x) - \mathrm{HA}_{\mathrm{med}}(x))^2 dx}, \tag{3.5}$$

where $\mathrm{HA}_{\mathrm{max}}$, $\mathrm{HA}_{\mathrm{med}}$ and $\mathrm{HA}_{\mathrm{min}}$ are mean maximum, median and minimum helix angle (HA) respectively, and $\int_{\mathrm{endo}}^{\mathrm{epi}}$ indicates that the interval is from the border of endocardium to the border of epicardium.

A positive shift in the helix angle in the remodeled zone is observed in all layers of the myocardium, and the shift is greatest in the subepicardium. This shift is detected by visual inspection of the fiber tracts and is quantified using histograms; is confirmed by histology under phase-contrast microscopy.

The TCI values were calculated for normal and remodeled myocardia for different fiber lengths and image resolutions. The small difference between these TCI values indicates that the positive shift in fiber orientation within the remote zone occurs in a coherent way along the length of the myofiber.

II Contributions

Chapter 4

A neighborhood-based probabilistic approach for fiber tracking in human cardiac DTI[1]

Hongying Li, Marc Robini, Feng Yang, and Yuemin Zhu

4.1 Résumé

Les techniques de suivi des fibres ou la tractographie sont essentielles pour représenter et visualiser l'architecture des fibres cardiaques dans DTI. Nous proposons une méthode probabiliste de tractographie. Il pend en compte la corrélation spatiale des fibres dans un voisinage. La méthode consiste à calculer une distribution pondérée locale de l'orientation, et d'échantillonner une direction pour prolonger la fibre. Des résultats expérimentaux sur des données synthétiques et sur des données cardiaques humaines réelles montrent que, la méthode proposée est plus robuste au bruit et produit des fibres plus lisses et plus cohérentes que la méthode streamline.

[1] *ISBI 2012*, pages 9-13.

4.2 Abstract

Fiber tracking techniques are essential for representing and visualizing the cardiac fiber architecture information encoded in diffusion-tensor imaging (DTI) data. We propose a neighborhood-based probabilistic fiber tracking method for cardiac DTI which accounts for spatial correlation and data uncertainty. The method consists in tracking fiber paths by sampling step directions from a normalized weighted sum of local fiber orientation probability distributions. The sum is over a predefined neighborhood of the current position in the fiber path, and the weights depend on fractional anisotropy, angular change and distance to the current position. Experimental results on synthetic data and on real human cardiac data show that, compared to the streamlining approach, the proposed method is meaningfully more robust to noise and produces smoother and more consistent fibers.

4.3 Introduction

Fiber tracking techniques are essential for representing and visualizing the fiber architecture information encoded in diffusion-tensor imaging (DTI) data [Basser *et al.* (1994)]. Standard tracking methods such as streamlining generate fiber paths from tensor fields or from principal eigenvector fields [Basser *et al.* (2000)] without taking data uncertainty into account. Consequently, standard tracking methods usually require some preprocessing to remove noise and artifacts from the raw diffusion-weighted (DW) data (or from the tensor field extracted from the DW data, or from the principal eigenvector field computed from the tensors). Fiber tracking can be improved by resorting to global optimization or probabilistic modeling. Global methods have a better ability to extract fiber bundles from human brain data [Fillard *et al.* (2011)] or from low SNR human cardiac data [Frindel *et al.* (2010)], but they are computationally very expensive. Probabilistic tracking methods explicitly account for data uncertainty by describing the local fiber orientation via a posterior probability distribution that incorporates data likelihood and prior information [Behrens *et al.* (2003), Friman *et al.* (2006)] (fiber paths are generated by following the directions randomly sampled from this posterior), but they do not exploit the spatial correlation of the fiber orientations that is observed in the cardiac muscle tissue architecture.

In this paper, we propose an efficient probabilistic method that takes spatial correlation into account. The method consists in tracking fiber paths by sampling step directions from a normalized weighted sum of local fiber orientation probability distributions. The sum is over a predefined neighborhood of the current position in the fiber path, and the weights depend on fractional anisotropy, angular change and distance to the current position. Our method is described in the next section. We provide experimental results on synthetic data and on real human cardiac data in Section 4.5.

4.4 Tracking process formulation

The raw DTI data produced by MRI machines consists in N DW volumes associated with each gradient direction $g^{(i)}$, $i \in [\![1, N]\!]$ ($[\![1, N]\!]$ is a shorthand notation for $\{1, \dots N\}$). Each raw DW volume $y^{(i)}$ is defined on a 3-D voxel lattice V, and we let $y_v^{(i)}$ denote the intensity of $y^{(i)}$ at voxel $v \in V$. Assuming that the SNR is sufficiently high, the observed voxel intensities can be modeled by taking the logarithm of the true voxel intensities and adding the realizations of independent Gaussian random variables [Salvador *et al.* (2005)], that is, for any $i \in [\![1, N]\!]$ and any $v \in V$,

$$\ln y_v^{(i)} \;=\; \ln \mu_v^{(i)} + \varepsilon_v^{(i)} \tag{4.1}$$

with $\varepsilon_v^{(i)} \sim \mathcal{N}\Big(0, \Big(\sigma_v / \mu_v^{(i)}\Big)^2\Big)$. In this case, the conditional distribution of the log-transformed data $\mathbf{z}_v = \Big(\ln(y_v^{(1)}), \dots, \ln(y_v^{(N)})\Big)$ given $\boldsymbol{\mu}_v = (\mu_v^{(1)}, \dots, \mu_v^{(N)})$ and the residual noise standard deviation σ_v writes

$$\mathrm{P}(\mathbf{z}_v |\, \boldsymbol{\mu}_v, \sigma_v) \;=\; \prod_{i=1}^{N} \frac{\mu_v^{(i)}}{\sigma_v \sqrt{2\pi}} \exp\left(- \frac{(\mu_v^{(i)})^2}{2\sigma_v^2} \left(\ln \frac{y_v^{(i)}}{\mu_v^{(i)}} \right)^2 \right). \tag{4.2}$$

To express the data likelihood in terms of the principal diffusion direction field — denote it by $\{\mathbf{v}_v \in \mathbb{U};\, v \in V\}$ with $\mathbb{U}$ being the unit sphere — we model the true DW data $\boldsymbol{\mu}$ using the constrained model proposed in [Friman and Westin (2005)]. This model is obtained by assuming that the two smallest eigenvalues of each diffusion tensor $\mathbf{D}_v$ are equal; it approximates $\boldsymbol{\mu}_v$ by a function of $\mathbf{v}_v$ that is parameterized by a set $\boldsymbol{\theta}_v$ of parameters computed from the eigen-decomposition of $\mathbf{D}_v$. The modified likelihood is given by

$$\mathrm{P}(\mathbf{z}_v |\, \mathbf{v}_v = \mathbf{u}, \boldsymbol{\theta}_v, \sigma_v) \;=\; \mathrm{P}(\mathbf{z}_v |\, \boldsymbol{\mu}_v = \widehat{\boldsymbol{\mu}}(\mathbf{u}; \boldsymbol{\theta}_v), \sigma_v), \tag{4.3}$$

where $\widehat{\boldsymbol{\mu}}(\,\cdot\,; \boldsymbol{\theta}_v)$ is the constrained-model approximation of the true voxel intensities: letting $\lambda_{1,v}$, $\lambda_{2,v}$ and $\lambda_{3,v}$ be the eigenvalues of $\mathbf{D}_v$ with $\lambda_{1,v} \geqslant \lambda_{2,v} \geqslant \lambda_{3,v}$, we have

$$\widehat{\mu}^{(i)}(\mathbf{u}; \boldsymbol{\theta}_v) \;=\; \mu_v^{(0)} \exp\Big(- b^{(i)} \Big(\theta_{v,1} + \theta_{v,2} \langle g^{(i)}, \mathbf{u} \rangle^2 \Big) \Big) \tag{4.4}$$

$$\text{with} \quad \theta_{v,1} = \frac{\lambda_{2,v} + \lambda_{3,v}}{2} \quad \text{and} \quad \theta_{v,2} = \lambda_{1,v} - \theta_{v,1}, \tag{4.5}$$

where $\langle \cdot, \cdot \rangle$ denotes the standard Euclidean dot product, $\mu^{(0)}$ is the true non-diffusion-weighted volume (in practice, $\mu^{(0)}$ is replaced by the estimate $\widehat{\mu}^{(0)}$ obtained by denoising its experimental measurement $y^{(0)}$ using the edge-preserving regularization technique described in [Frindel *et al.* (2009)a]), and the gradient directions $g^{(i)}$ and the b-values $b^{(i)}$ are known experimental parameters.

If we do not assume any prior knowledge on the diffusion direction or on the raw data,

the function $\mathbf{u} \in \mathbb{U} \mapsto \mathrm{P}(\mathbf{z}_v | \, \mathbf{v}_v = \mathbf{u}, \boldsymbol{\theta}_v, \sigma_v)$ is proportional to the diffusion direction probability map at voxel v. The likelihood (4.3) is "voxel-wise": it only uses the information attached to the voxel under consideration, and thus it does not take into account the spatial correlation inherent to DTI data eligible for fiber tracking. To overcome this weakness, we propose to define the likelihood at a given voxel v as a weighted sum of the voxel-wise likelihoods within a spatial neighborhood of v. We give more weights to the voxels where the FA is high and to the voxels that define a small angular change in the direction of the fiber being tracked. More precisely, let $\mathcal{G}$ be a neighborhood system on V, that is, a collection $\mathcal{G} = \{\mathcal{G}(v) \, ; \, v \in V\}$ of subsets of V such that (i) $v \notin \mathcal{G}(v)$ for all $v \in V$, and (ii) $w \in \mathcal{G}(v) \Longleftrightarrow v \in \mathcal{G}(w)$ for all $(v, w) \in V^2$. Let $w \in \mathcal{G}(v)$ be a neighbor of the current voxel v, let $\mathbf{c}_w$ be the center of w, and let $\overrightarrow{\mathbf{s}_{k-1}\mathbf{s}_k}$, $\mathbf{s}_k \in v$, be the last computed fiber segment (see Fig. 4.1). Then, the weight assigned to w is given by

$$\xi_k(w) \; = \; (\mathrm{FA}(w))^{\alpha} |\cos(\varphi_k(\mathbf{c}_w))|^{\beta} \tag{4.6}$$

$$\text{with} \quad \cos(\varphi_k(\mathbf{a})) \; = \; \frac{\left\langle \overrightarrow{\mathbf{s}_{k-1}\mathbf{s}_k}, \overrightarrow{\mathbf{s}_k\mathbf{a}} \right\rangle}{\left\| \overrightarrow{\mathbf{s}_{k-1}\mathbf{s}_k} \right\| \left\| \overrightarrow{\mathbf{s}_k\mathbf{a}} \right\|}, \tag{4.7}$$

where α and β are positive parameters that control the influence of FA and angular change in the weighting process — note that the angular weight is symmetric with respect to $\pi/2$, so that forward and backward tracking of a given fiber are equally likely. We also weight the influence of the neighbors by a decreasing function of their distance to the current fiber position $\mathbf{s}_k$. Denoting this function by ρ, the weighted likelihood is defined by

$$\begin{aligned} &\mathrm{P}(\mathbf{z}_v | \, \mathbf{v}_v = \mathbf{u}, \mathbf{s}_{k-1}, \mathbf{s}_k, \boldsymbol{\theta}_v, \sigma_v) \\ &\propto \sum_{w \in \mathcal{G}(v) \cup \{v\}} \rho\Big(\Big\| \overrightarrow{\mathbf{s}_k\mathbf{c}_w} \Big\| \Big) \xi_k(w) \mathrm{P}(\mathbf{z}_w | \, \mathbf{v}_w = \mathbf{u}, \boldsymbol{\theta}_w, \sigma_w), \end{aligned} \tag{4.8}$$

where it is understood that $\mathbf{s}_k \in v$.

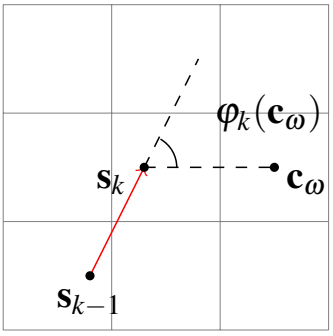

Figure 4.1: Angular change used for weighting a neighbor w of the center voxel v: $\varphi_k(\mathbf{c}_w)$ is the angle between the last computed fiber segment going from $\mathbf{s}_{k-1}$ to $\mathbf{s}_k \in v$ and the vector going from the current position $\mathbf{s}_k$ to the center $\mathbf{c}_w$ of w.

Following [Friman *et al.* (2006)], the prior knowledge about fiber regularity is modeled by a conditional probability $\mathrm{P}(\mathbf{s}_{k+1}|\mathbf{s}_{k-1},\mathbf{s}_k)$ that encourages the new step direction $\overrightarrow{\mathbf{s}_k\mathbf{s}_{k+1}}$ to be close to the previous step direction $\overrightarrow{\mathbf{s}_{k-1}\mathbf{s}_k}$ and which decreases to zero as the angle between $\overrightarrow{\mathbf{s}_{k-1}\mathbf{s}_k}$ and $\overrightarrow{\mathbf{s}_k\mathbf{s}_{k+1}}$ goes to $\frac{\pi}{2}$:

$$\mathrm{P}(\mathbf{s}_{k+1}|\,\mathbf{s}_{k-1},\mathbf{s}_k) \propto \begin{cases} (\cos\varphi_k(\mathbf{s}_{k+1}))^\gamma & \text{if } \cos\varphi_k(\mathbf{s}_{k+1})>0, \\ 0 & \text{otherwise,} \end{cases} \tag{4.9}$$

where $\cos\varphi_k(\cdot)$ is given by (4.7) and the parameter $\gamma \geqslant 0$ controls the fiber regularity degree (the larger γ, the more regular the reconstructed fibers). Note that the probability is zero for angular changes greater than $\frac{\pi}{2}$ in order to prevent fibers from going backwards.

Finally, the combination of the weighted likelihood (4.8) together with the prior (4.9) gives the posterior distribution used for sampling the local fiber directions:

$$\begin{aligned} \mathrm{P}\Big(\mathbf{s}_{k+1}=\mathbf{s}_k+\delta\mathbf{u}\,\Big|\,\mathbf{z}_{v_k},\mathbf{s}_{k-1},\mathbf{s}_k,\boldsymbol{\theta}_{v_k},\sigma_{v_k}\Big) \\ \propto\ \mathrm{P}\Big(\mathbf{z}_{v_k}\,\Big|\,\mathbf{v}_{v_k}=\mathbf{u},\mathbf{s}_{k-1},\mathbf{s}_k,\boldsymbol{\theta}_{v_k},\sigma_{v_k}\Big) \\ \times\,\mathrm{P}\Big(\mathbf{s}_{k+1}=\mathbf{s}_k+\delta\mathbf{u}\,\Big|\,\mathbf{s}_{k-1},\mathbf{s}_k\Big), \end{aligned} \tag{4.10}$$

where v_k denotes the voxel in which $\mathbf{s}_k$ lies and $\delta>0$ is the step length of the tracking process. A fiber path is generated by iteratively sampling step directions from (4.10), starting from a given seed point $\mathbf{s}_0$ and until the curvature exceeds a user-defined threshold τ (the curvature κ at a point $\mathbf{s}$ of a fiber path $\mathfrak{F}$ is the reciprocal of the radius of the osculating circle of $\mathfrak{F}$ at $\mathbf{s}$).

On the practical side, the unit sphere $\mathbb{U}$ is restricted to a finite set $\mathbb{U}_0$ of possible step directions in order to facilitate the sampling process. The first step direction is sampled from

$$\begin{aligned} \mathrm{P}\Big(\mathbf{s}_1=\mathbf{s}_0+\delta\mathbf{u}\,\Big|\,\mathbf{z}_{v_0},\mathbf{s}_0,\boldsymbol{\theta}_{v_0},\sigma_{v_0}\Big) \\ \propto \sum_{w\in\mathcal{G}(v_0)\cup\{v_0\}} \rho\Big(\Big\|\overrightarrow{\mathbf{s}_0\mathbf{c}_w}\Big\|\Big)(\mathrm{FA}(w))^\alpha \\ \times\,\mathrm{P}(\mathbf{z}_w|\,\mathbf{v}_w=\mathbf{u},\boldsymbol{\theta}_w,\sigma_w), \end{aligned} \tag{4.11}$$

and the residual noise variance σ_v^2 is approximated by

$$\widehat{\sigma}_v^2 = \frac{1}{N-5}\sum_{i=1}^{N}(y_v^{(i)}-\widehat{\mu}^{(i)}(\mathbf{v}_v^\star;\boldsymbol{\theta}_v))^2, \tag{4.12}$$

where $\mathbf{v}_v^\star$ is the unit principal eigenvector of $\mathbf{D}_v$ (we divide by $N-5$ because the constrained-model approximation has 5 parameters, namely, $\theta_{1,v}$, $\theta_{2,v}$ and the vector components of

the principal diffusion direction). The procedure for generating a fiber path $\mathbf{s}_0, \mathbf{s}_1, \ldots, \mathbf{s}_K$ given the seed $\mathbf{s}_0$ is the following (given a PDF f on $\mathbb{U}$, we call the restriction of f to $\mathbb{U}_0$ the PDF $\mathbf{u} \in \mathbb{U}_0 \mapsto f(\mathbf{u}) / \sum_{\mathbf{v} \in \mathbb{U}_0} f(\mathbf{v})$).

$\diamond$ set $k \leftarrow 0$ and $\kappa \leftarrow 0$;
while $\kappa \leqslant \tau$ **do**
  $\diamond$ add $\mathbf{s}_k$ to the fiber path;
  for each $v \in \mathcal{G}(v_k) \cup \{v_k\}$ **do**
    $\diamond$ estimate the tensor $\mathbf{D}_v$ from the raw DTI data;
    $\diamond$ compute the eigen-decomposition of $\mathbf{D}_v$;
    $\diamond$ compute $\boldsymbol{\theta}_v = \{\theta_{1,v}, \theta_{2,v}\}$ (see (4.5));
    $\diamond$ estimate the residual noise variance σ_v^2 (see (4.12));
    $\diamond$ compute the restriction of the modified likelihood $\mathrm{P}(\mathbf{z}_v | \, \mathbf{v}_v = \mathbf{u}, \boldsymbol{\theta}_v, \sigma_v)$ (see (4.3)) to $\mathbb{U}_0$;
  end(for)
  if $k = 0$ **then**
    $\diamond$ compute the restriction to $\mathbb{U}_0$ of the weighted likelihood (4.11) and draw $\mathbf{u}_0$ from it;
    $\diamond$ set $\mathbf{s}_1 \leftarrow \mathbf{s}_0 + \delta \mathbf{u}_0$;
  else
    $\diamond$ compute the restrictions to $\mathbb{U}_0$ of the weighted likelihood (4.8) and of the prior (4.9);
    $\diamond$ form the restriction to $\mathbb{U}_0$ of the posterior (4.10) and draw $\mathbf{u}_k$ from it;
    $\diamond$ set $\mathbf{s}_{k+1} \leftarrow \mathbf{s}_k + \delta \mathbf{u}_k$;
    $\diamond$ estimate the curvature κ at $\mathbf{s}_k$ of an interpolation of the fiber path $\mathbf{s}_0, \ldots, \mathbf{s}_{k+1}$;
  end(if)
  $\diamond$ set $k \leftarrow k + 1$;
end(while)

4.5 Experiments

4.5.1 The data

We assess our method using both synthetic and human cardiac DTI data.

Synthetic data

The synthetic data is generated from a spiral-shaped tensor field of size $50 \times 50 \times 20$. Fig. 4.2 shows a slice of synthetic helix curve tangents, which are assigned to voxels as the principal eigenvectors of the synthetic tensors. Note that only the synthetic helix curves passing through the red points are displayed , and the helix curves are colored by their helix angles calculated curve-wise instead of voxel-wise. More precisely, we compute the elevation angle of a curve with the xy plan instead of using the angle between the xy plan and the principal eigenvector at each voxel. We set the sign of the helix angles according to the spiral pattern of the curve segment. The helix angle is positive along a curve segment with right-handed spiral pattern, and it is negative for a left-handed one. The spiral pattern is determined as follows:

$$g = \tau_z \cdot (\mathbf{r} \times \tau)_z \tag{4.13}$$

where τ is the tangent vector, τ_z is the z component, the subscript z of τ_z indicates the rotation axis of the curve, $\mathbf{r}$ is the radius vector pointing to the element. If $g > 0$, the spiral pattern is right-handed, otherwise it is left-handed [Zhukov and Barr (2003)].

The diffusion tensor at voxel v is given by

$$\mathbf{D_v} = \mathbf{e}_{1,v}\mathbf{e}_{1,v}^T + \frac{1}{2}\Big(\mathbf{e}_{2,v}\mathbf{e}_{2,v}^T + \mathbf{e}_{3,v}\mathbf{e}_{3,v}^T\Big), \tag{4.14}$$

where the unit eigenvectors $\mathbf{e}_{1,v}$, $\mathbf{e}_{2,v}$ and $\mathbf{e}_{3,v}$ are defined as follows:

- the principal eigenvector $\mathbf{e}_{1,v}$ is parallel to the local tangent of the helix curve and perpendicular to the radial direction (the angle between $\mathbf{e}_{1,v}$ and the xy plane ranges from $-65°$ to $+65°$);
- $\mathbf{e}_{2,v}$ is parallel to the xy plane and points towards the z-axis;
- $\mathbf{e}_{3,v} = \mathbf{e}_{1,v} \wedge \mathbf{e}_{2,v}$.

The corresponding DW volumes are computed by using the Stejskal-Tanner diffusion equations with a constant non-diffusion-weighted signal.

To study the robustness of the proposed fiber tracking method, Gaussian noise is added to the DW images. The values of the noise variance are normalized by the maximum DW intensity and no noise is added to the non-diffusion weighted volume. Fig. 4.3 shows the peak signal-to-noise ratio (PSNR) as a function of the noise variance. The noise variance varies from 0.001 to 0.8, while the corresponding PSNR ranges from 40.10 dB to 7.21 dB. Fig. 4.4 shows the synthetic noisy DW images with different noise variances. Fig. 4.5 shows the principal eigenvectors of one slice of estimated tensors.

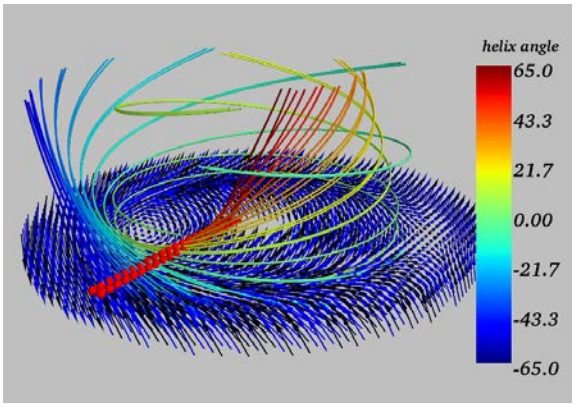

Figure 4.2: Some synthetic fiber paths shown with a slice of principal eigenvectors. The selected fiber paths are those passing through the red points. Note that the whole principal vector field consists of twenty slices of the principal eigenvectors shown here. The principal eigenvector at a given voxel is set to be parallel to the tangent of the helix curve at the center of the voxel.

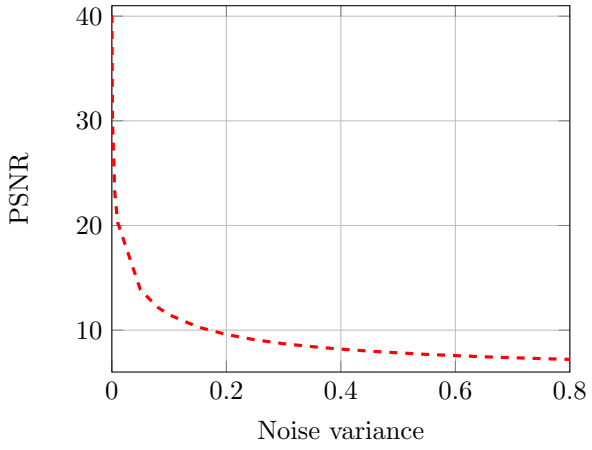

Figure 4.3: Peak signal-to-noise ratio (PSNR) plotted with respect to noise variance.

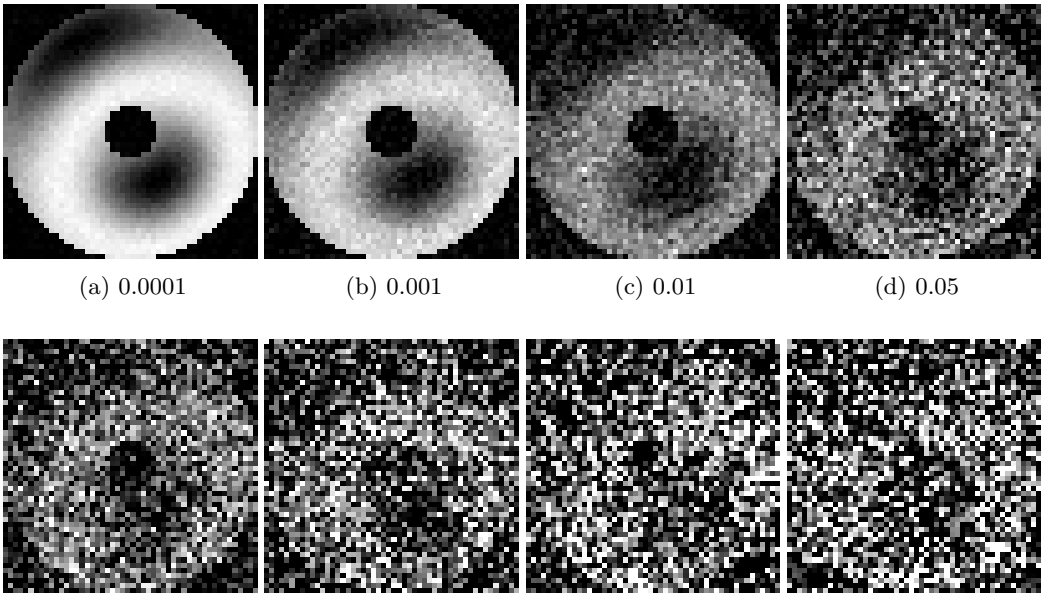

(a) 0.0001 (b) 0.001 (c) 0.01 (d) 0.05

(e) 0.1 (f) 0.2 (g) 0.3 (h) 0.4

Figure 4.4: Synthetic noisy DW images with different noise levels indicated by the normalized variance.

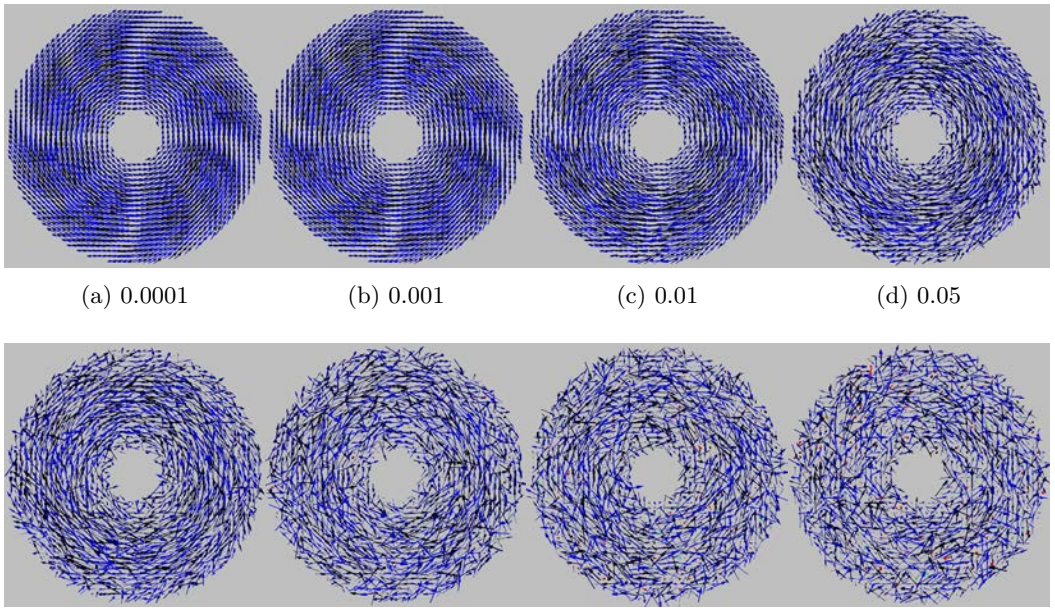

(a) 0.0001 (b) 0.001 (c) 0.01 (d) 0.05

(e) 0.1 (f) 0.2 (g) 0.3 (h) 0.4

Figure 4.5: Principal eigenvectors of one slice of estimated tensors from the synthetic noisy DW images.

Cardiac data

The real data consists of ex-vivo human cardiac data acquired with a Siemens 1.5 T Magnetom Avanto in the Cardiology Hospital of Lyon with the following settings: TE = 98 ms, TR = 8600 ms, FOV = $256 \times 256\,\mathrm{mm}^2$, slice thickness = 2 mm, number of slices = 52, slice size = 128×128, diffusion sensitivity $b = 1000\,\mathrm{s \cdot mm^{-2}}$, gradient directions = 12. The sequence used was a 2D EPI diffusion-weighted sequence with a twice-refocused diffusion preparation.

4.5.2 Parameter setting and performance evaluation

We compare the performance of the proposed method to the standard streamlining approach. For our method, we take $\mathcal{G}(v)$ to be the set of nearby voxels within a radius of r times the voxel size d, that is,

$$\mathcal{G}(v) = \left\{ w \in V \setminus \{v\} \;\middle|\; \|\overrightarrow{\mathbf{c}_v\mathbf{c}_w}\| \leqslant rd \right\} \tag{4.15}$$

(thus $r = \sqrt{3}$ corresponds to the 26 nearest-neighbor system), and the attenuation function ρ is defined by

$$\rho(t) = \exp(\frac{-t^2}{2\varsigma^2}), \tag{4.16}$$

where the standard deviation ς is set to $rd/2$. The parameters α and β of the weighting function are set to 2.0, the parameter γ of the prior is set to 1.0, the step length δ is set to half the voxel size (that is, 1 mm for the real cardiac data), and the curvature threshold τ used for the termination of the tracking process is set to $1/\delta$. The streamlining approach uses a fourth-order Runge-Kutta integration scheme with integration step δ, and the criteria used for stopping the tracking are thresholds on FA (FA < 0.1) and on curvature ($\kappa \leqslant 1/\delta$).

To assess the relative performances of the fiber tracking methods in the case of the synthetic data, we measure the adequation of a reconstructed fiber path $\mathfrak{F}$ to the noise-free tensor distribution by computing the error term

$$\mathcal{E}(\phi) = \frac{1}{L(\phi)} \int_0^L \left(1 - \frac{\|\mathbf{D}_{\phi(l)}\,\phi'(l)\|}{\|\phi'(l)\| \left\|\mathbf{D}_{\phi(l)}\right\|} \right) \|\phi'(l)\|\,\mathrm{d}l\,, \tag{4.17}$$

where $\phi : [0, L] \longrightarrow \mathbb{R}^3$ is a quadratic spline interpolation of $\mathfrak{F}$, $L(\phi) = \int_0^L \|\phi'(l)\|\,\mathrm{d}l$ denotes the length of ϕ, $\mathbf{D}_{\phi(l)}$ is the tensor at $\phi(l)$, and $\left\| \cdot \right\|$ is the spectral norm induced by the standard Euclidean norm $\|\cdot\|$ (the term between parenthesis is equal to one if $\mathrm{FA}(\phi(l)) = 1$ and if $\phi'(l)$ is parallel to the diffusion direction, and it is zero if $\mathrm{FA}(\phi(l)) = 0$ or if $\mathrm{FA}(\phi(l)) = 1$ and $\phi'(l)$ is perpendicular to the diffusion direction). This error term is averaged over all generated fiber paths to obtain a mean fiber error measure.

In the case of the real data, the noise-free tensor distribution is not available and thus (4.17) cannot be used. We therefore consider the following quantitative criteria: number of fibers with length greater than 6mm, mean fiber-length, and median fiber-length.

4.5.3 Results

Tracking results on synthetic data

Fig. 4.7 shows the tracking results of the proposed method for the synthetic data in Fig. 4.4. Compared to the tracking results of streamlining (see Fig. 4.6), we observe that the proposed method is more robust to noise. When a large amount of noise is added, e.g., in the case of normalized variance equal to 0.3 to 0.8, we can hardly observe the helix curve in the tracking results of streamlining. By contrast, we can still observe this pattern in the tracking results of the proposed method.

Fig. 4.8 shows the mean fiber error as a function of the noise variance for streamlining and for the proposed method with $r = \sqrt{3}$ (r is defined in (4.15)). Note that the values of the noise variance are normalized by the maximum DW intensity and no noise is added to the non-diffusion weighted volume. For both methods, the fibers were initialized from the red point seeds shown in Fig. 4.2. We observe that the fibers generated by our method are always closer to the noise-free tensor data (in terms of the error measure (4.17)) than are the fibers produced by streamlining. Furthermore, the higher the noise level, the higher the improvement brought by our method over streamlining.

Tracking results on cardiac data

The fiber tracking results associated with our human cardiac data are shown in Fig. 4.9. The proposed method produces more regular and smoother fibers than does streamlining (we used $r = \sqrt{3}$ again). Quantitative results are given in Table 4.1 where both methods are compared in terms of the number of fibers, the mean fiber-length, and the median fiber-length. The proposed method outperforms streamlining in terms of all three criteria.

Tuning the parameter r

The parameter r defined in (4.15) is the ratio between the distance of the farthest neighbor to the current position and the voxel size. It controls the size of the neighborhood.

Fig. 4.10 displays the error plots for the tracking results of the proposed method with $r = \sqrt{3}$, 3, and 4 for the synthetic data. Fiber tracking is ran 100 times and the results were averaged. The produced fiber paths with $r = 3$ and with $r = 4$ are more accurate than

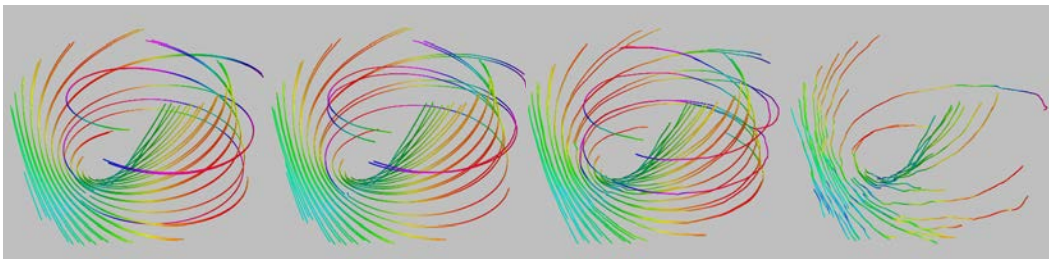

(a) 0.0001 (b) 0.001 (c) 0.01 (d) 0.05

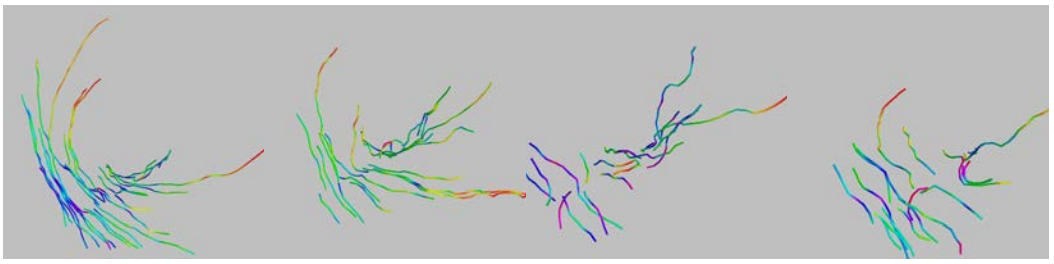

(e) 0.1 (f) 0.2 (g) 0.3 (h) 0.4

Figure 4.6: Fiber tracking results of streamlining for synthetic DW images with different noise variances. The fourth order Runge-Kutta integration method is used with trilinear interpolation on the principal eigenvector field to perform streamlining.

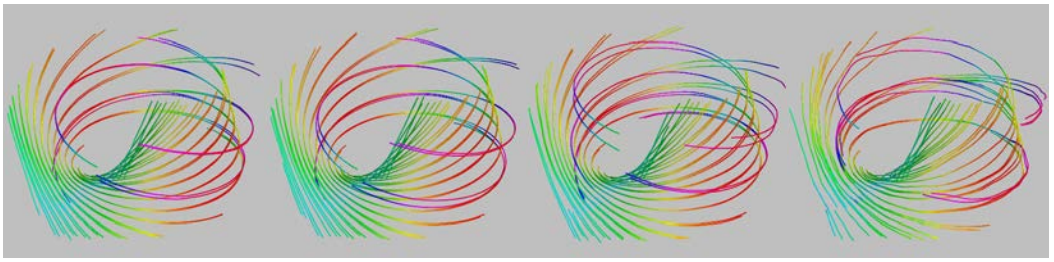

(a) 0.0001 (b) 0.001 (c) 0.01 (d) 0.05

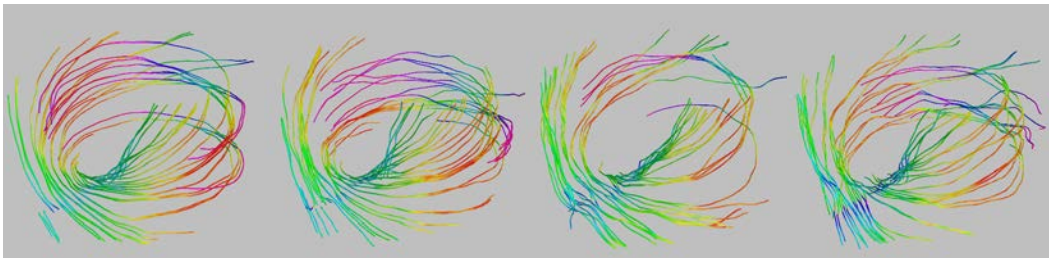

(e) 0.1 (f) 0.2 (g) 0.3 (h) 0.4

Figure 4.7: Fiber tracking results of the proposed method with $r = \sqrt{3}$ for synthetic DW images with different noise variances.

Table 4.1: Quantitative comparison between streamlining and the proposed method (real cardiac data).

	Number of fibers	Mean fiber-length	Median fiber-length
Streamlining	777	24.94mm	19.00mm
Proposed	1082	50.91mm	38.00mm

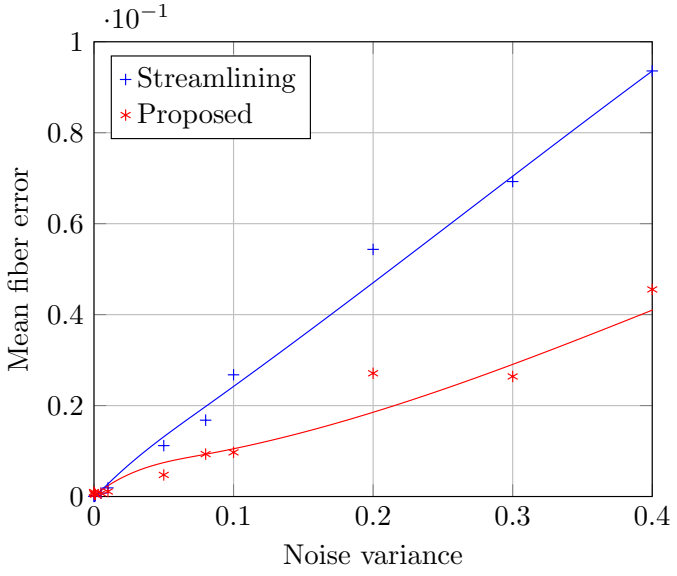

Figure 4.8: Mean fiber error as a function of the noise level for streamlining and for the proposed method (synthetic data).

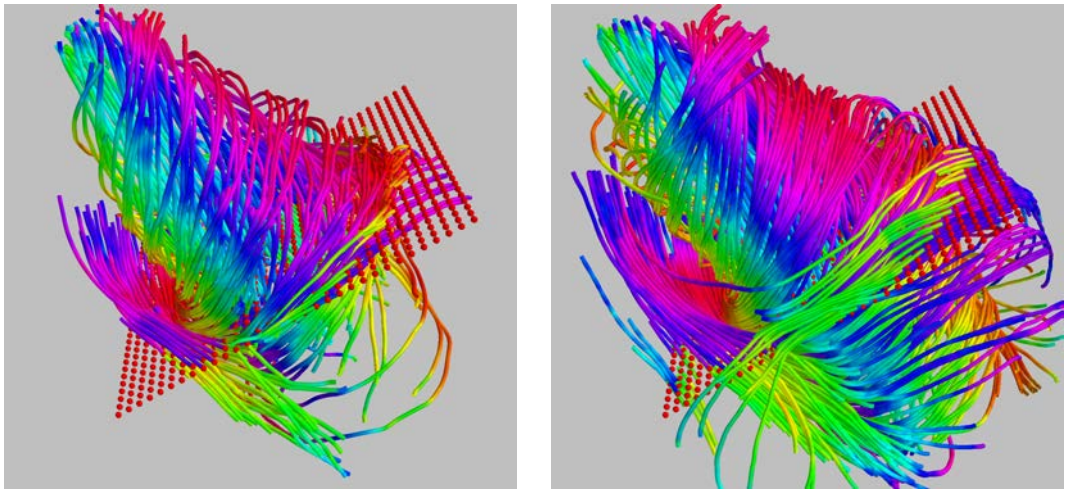

(a) **(b)**

Figure 4.9: Fibers tracked from the red point seeds using: (a) streamlining; (b) proposed method with $r = \sqrt{3}$.

the ones with $r = \sqrt{3}$ in the sense of the error term (4.17). However increasing r from 3 to 4 does not improve the accuracy of the reconstructed fiber paths.

In the case of the real cardiac data, the fiber density seems to increase when increasing r (Fig 4.11). In fact, according to Table 4.2, the mean fiber-length and the median fiber-length increase with increasing r, but the number of fibers decreases. The missing fiber positions are shown in Fig 4.13 and Fig 4.14; thy are spread in the myocardium without apparent regular patterns. Note that there are "strange" fibers in the case where $r = 4$ (see Fig. 4.11), which could explained by the large neighborhood for calculating the weighted likelihood.

The above shows that $r = 3$ is a good trade-off between accuracy and computation time for the proposed method.

Visualize weighted likelihood

Fig. 4.15 and Fig. 4.16 show the weighted likelihood and the original ones in the neighborhood. The weighted likelihood is calculated for the center of voxel (14,23,20) and voxel (32,11,20) respectively.

The weighted likelihood in Fig. 4.15 has a different shape from the original one. The weighted likelihood in Fig. 4.16 has a similar shape, but the direction is changed and well-aligned with the neighbor likelihoods. Note that the weighted likelihood is calculated in a three dimensional neighborhood, but only the neighborhood voxel likelihoods in the plane $z = 20$ are shown.

Revealing the fiber architecture complexity by local fiber tangents

Fig. 4.17 and Fig. 4.18 show the local tangents of fiber paths produced by the proposed method and streamlining, respectively. The "local fiber tangents" at a given voxel are defined as the tangents of the fiber paths at that voxel.

In Fig. 4.17, the varying directions of local fiber tangents at (14,23,20) show the potential complex fiber architecture at the "tri-intersect" area, that is, the area where the left and right ventricles intersect. By contrast, local fiber tangents follow nearly the same direction in the remaining part of the myocardium. Note that similar local fiber tangent patterns are also found at the symmetric position with respect to the center of the left ventricle (see voxel (41 20 20)).

Comparing streamlining to the proposed method, we notice that there are more areas containing disordered tangent directions in the streamlining results (see Fig. 4.18). This could result from the noise sensitivity of streamlining.

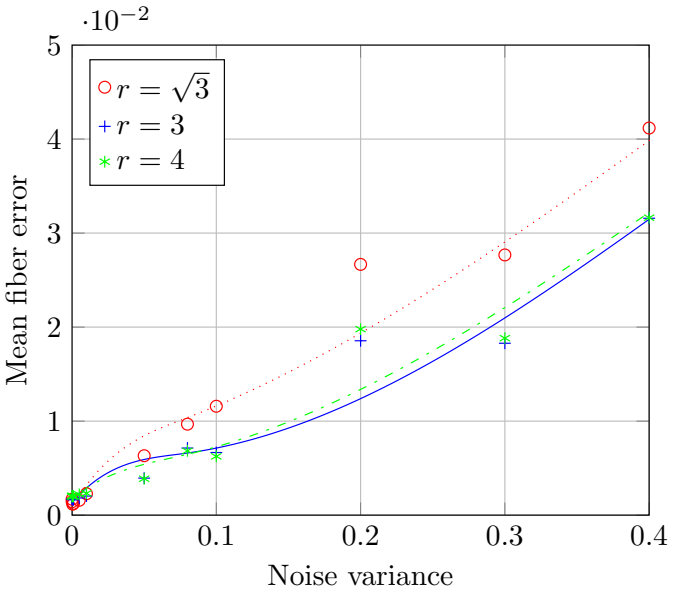

Figure 4.10: Error plots for the tracking results of the proposed method with $r = \sqrt{3}$, 3, and 4 (synthetic data, average 100 times).

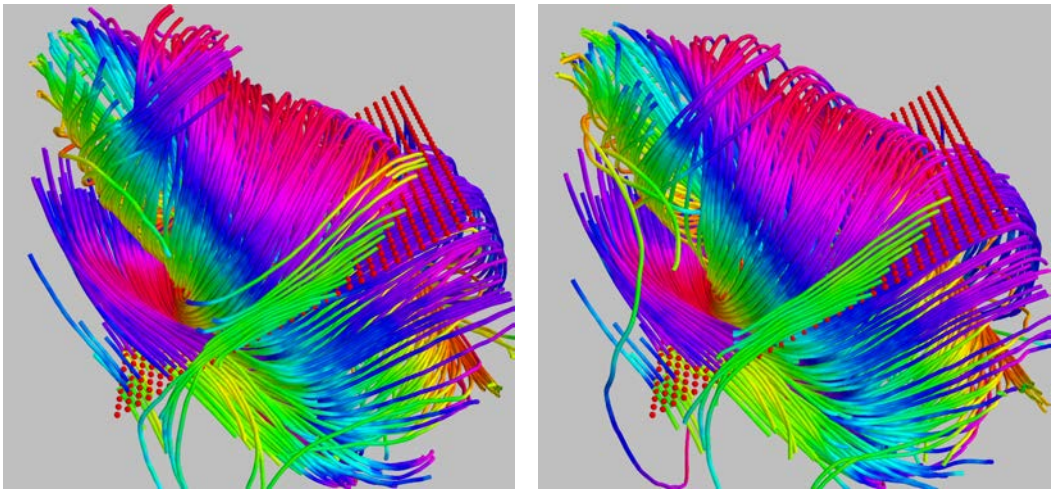

(a) **(b)**

Figure 4.11: Fiber tracked from the red point seeds using the proposed method: (a) $r = 3$; (b) $r = 4$. (The results corresponding to $r = \sqrt{3}$ are displayed in Fig. 4.9b.)

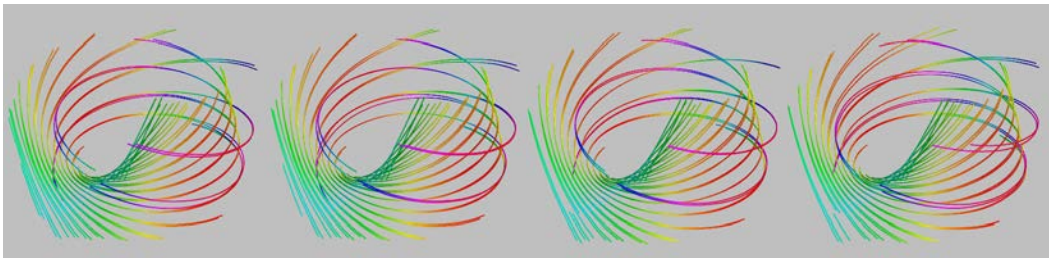

(a) 0.001,$r = \sqrt{3}$ (b) 0.001,$r = 2$ (c) 0.001,$r = 3$ (d) 0.001,$r = 4$

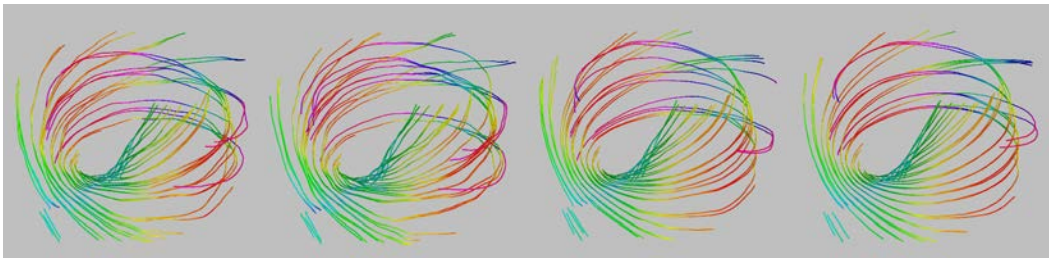

(e) 0.1,$r = 2$ (f) 0.1,$r = \sqrt{3}$ (g) 0.1,$r = 3$ (h) 0.1,$r = 4$

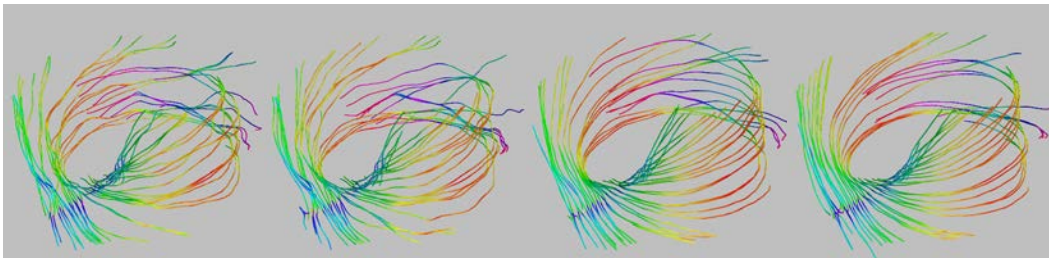

(i) 0.4,$r = \sqrt{3}$ (j) 0.4,$r = 2$ (k) 0.4,$r = 3$ (l) 0.4,$r = 4$

Figure 4.12: Comparison of tracking results obtained with $r = \sqrt{3}$, 2, 3, and 4 on the synthetic DW images with normalized noise variance equal to 0.001, 0.1, and 0.6.

Table 4.2: Quantitative results for different values of r (real cardiac data).

	Number of fibers	Mean fiber-length	Median fiber-length
$r = \sqrt{3}$	1082	50.91 mm	38.00 mm
$r = 3$	1039	69.95 mm	48.00 mm
$r = 4$	978	73.13 mm	47.00 mm

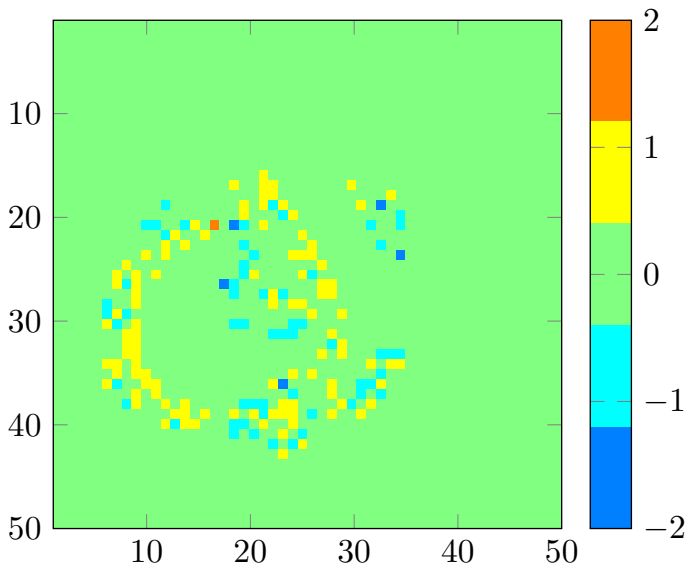

Figure 4.13: Missing fiber seed locations (between the proposed method with $r = \sqrt{3}$ and $r = 3$; positive values on the figure indicate the seed locations where more fibers are tracked with $r = \sqrt{3}$).

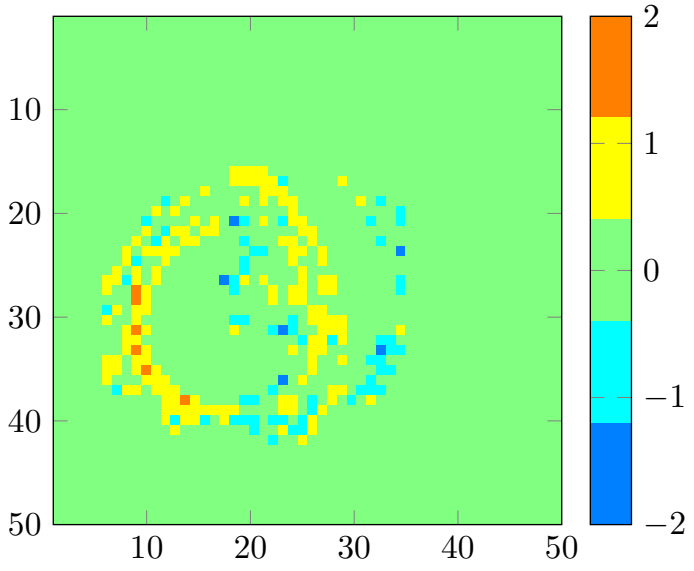

Figure 4.14: Missing fiber seed locations (between the proposed method with $r = \sqrt{3}$ and $r = 4$; positive values on the figure indicate the seed locations where more fibers are tracked with $r = \sqrt{3}$).

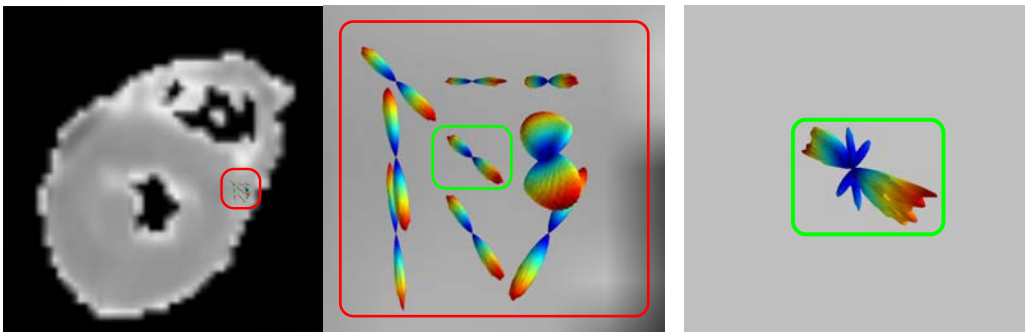

(a) Original voxel wise likelihoods (b) Zoomed in view of (a) (c) Weighted likelihood

Figure 4.15: Original likelihood distributions and weighted likelihood distribution for voxel (14 23 20). (a) Original likelihood distributions in the neighborhood on the $x-y$ plan. (b) Zoomed view of the likelihood distributions in (a). (c) The weighted likelihood distribution for the center voxel in (b).

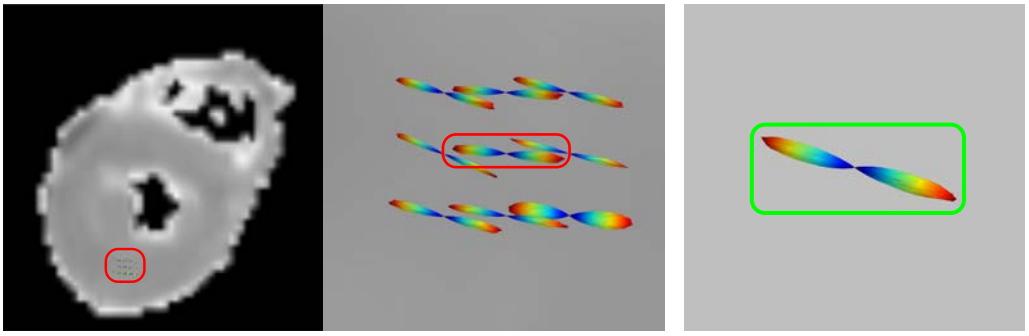

(a) Original voxel wise likelihoods (b) Zoomed in view of (a) (c) Weighted likelihood

Figure 4.16: Original likelihood distributions and weighted likelihood distribution for voxel (32 11 20). (a) Original likelihood distributions in the neighborhood on the xy plan. (b) Magnification view of the likelihood distributions in (a). (c) The weighted likelihood distribution for the framed voxel in (b).

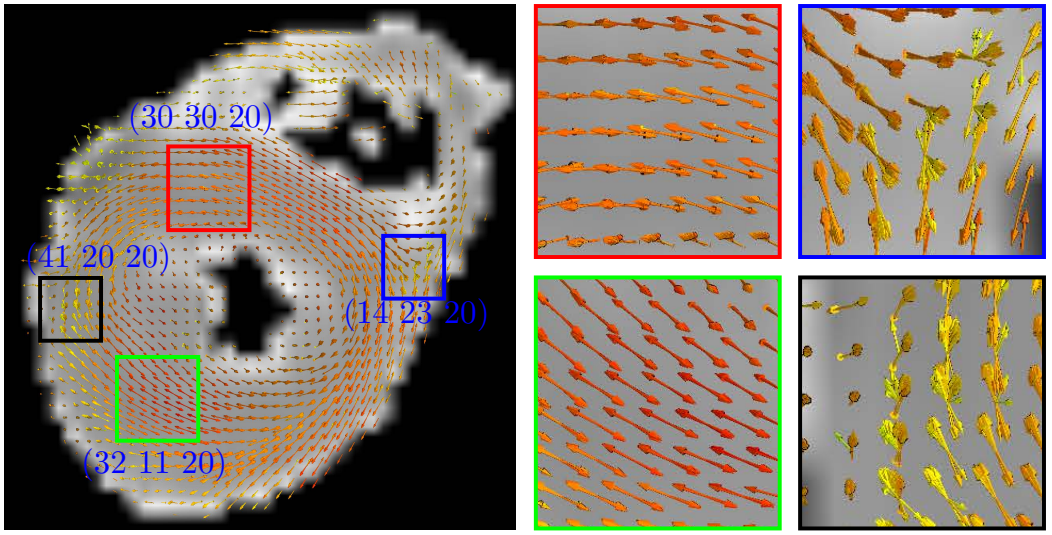

(a) (b)

Figure 4.17: Local tangents of fiber paths produced by the proposed method.

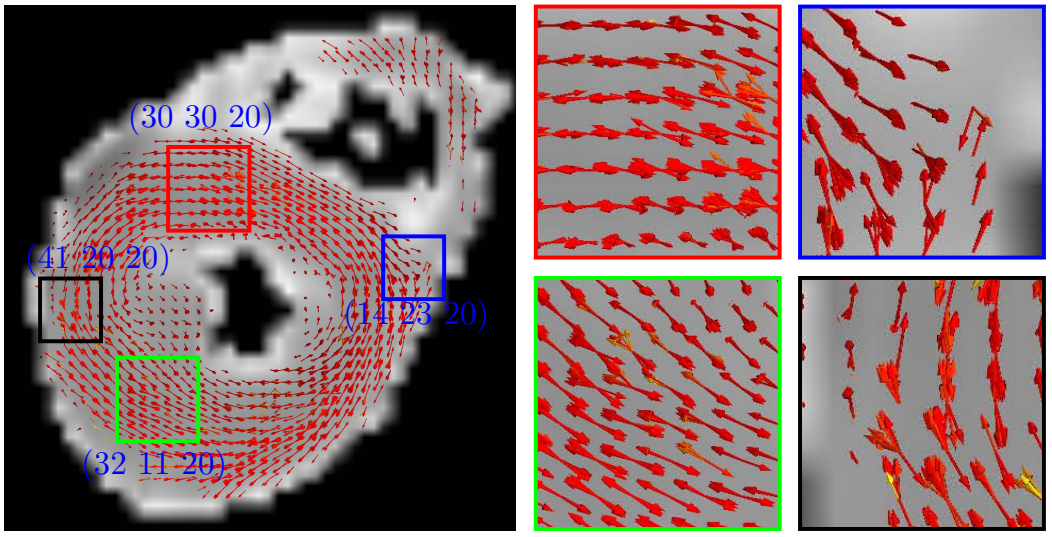

(a) (b)

Figure 4.18: Local tangents of fiber paths produced by streamlining.

LeGrice's sheet model, an illusion of cardiac architecture? – from a visual dissection perspective.

In Fig. 4.19, we show the "strawberry" view of fiber path segments. Fiber paths are cut by the plan $x = 36$ and $x = 37$, and only the fiber path segments between these two plans are left.

In Fig. 4.19-(b) and Fig. 4.19-(c), we observe an "U" and "n" fiber alignment patterns, respectively. But looking ad the fiber path segments in the direction of x axis as shown in Fig. 4.19-(a), we do not observe such pattern. The observed fiber alignment pattern depends on the way in which fiber paths are cut and the viewing angle. Compared to the "strawberry" dissection, the fiber alignment pattern in the sheet model [LeGrice *et al.* (2005)] (see Fig. 2.8 in Chapter refch-anatomy) could probably also behave as "n", but such fiber alignment may be also just an illusion.

4.6 Conclusion

We have proposed a probabilistic fiber tracking method that exploits spatial correlation to better account for data uncertainty in human cardiac DTI data. The method is based on the estimation of a weighted mean likelihood over the spatial neighborhood of the current fiber position. Experimental results on both synthetic and real human cardiac DTI data showed that the proposed method is more robust to noise than the streamlining method and that it produces more regular and smoother fibers, which enables cardiac fiber configurations to be more clearly observed.

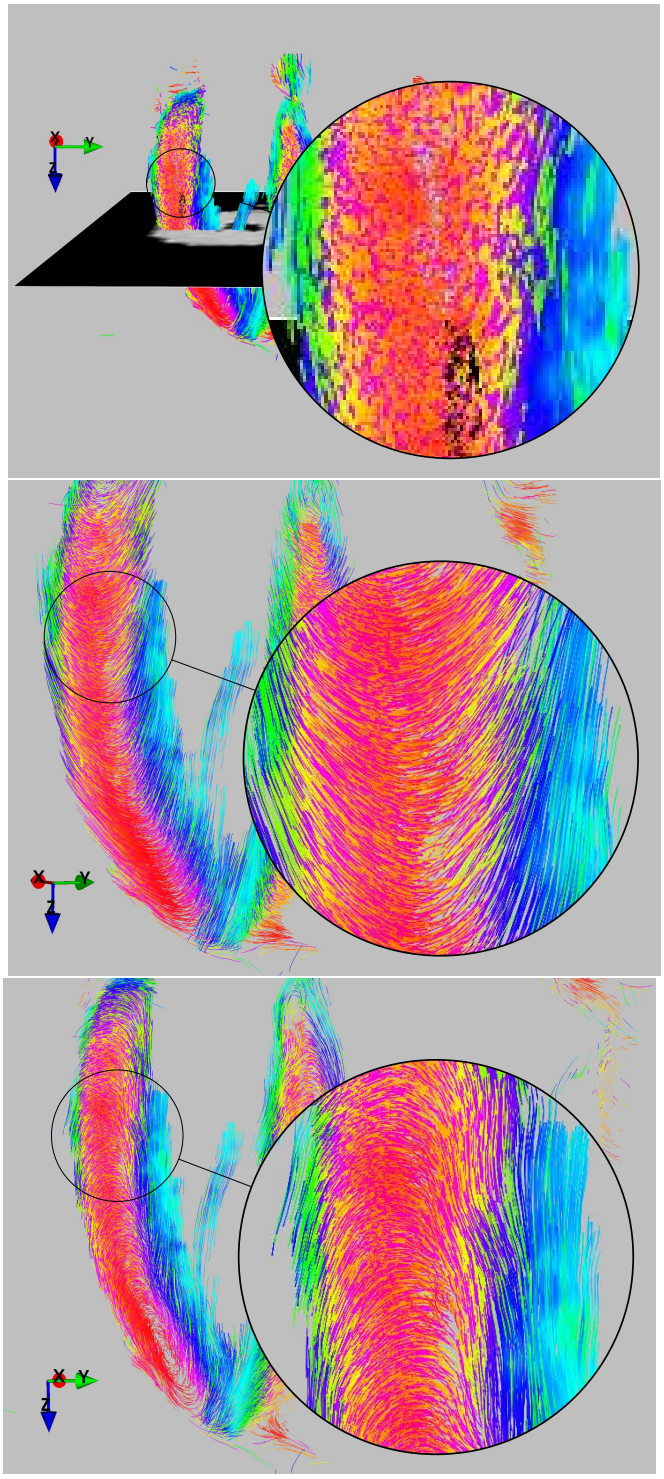

Figure 4.19: “Strawberry” view of the fiber path segments. Fiber paths are cut such that only the segments between $x = 36$ and $x = 37$ are kept. (a) View in the x-axis direction. (b) View in a direction that makes a positive angle between x axis in the $x - y$ plan. (c) View in a direction that has a negative angle between x-axis in the xy plan. The viewing angle is indicated by the small coordinate widget. Notice the position of the red arrow that indicates the x-axis direction.

Chapter 5

Cardiac fiber unfolding by manifold learning

5.1 Résumé

L'architecture de fibres myocardiques est fondamentale pour la compréhension de la fonction cardiaque. L'imagerie de tenseur de diffusion (DTI) permet l'étude non invasive de cette architecture. Dans ce domaine, les techniques de tractographie ont été largement utilisées qualitativement pour représenter et visualiser les informations d'architecture de fibres. Nous proposons un cadre pour décrire l'architecture de fibres cardiaques quantitativement. Le cadre proposé consiste à prendre des faisceaux de fibres en trois dimensions (3D) comme entrées, à déplier les fibres en maximisant la distance au carré totale entre points sous contraintes locales d'isométrie de fibres, et à calculer des paramètres quantitatifs sur les incorporations en deux dimensions à partir des résultats du dépliement. Les résultats ont montré que, après dépliement, il est beaucoup plus facile d'observer et d'appréhender l'architecture des fibres cardiaques et le changement de la forme caractéristique ds fibres 3D, et a révélé qu'il existe des fibres cardiaques présentant des motifs caractéristiques, ce qui offre un moyen intéressant pour étudier quantitativement l'architecture de fibres cardiaques.

5.2 Abstract

Fiber architecture is fundamental in understanding the heart function. Diffusion tensor imaging enables the noninvasive study of myocardial architecture of the heart. Tractography techniques are essential for representing and visualizing the cardiac fiber architecture information encoded in cardiac diffusion weighted images, and have been largely employed qualitatively. In this work we introduce a novel framework of describing quantitatively cardiac fiber architecture using manifold leaning. The proposed unfolding approach takes tractography results, three-dimensional fiber tracts, as inputs and provides a two-dimensional representation of fiber tracts, the embedding, as outputs. The unfolding is performed by maximizing the total squared point distance under local fiber isometry constraints. Our unfolding approach provides a way of quantitatively studying cardiac fiber architecture on the embedding. The results showed that after unfolding it is much easier to observe and apprehend cardiac fiber architecture and the fiber pattern change during fiber propagation. The results also revealed the existence of several cardiac fiber feature patterns.

5.3 Introduction

Fiber architecture is fundamental in understanding the heart function [Taccardi *et al.* (1994), Chung *et al.* (2007)]. Diffusion tensor imaging (DTI) [Basser *et al.* (1994)], which allows for the measurement of water diffusion process in fibrous structure, enables the noninvasive study of myocardial architecture of the human heart [Rohmer *et al.* (2007), Frindel *et al.* (2010), Yang *et al.* (2012), Lombaert *et al.* (2012), Toussaint *et al.* (2013)].

In DTI, the fiber tracts resulting from the tractography process, are usually assessed visually and rendered with a coloring scheme that is sensitive to curve features such as fiber local tangent directions [Zhukov and Barr (2003)]. In the literature of cardiac DTI tractography studies, the helical pattern of cardiac fibers is successfully reconstructed [Kocica *et al.* (2006), Wei *et al.* (2013)]. However cardiac tractography is still commonly considered the final step in representing and visualizing the cardiac fiber architecture.

Until now, there are few works in the literature on the quantitative study of fiber tracts. In cardiac DTI, Frindel et al. proposed a clustering methodology to find cardiac fiber tract correspondences across a fiber tract population obtained from DTI data [Frindel *et al.* (2009)b]. In [Mekkaoui *et al.* (2012)], a significant reorganization of the three-dimensional (3D) fiber continuum was observed in the remote zone of remodeled hearts, indicated by a positive shift in median helix angle along fiber tract segments. In brain DTI, Batchelor et al. [Batchelor *et al.* (2006)] proposed a series of computational techniques that can be used to quantify and compare the shape of fiber tracts. Several clustering approaches were proposed to classify white matter bundles [O'Donnell *et al.* (2006), Zhang *et al.*

(2008)].

In this chapter, we introduce a framework for unfolding cardiac fibers and quantitatively describing their architecture in an easier way. The proposed framework consists in taking 3D fiber tracts as inputs, unfolding the fibers through maximizing the total squared point distance under local fiber isometry constraints, and calculating quantitative parameters on the 2D embeddings resulting from the unfolding.

5.4 Method

Our cardiac fiber unfolding method is based on a non-linear dimensionality reduction technique, semidefinite embedding (SDE) [Weinberger and Saul (2004)]. We start this section by first introducing the principle of dimensionality reduction.

5.4.1 Introduction of dimensionality reduction

Dimensionality reduction is the transformation of high-dimensional data into a meaningful representation of reduced dimensionality. The idea behind dimensionality reduction is that the dimensionality of data set in real applications is usually artificially high, and the data set can be described by just a few parameters. Ideally, after performing dimensionality reduction, the reduced data representation should have a dimensionality that corresponds to the intrinsic dimensionality of the data, which is the minimum number of parameters needed to account for the observed data properties [Van der Maaten *et al.* (2009)]. Dimensionality reduction facilitates data visualization, classification, characterization, etc.

Linear dimensionality reduction

Principal components analysis (PCA) is one of the most popular algorithms for dimensionality reduction. PCA is useful in the case data lies on or close to a linear subspace.

PCA transforms data to a new coordinate system by an orthogonal linear transformation, such that the greatest variance by any projection of the data comes to lie on the first coordinate, the second greatest variance on the second coordinate, and so on [Jolliffe (2005)]. Given n points that lie in $\mathbb{R}^D$, represented by a matrix $X \in \mathbb{R}^{n\times D}$, PCA looks for the d-dimensional linear subspace of $\mathbb{R}^D$ by optimizing the objective function

$$\max_V \operatorname{var}(XV), \tag{5.1}$$

where V is an orthogonal $D \times d$ matrix with its columns representing the d dimensions that we project the original data onto [Cayton (2005)].

Nonlinear dimensionality reduction

Traditional linear techniques are inadequate to handle nonlinear data. For example, intuitively we can observe that the so-called "swiss roll" in Fig. 5.1c is 2D, while linear methods, such as PCA, can not correctly extract this 2D structure, because it lies on a 2D manifold, rather than in a 2D subspace.

Manifold. A manifold is a topological space which is locally Euclidean. Fig. 5.1 shows three manifold examples. A curve is a one-dimensional (1D) manifold, because it can be parameterized by a single variable and locally it can be viewed as a copy of $\mathbb{R}^1$ (see Fig. 5.1a). A sphere is a 2D manifold, because it locally looks like the plane everywhere (see Fig. 5.1b). The so-called "swiss roll" in Fig. 5.1c is a curled plan, and is also a 2D manifold.

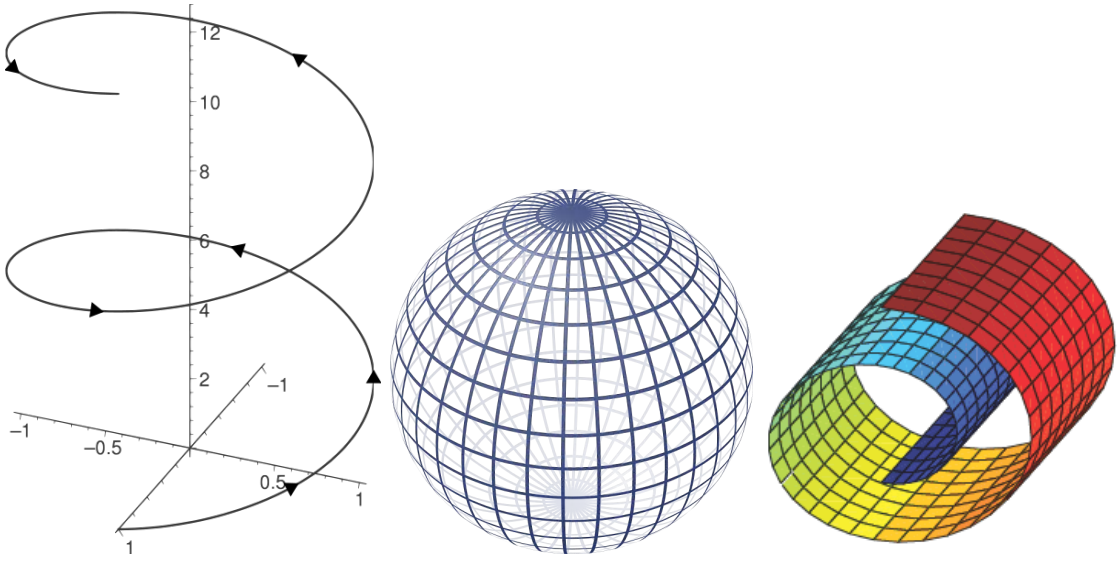

(a) (b) (c)

Figure 5.1: Manifold examples. (a) A curve, a 1D manifold. (b) A sphere, a 2D manifold. (c) A curled plan, the "swiss roll", a 2D manifold. (From wikipedia.org.)

Manifold learning techniques are proposed as nonlinear approaches for dimensionality reduction, and are often viewed as the nonlinear analogs to PCA. The manifold learning problem is about finding the low dimensional embedding of high dimensional data sampled from an underlying manifold [Saul and Roweis (2003)], and is illustrated in Fig. 5.2. A number of manifold learning algorithms are proposed in the last decade: Isomap [Tenenbaum *et al.* (2000)] and LLE [Roweis and Saul (2000)] are the first two algorithms, followed by Laplacian Eigenmaps [Belkin and Niyogi (2001)], and Semidefinite Embedding [Weinberger and Saul (2004)]. (see for an overview, e.g., [Cayton (2005), Van der Maaten *et al.* (2009)]).

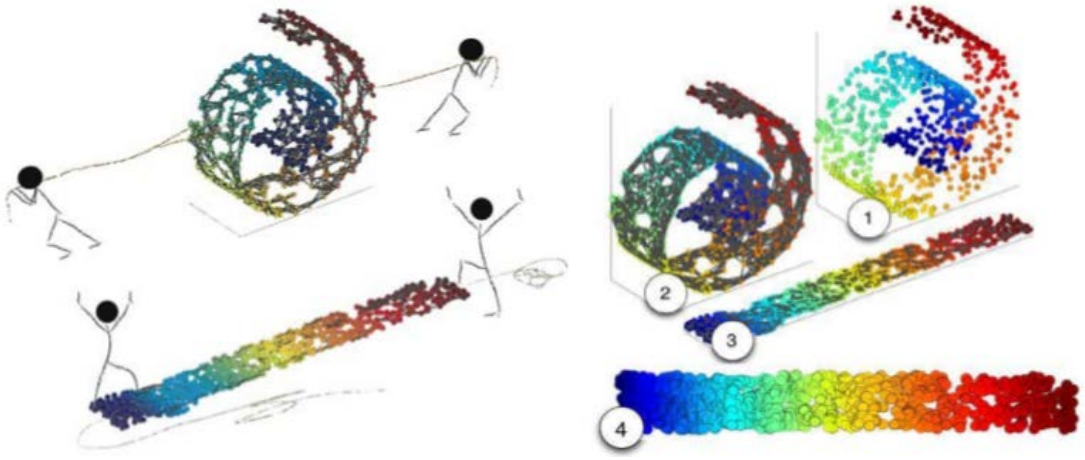

(a) (b)

Figure 5.2: The problem of manifold learning illustrated for data points sampled from a "Swiss roll". (a) The problem is about finding the 2D plan while preserving the local geometry of nearby data points. (b) To reveal the discretized manifold, we first connect a data point with its neighbors, project the data points onto a 2D subspace through an unsupervised learning algorithm while preserving the local geometry of nearby data points. (From [Weinberger and Saul (2004)] [Weinberger and Saul (2006)b].)

Manifold learning examples

Fig. 5.3 shows the manifold concept in human visual perception. An image can be regarded as a collection of numbers with respect to a set of axes, and can also be identified with a point in an abstract high dimensional image space. In Fig. 5.3, a facial image set M is generated by varying the orientation of a face. Because it is generated by smoothly varying one degree of freedom, the angle of rotation, this image set M is a 1D continuous curve in the image space, which has a high dimensionality equal to the number of image pixels. In the general case, when other types of image transformations are also applied in generating the image set, M would have more dimensions, and is said to be a manifold embedded in the image space [Seung and Daniel D. Lee (2000)].

In the image matching problem in Fig. 5.4a, regarding the mean-squared-difference of pixel intensities, the query image and image A are closer. While actually the view in the image A involves an 180 degrees of rotation of the tea pot in the image B. According to the order in which these images are taken shown in Fig. 5.4b, the "distance" between query image and image A is much larger than that between query image and image B.

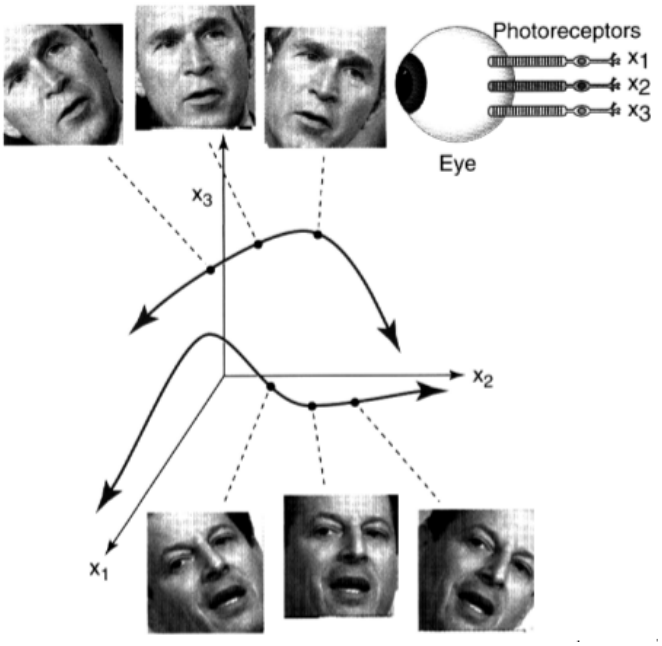

Figure 5.3: In human visual perception, a set of rotated images can be viewed as a continuous curve embedded in the image space. Two sets of images generated by rotating two different faces in the same manner are represented by two curves, i.e., two 1D manifolds. (From [Seung and Daniel D. Lee (2000)].)

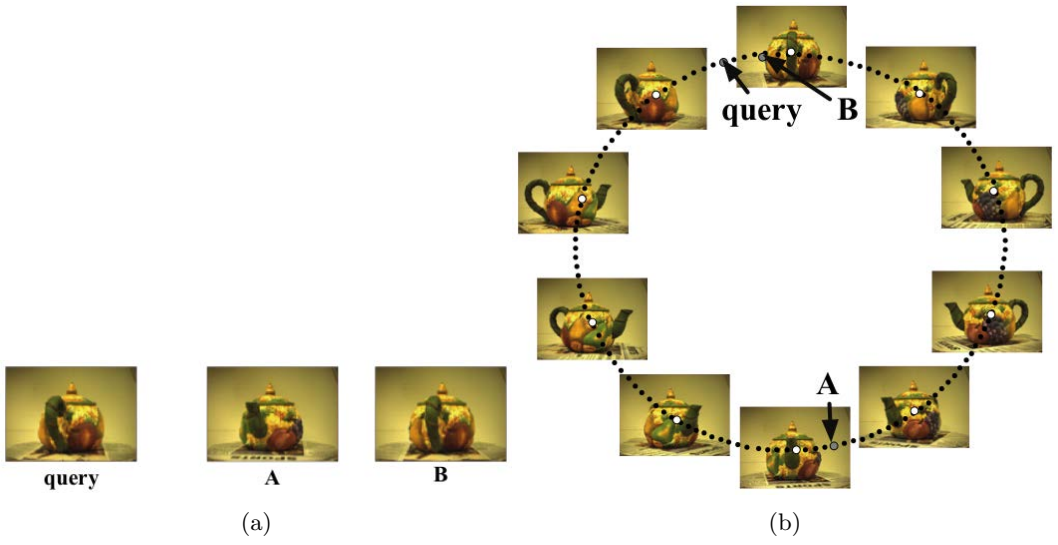

Figure 5.4: A tea pot image matching problem. (a) According to the pixel distance, e.g., the mean-squared-difference of pixel intensities, the query image is near to both image A and image B. (b) According to the order in which these images are taken, image A is "nearer" to the query image. (From [Weinberger and Saul (2006)a].)

5.4.2 Problem description

Cardiac tractography provides a set of 3D fibers or fiber tracts, which represent locally or globally the fiber architecture of the human heart. Fig. 5.5 shows four fibers from tractography process with the 3D B0 volume in the background. In this example, four fibers passing through the same red point are selected. Although there are only a few fibers in this example, the cardiac fiber architecture (here the relative position of fiber segments) is still difficult to describe and apprehend.

In order to deal with this problem, we propose to unfold the 3D fibers on a 2D plane to facilitate their analysis and description through a non-linear dimensionality reduction technique (for an overview, see, e.g., [Cayton (2005), Van der Maaten *et al.* (2009)]) – semidefinite embedding (SDE) [Weinberger and Saul (2004)], which has the nature of positioning data points apart [Sun *et al.* (2006)]. To achieve that, fiber representation is first formulated. Then, fiber unfolding is defined as an implicit process of stretching fiber points by maximizing total squared point distance. To maintain fiber properties, fiber isometry constraint is imposed during unfolding process through constructing a local fiber isometry graph. Final unfolding is achieved by semidefinite programming.

5.4.3 Fiber representation

A fiber can be modeled as a sequence of points (Fig. 5.6). We use the notation $\mathbf{X}^{(p)} = (\mathbf{x}_1^{(p)}, ..., \mathbf{x}_n^{(p)})$ for such a fiber tract, where $p \in \{1, ..., N_f\}$ denotes the fiber number with N_f being the total number of fibers, and $n^{(p)}$ is the number of points that form the p-th fiber. We denote $\mathbf{X} = \bigcup_{p=1}^{N_f} \bigcup_{i=1}^{n^{(p)}} \{\mathbf{x}_i^{(p)}\}$ as the set of all the fiber points, and $N = \sum_{p=1}^{N_f} n^{(p)}$ as the total number of fiber points in $\mathbf{X}$.

By fixing the distance between any two adjacent fiber points $\mathbf{x}_i^{(p)}, \mathbf{x}_{i+1}^{(p)} \in \mathbf{X}^{(p)}$ to be a constant δ (refered to as step length in the following), the arc length between two fiber points $\mathbf{x}_i^{(p)}, \mathbf{x}_j^{(p)} \in \mathbf{X}^{(p)}$ $(i < j,\ i, j \in \{1, ..., n^{(p)}\})$ is approximated by

$$c(\mathbf{x}_i^{(p)}, \mathbf{x}_j^{(p)}) := (j - i)\delta \tag{5.2}$$

($c(\mathbf{x}_i^{(p)}, \mathbf{x}_j^{(p)})$ is the lenth of a polynomial chain approximating the p-th fiber between $\mathbf{x}_i^{(p)}$ and $\mathbf{x}_j^{(p)}$).

We will sometimes drop the superscript indicating the fiber number for simplicity. In this case, a point $\mathbf{x}_i^{(p)}$ is denoted by $\mathbf{x}_m$ with

$$m = \begin{cases} i & \text{if } p = 1, \\ \sum_{k=1}^{p-1} n^{(k)} + i & \text{if } p > 1. \end{cases} \tag{5.3}$$

In other words, $(\mathbf{x}_1, ..., \mathbf{x}_N)$ is the ordering obtained by concatenating the $\mathbf{X}^{(p)}$'s.

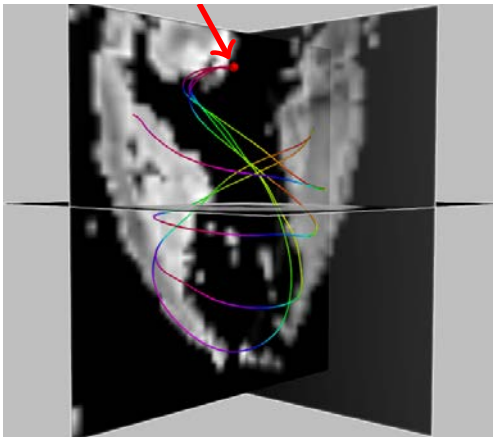

Figure 5.5: Tractography results on human cardiac DT-MRI data with MRI B0 image in the background. Four fibers that locate in the left ventricle are selected by a manually defined point of interest indicated by the red sphere with a diameter equal to voxel size.

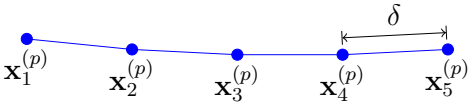

Figure 5.6: A fiber tract $\mathbf{X}^{(p)}$ is represented by a sequence of points. The distance between any two adjacent points is fixed to be a constant δ, and is referred to as "step length".

5.4.4 Fiber isometry

Mathematically, let $(\mathbf{X}, d_{\mathbf{X}})$ and $(\mathbf{Y}, d_{\mathbf{Y}})$ be metric spaces with metrics $d_{\mathbf{X}}$ and $d_{\mathbf{Y}}$. A map $f : \mathbf{X} \to \mathbf{Y}$ is called an isometry or distance preserving if for any $\mathbf{x}_m, \mathbf{x}_n \in \mathbf{X}$ and $\mathbf{y}_m, \mathbf{y}_n \in \mathbf{Y}$ one has

$$d_{\mathbf{Y}}(f(\mathbf{x}_m), f(\mathbf{x}_n)) = d_{\mathbf{X}}(\mathbf{x}_m, \mathbf{x}_n). \tag{5.4}$$

From the definition (5.4), every isometry between metric spaces is a topological embedding. In the above:

- $\mathbf{X}$ is the set of original fiber points, and is the input of fiber unfolding process.
- $\mathbf{Y}$ is the embedding of $\mathbf{X}$ on the 2D Euclidean plan, and is the output of the fiber unfolding process. The elements of $\mathbf{Y}$ are in one-to-one correspondence with those of $\mathbf{X}$.
- f is a "fiber isometry" map, and we have $\mathbf{y}_m = f(\mathbf{x}_m)$.
- $d_{\mathbf{X}}$ is a distance between any two points on the same fiber or two different fibers defined on $\mathbf{X}$, and reflects our knowledge about cardiac fiber organization.
- $d_{\mathbf{Y}}$ is a distance in the embedding $\mathbf{Y}$ (unfolded fibers) between any two points on the same fiber or two different fibers.

5.4.5 Unfolding by stretching fibers

Ideally, we would like to study the fiber architecture directly on $\mathbf{X}$ with a well defined $d_{\mathbf{X}}$. A good $d_{\mathbf{X}}$ should be able to deal well with both local nearby fiber points and far away fibers points that could lie on one single fiber or on different fibers. Fig. 5.7 illustrates that all four points are close to each other regarding to the Euclidean distance. But $\mathbf{x}_k^{(2)}$ is far away from others with regard to the arc length.

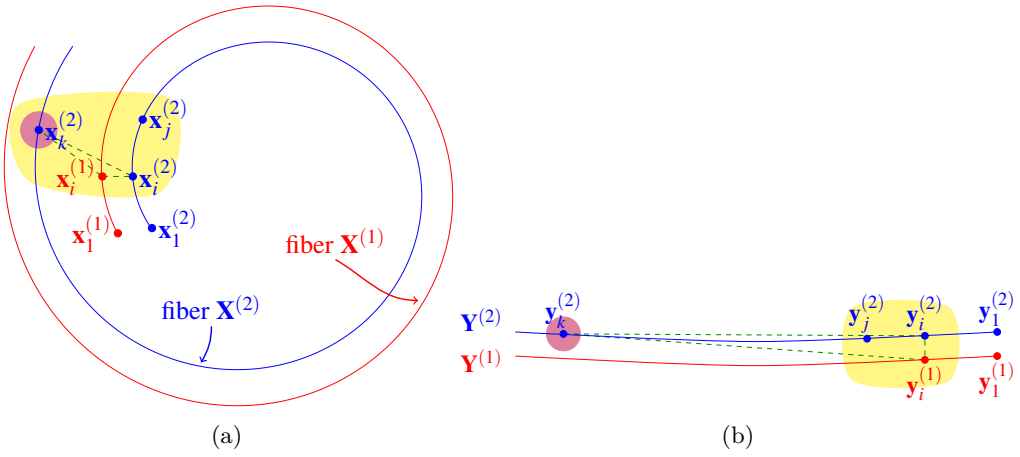

(a) (b)

Figure 5.7: Illustration of two spiral fibers before and after unfolding. (a) All four fiber points $\mathbf{x}_i^{(1)}$, $\mathbf{x}_i^{(2)}$, $\mathbf{x}_j^{(2)}$, and $\mathbf{x}_k^{(2)}$, are close to each other in the sense of the Euclidean distance metric. (b) In the embedding of (a), $\mathbf{y}_k^{(2)} = f(\mathbf{x}_k^{(2)})$ is far away from other three points according to the fiber arc length.

Instead of trying to define $d_{\mathbf{X}}$ precisely and describe the cardiac fiber architecture directly on $\mathbf{X}$, we unfold fibers onto a plan in the Euclidean space to obtain "transformed fibers", namely the embedding $\mathbf{Y}$, and we study the fiber architecture on the embedding. More precisely, without defining the map-f explicitly, our cardiac fiber unfolding process performs it implicitly by stretching fibers, i.e., by maximizing the total pairwise squared distance between the points in the embedding subject to (5.4):

$$\text{Maximize} \sum_{m,n=1}^{N} \|\mathbf{y}_m - \mathbf{y}_n\|^2 \text{ subject to :} \tag{5.5}$$
$$d_{\mathbf{X}}(\mathbf{x}_m, \mathbf{x}_n) = d_{\mathbf{Y}}(\mathbf{y}_m, \mathbf{y}_n) = \|\mathbf{y}_m - \mathbf{y}_n\|,$$

where $\mathbf{x}_m, \mathbf{x}_n \in \mathbf{X}$, $\mathbf{y}_m, \mathbf{y}_n \in \mathbf{Y}$, and $d_{\mathbf{Y}}$ is replaced by the Euclidean distance metric as we unfold fibers to a 2D Euclidean plan.

5.4.6 Preserving local fiber isometry in unfolding

To maintain some fiber properties in the unfolding, e.g., the arc length along fibers and the relative local position of fiber segments, we make $\mathbf{X}$ and $\mathbf{Y}$ "locally isometric". That

is, we make them look like each other locally, and apply the Euclidean metric locally on $\mathbf{X}$. Then the optimization problem becomes

$$\begin{aligned} &\text{Maximize} \sum_{m,n=1}^{N} \|\mathbf{y}_m - \mathbf{y}_n\|^2 \text{ subject to :} \\ &\|\mathbf{x}_m - \mathbf{x}_n\| = \|\mathbf{y}_m - \mathbf{y}_n\|, \text{ for all } (m,n) \text{ such that } e_{mn} = 1, \end{aligned} \tag{5.6}$$

where e_{mn} is an element of the local fiber isometry graph E that is an binary $N \times N$ matrix to be defined. When $e_{mn} = 1$, $\mathbf{x}_m$ and $\mathbf{x}_n$ are close to each other, and zero otherwise. Whether $\mathbf{x}_m$ and $\mathbf{x}_n$ are "close" is measured by the distance $d_{\mathbf{X}}$ defined in the following. The construction of the graph E is detailed after defining the distance $d_{\mathbf{X}}$.

5.4.7 Distance between fiber points

To construct E, we need to first determine $d_{\mathbf{X}}$. The calculation of $d_{\mathbf{X}}$ is not a trivial task since the input fibers present spiral structures in 3D space. To cope with this problem, we introduce the notion of reference points and fiber arc length in the calculation of $d_{\mathbf{X}}$. The idea is to separate a fiber point like $\mathbf{x}_k^{(2)}$ from others to avoid false attachments between them during unfolding (see Fig. 5.7).

More precisely, fibers passing a user defined region of interest (ROI) are selected, and the fiber points in the ROI are treated as reference points. By noting the reference point on a p-th fiber as $\mathbf{x}_1^{(p)}$ with fiber point identifier equal to one, the distance between reference points is given by

$$d_{\mathbf{X}}(\mathbf{x}_1^{(p)}, \mathbf{x}_1^{(q)}) = \|\mathbf{x}_1^{(p)} - \mathbf{x}_1^{(q)}\|. \tag{5.7}$$

For two fiber points $\mathbf{x}_i^{(p)}$ and $\mathbf{x}_j^{(p)}$ that are along the same fiber $\mathbf{X}^{(p)}$, $d_{\mathbf{X}}(\mathbf{x}_i^{(p)}, \mathbf{x}_j^{(p)})$ is set to be the arc length between them

$$d_{\mathbf{X}}(\mathbf{x}_i^{(p)}, \mathbf{x}_j^{(p)}) = c(\mathbf{x}_i^{(p)}, \mathbf{x}_j^{(p)}). \tag{5.8}$$

For the case that $\mathbf{x}_i^{(p)}$ and $\mathbf{x}_j^{(q)}$ $(1 \leq i \leq j,\ p \neq q)$ are on different fibers, we first find the fiber point $\mathbf{x}_i^{(q)}$ then we calculate $d_{\mathbf{X}}(\mathbf{x}_i^{(p)}, \mathbf{x}_j^{(q)})$ approximately using Pythagorean equation (for the example of $d_{\mathbf{X}}(\mathbf{x}_i^{(1)}, \mathbf{x}_k^{(2)})$ see Fig. 5.7),

$$d_{\mathbf{X}}(\mathbf{x}_i^{(p)}, \mathbf{x}_j^{(q)}) = \sqrt{d_{\mathbf{X}}(\mathbf{x}_i^{(p)}, \mathbf{x}_i^{(q)})^2 + d_{\mathbf{X}}(\mathbf{x}_i^{(q)}, \mathbf{x}_j^{(q)})^2}. \tag{5.9}$$

5.4.8 Constructing local fiber isometry graph

After calculating $d_{\mathbf{X}}$ between any two fiber points, we construct the local isometry graph E as follows:

1) For a fiber point $\mathbf{x}_i^{(p)}$, to void dependency on fiber density and fiber step-length, we select the three nearest fiber points along each fibers in terms of $d_{\mathbf{X}}$, and denote this point set as $S_3(\mathbf{x}_i^{(p)})$. That is, $S_3(\mathbf{x}_i^{(p)})$ contains $\mathbf{x}_i^{(p)}$, the two nearest neighbors of $\mathbf{x}_i^{(p)}$ on the p-th fiber, and three nearest neighbors of $\mathbf{x}_i^{(p)}$ on the q-th fiber for all $q \neq p$.

2) Since $\mathbf{x}_j^{(q)} \in S_3(\mathbf{x}_i^{(p)})$ does not necessarily imply that $\mathbf{x}_i^{(p)} \in S_3(\mathbf{x}_j^{(q)})$, we define a symmetric neighborhood system, $\{C(\mathbf{x}_m) : m \in \{1, ..., N\}\}$ by

$$C(\mathbf{x}_m) = S_3(\mathbf{x}_m) \cup \{\mathbf{x}_n \in \mathbf{X} | \mathbf{x}_m \in S_3(\mathbf{x}_n)\} \tag{5.10}$$

3) Among the points in $C(\mathbf{x}_m)$ ($\mathbf{x}_m \in \mathbf{X}$), we select the k-nearest neighbors of $\mathbf{x}_m$ in terms of $d_{\mathbf{X}}$ and denote as $C_k(\mathbf{x}_m)$. This reduction step is intended to deal with fibers of different lengths.

4) we construct the graph E ($N \times N$ binary matrix) as follows:

$$e_{mn} = \begin{cases} 1 & \text{if } \mathbf{x}_m \in C_k(\mathbf{x}_n) \text{ and } \mathbf{x}_n \in C_k(\mathbf{x}_m), \\ 0 & \text{otherwise}. \end{cases} \tag{5.11}$$

Fig. 5.8 illustrates the examples of $S_3(\mathbf{x}_4^{(q)})$, $S_3(\mathbf{x}_6^{(p)})$, $C(\mathbf{x}_4^{(q)})$, $C(\mathbf{x}_6^{(p)})$, $C_k(\mathbf{x}_4^{(q)})$, and $C_k(\mathbf{x}_6^{(p)})$.

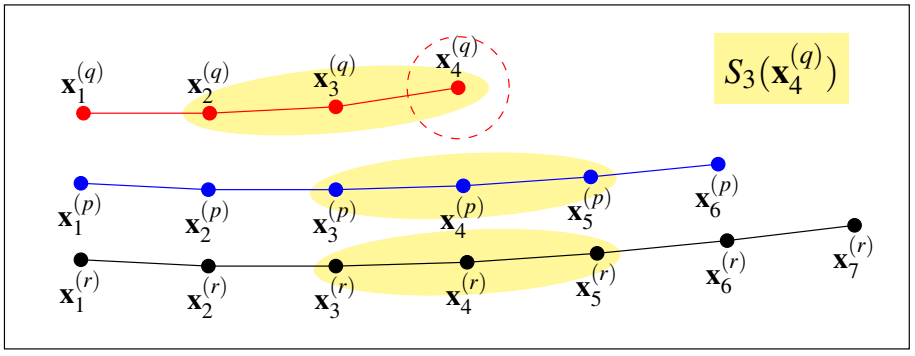

(a)

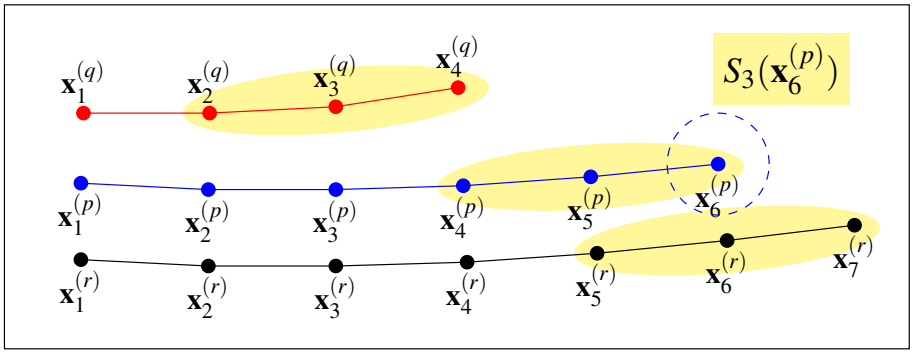

(b)

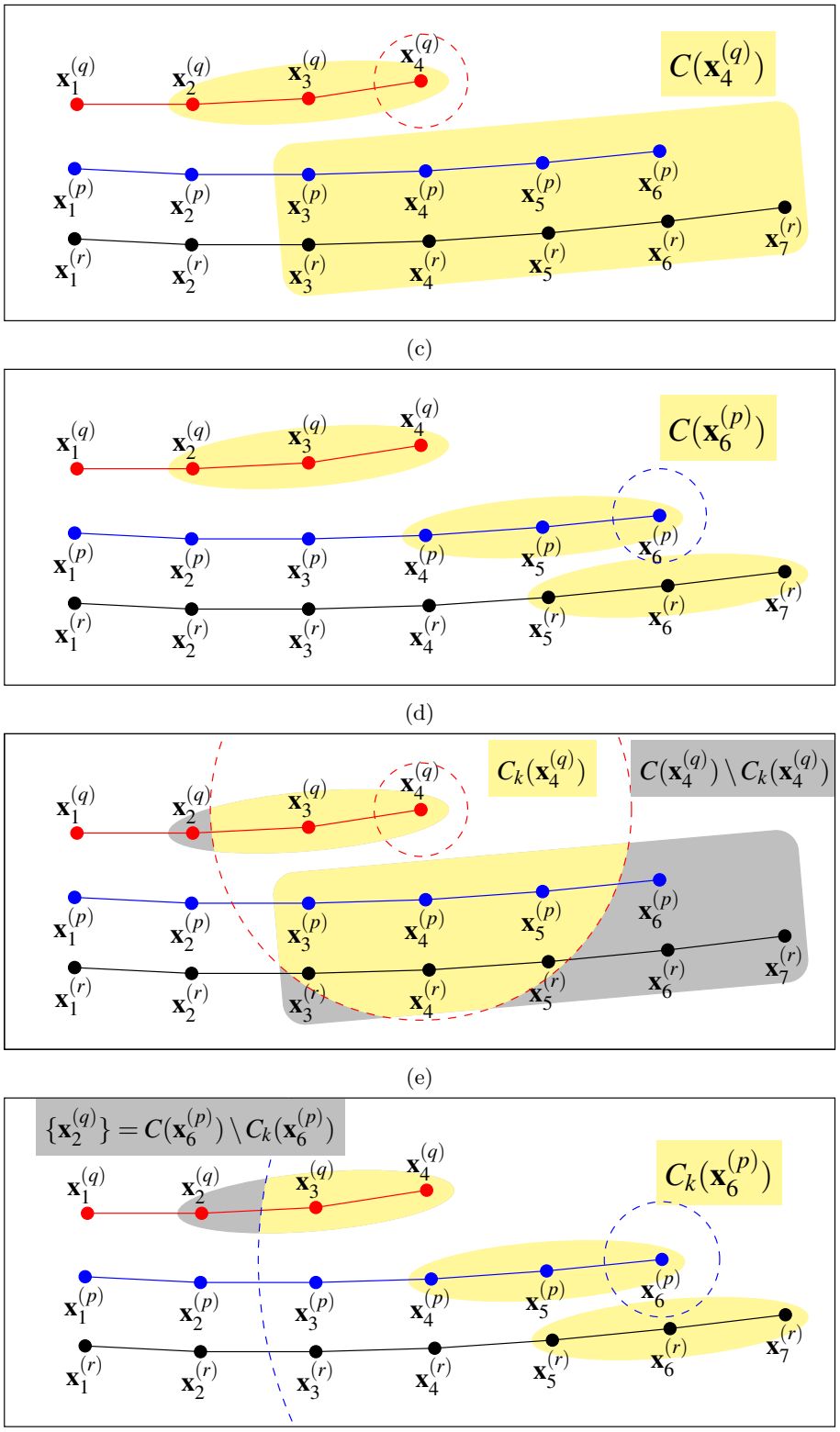

Figure 5.8: Illustration of point sets $S_3(\mathbf{x}_i)$, $C(\mathbf{x}_i)$, and $C_k(\mathbf{x}_i)$. In the illustration, there are three fibers in total with fiber ID p, q, and r. (a) $S_3(\mathbf{x}_4^{(q)})$ is the union of three-fiber-point neighbors of $\mathbf{x}_4^{(q)}$ from $p, q,$ and r-th fibers. (b) $S_3(\mathbf{x}_6^{(p)})$ is the union of the three-fiber-point neighbors from $p, q,$ and r-th fibers. Note that $\mathbf{x}_4^{(q)} \in S_3(\mathbf{x}_6^{(p)})$. (c) Elements of $C(\mathbf{x}_4^{(q)})$

with yellow background. (d) Elements of $C(\mathbf{x}_6^{(p)})$ with yellow background. (e) Elements of $C_k(\mathbf{x}_4^{(q)})$ with yellow background, and elements of $C(\mathbf{x}_4^{(q)}) \setminus C_k(\mathbf{x}_4^{(q)})$ with gray background. (f) Elements of $C_k(\mathbf{x}_6^{(p)})$ with yellow background, and elements of $C(\mathbf{x}_6^{(p)}) \setminus C_k(\mathbf{x}_6^{(p)})$ with gray background. (In this illustration we set $k = 8$ for $C_k(\mathbf{x}_i)$.)

5.4.9 Solving the unfolding problem

After the construction of fiber isometry graph E, the unfolding problem in (5.6) can be solved by semidefinite programming [Vandenberghe and Boyd (1996)] by defining a Gram matrix K with its component equal to the inner product of the elements of $\mathbf{Y}$ [Weinberger and Saul (2004)], that is $k_{mn} = \mathbf{y}_m \cdot \mathbf{y}_n$. Then the objective function in terms of these inner products is

$$\begin{aligned} \sum_{mn} \|\mathbf{y}_m - \mathbf{y}_n\|^2 &= \sum_{mn} (\mathbf{y}_m - \mathbf{y}_n) \cdot (\mathbf{y}_m - \mathbf{y}_n) \\ &= \sum_{mn} \mathbf{y}_m \cdot \mathbf{y}_m + \mathbf{y}_n \cdot \mathbf{y}_n - 2\mathbf{y}_m \cdot \mathbf{y}_n \\ &= \sum_{mn} k_{mm} + k_{nn} - 2k_{mn}. \end{aligned} \tag{5.12}$$

In addition to the fiber isometry constraint represented by E, we also center the output $\mathbf{Y}$ on the origin to remove a translational degree of freedom from the final solution:

$$\sum_m \mathbf{y}_m = \mathbf{0}, \tag{5.13}$$

or in terms of inner products

$$\begin{aligned} 0 &= \left| \sum_m \mathbf{y}_m \right|^2 \\ &= \sum_{mn} \mathbf{y}_m \cdot \mathbf{y}_n \\ &= \sum_{mn} k_{mn}. \end{aligned} \tag{5.14}$$

By putting (5.14) into (5.12), we obtain

$$\begin{aligned} \sum_{mn} \|\mathbf{y}_m - \mathbf{y}_n\|^2 &= \sum_{mn} k_{mm} + k_{nn} \\ &= 2N \sum_m k_{mm} \\ &= 2N \operatorname{Tr}(K). \end{aligned} \tag{5.15}$$

Then the optimization problem is identical to the following semidefinite programming

problem:

$$\begin{aligned} &\text{Maxmmmze trace}(K) \text{ subject to :} \\ &(1) K \succcurlyeq 0. \\ &(2) \sum_{mn} k_{mn} = 0. \\ &(3) k_{mm} - 2k_{mn} + k_{nn} = \|\mathbf{x}_m - \mathbf{x}_n\|^2, \forall (m,n) \text{ with } e_{mn} > 0. \end{aligned} \tag{5.16}$$

From the Gram matrix K learned by semidefinite programming, we can recover the outputs $\mathbf{y}_i$ by matrix diagonaization [Weinberger and Saul (2004)].

Let $v_{\alpha m}$ denote the m^{th} element of the α^{th} eigenvector, with eigenvalue λ_α. Then the Gram matrix element k_{mn} can be written as:

$$k_{mn} = \sum_{\alpha=1}^{N} \lambda_\alpha v_{\alpha m} v_{\alpha n}. \tag{5.17}$$

Then the α^{th} element of the output $\mathbf{y}_m$ is identified as

$$y_{\alpha m} = \sqrt{\lambda_\alpha} v_{\alpha m}. \tag{5.18}$$

5.5 Experiments and results

To evaluate the proposed fiber unfolding approach, both synthetic curves and real cardiac DTI data were used.

5.5.1 Unfolding results on synthetic curves

The synthetic curves concern plan spiral and 3D helixes, which mimic helix fibers in the human heart.

Fig. 5.9 shows a synthetic single spiral. The spiral is represented by 181 points and its length is 84.18. We unfolded the single spiral by setting the parameter $k = 3$, and the reference point was selected as the starting point of the spiral. We set $k = 3$ such that we only preserve the distance between adjacent fiber points. The reference point prevents both ends of the spiral from attaching each other in the embedding. Fig. 5.10 shows the unfolding result on the synthetic spiral in Fig. 5.9. As shown in Fig. 5.10, the embedding of the single spiral is a straight line. The unfolding process succeeded in finding the intrinsic structure. More quantitatively, the first normalized eigenvalue is about one and is much bigger than other eigenvalues. This indicates that the data variation of the embedding concentrates in the first dimension, and reveals that the intrinsic dimensionality of the

spiral is one. Between original spiral and its embedding, the length difference is about 0.01% of total length of the original spiral.

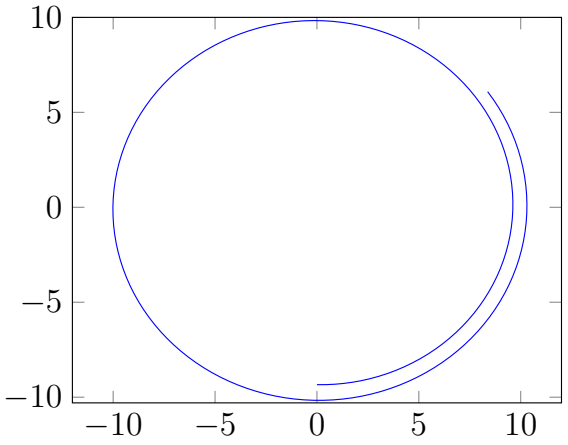

Figure 5.9: A spiral of length 84.18, represented by 181 points.

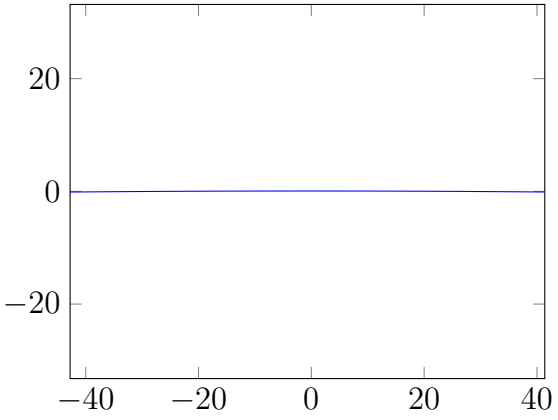

Figure 5.10: Unfolding result on the synthetic spiral in Fig. 5.9.

For 3D helixes with the same helix angle in Fig. 5.11, the unfolding results are shown in Fig. 5.12. The parameter k was set to 10, and the reference points (indicated by the red points in Fig. 5.11) were chosen manually. The embedding successfully reveals the intrinsic structure of the original helixes. The distance between the nearby lines in the embedding is almost the same as the distance between nearby helixes. The length of the lines in the embedding shrunk 0.49% on average. The two dominant normalized eigenvalues of Gram matrix are respectively 0.9949 and 0.0047, indicating that the variation of the point positions is two-dimensional. That is, the helix points are lying on a 2D manifold.

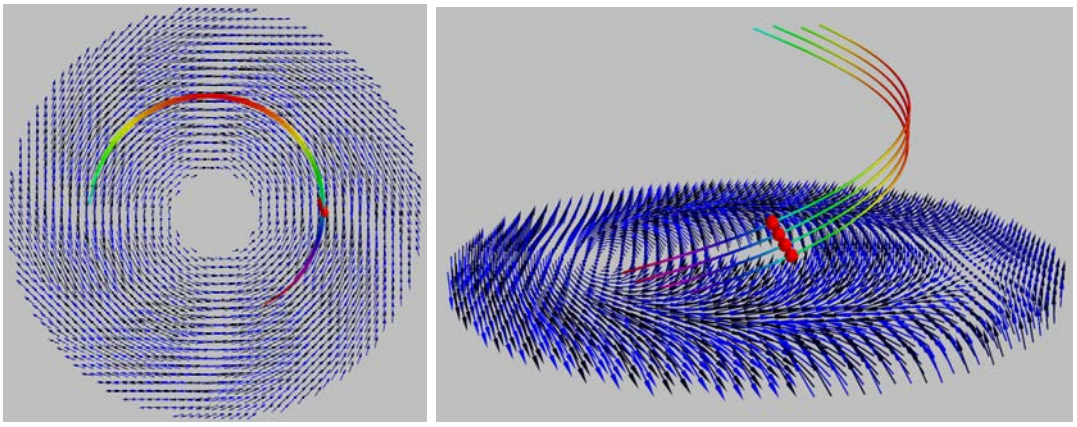

(a) (b)

Figure 5.11: Four synthetic 3D helixes of the same helix angle shown in different viewing angles. The lengths of the helixes are respectively 48.9976, 48.9976, 49.4976, and 49.4976. The distance between the helixes is approximately indicated by the distance between red points. For two nearby helixes, the distance is about 0.9322.

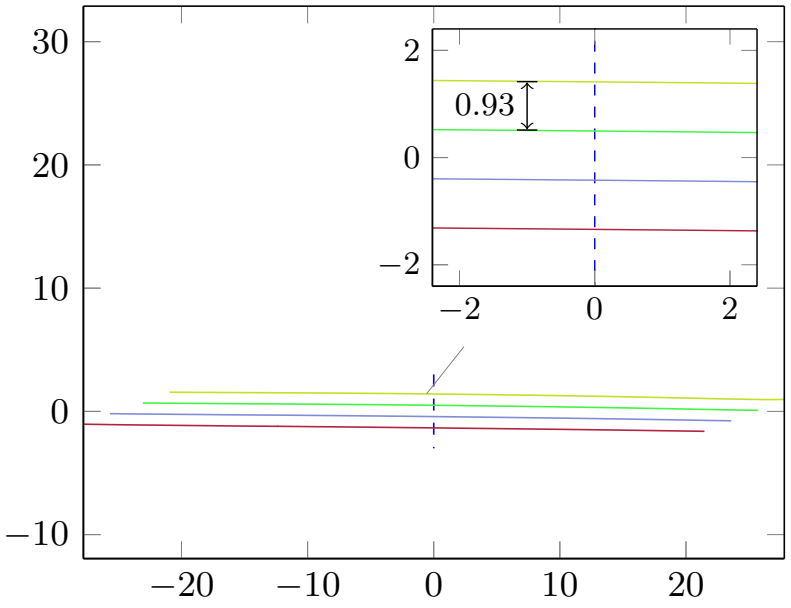

Figure 5.12: The embedding, four lines with lengths 48.7521, 48.7668, 49.2577, and 49.2469, obtained by unfolding the synthetic 3D helixes in Fig. 5.11.

5.5.2 Unfolding results on cardiac fibers

The real data consists of ex-vivo human cardiac data acquired with a Siemens 1.5 T Magnetom Avanto with the following settings: TE = 98 ms, TR = 8600 ms, FOV = 256×256 mm^2, slice thickness = 2 mm, number of slices = 52, slice size = 128×128, diffusion sensitivity $b = 1000$ s$\cdot$mm^{-2}, gradient directions = 12. The sequence used a 2D EPI diffusion-weighted sequence with a twice-refocused diffusion preparation.

The used fibers were generated by a probabilistic tractography method [Li *et al.* (2012)]. The seeds were initialized at all the voxels in the diffusion weighted image volume. From one seed, two fibers propagating in symmetrical directions were generated. The total number of fibers was about twenty thousand.

Each fiber provided by the tractography method consists of about 160 points on average with step length equal to half voxel size. To reduce the large memory requirement in the unfolding process, in some experiments, fibers were resampled with larger step length.

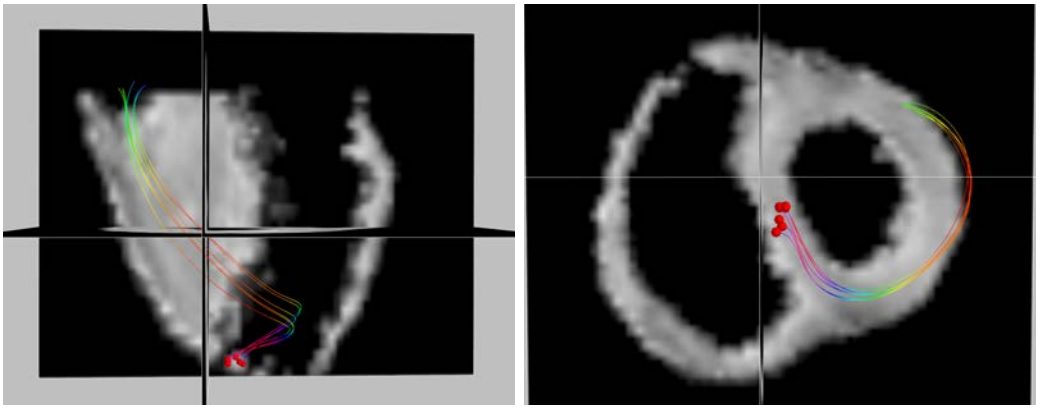

(a) (b)

Figure 5.13: Six fibers with simple architecture configuration shown in long axis view and short axis view. The red points are the seeds, i.e., the starting points of fibers.

Table 5.1: Top four normalized eigenvalues of the Gram matrix K obtained from unfolding the fibers in Fig. 5.14 with reference points at different locations along fibers.

n-th normalized eigenvalue	1	2	3	4
reference points: at the start	0.9907	0.0064	0.0008	0.0005
reference points: in the middle	0.9896	0.0073	0.0010	0.0005
reference points: at the end	0.9906	0.0070	0.0007	0.0005

Fig. 5.13 shows fibers having simple configurations. The reference points were set at the starting, in the middle and at the end of fibers to study the effect of different reference point positions. In all these three experiments, we set $k = 15$. In Fig. 5.14, we observe that the embedding curves vary in 2D plan. The three embeddings do not show any apparent difference. The normalized eigenvalues indicate that the dominant data variation occurs in the first dimension, and the variations in the third dimension and beyond are negligible (see Table 5.1). Visually the distances between nearby reference points in Fig. 5.14d are a little larger than the ones in Fig. 5.14b and Fig. 5.14f. As a result, the data variation of the embedding in the second dominant dimension is slightly bigger than the other two, which is indicated by the second largest normalized eigenvalues in Table 5.1.

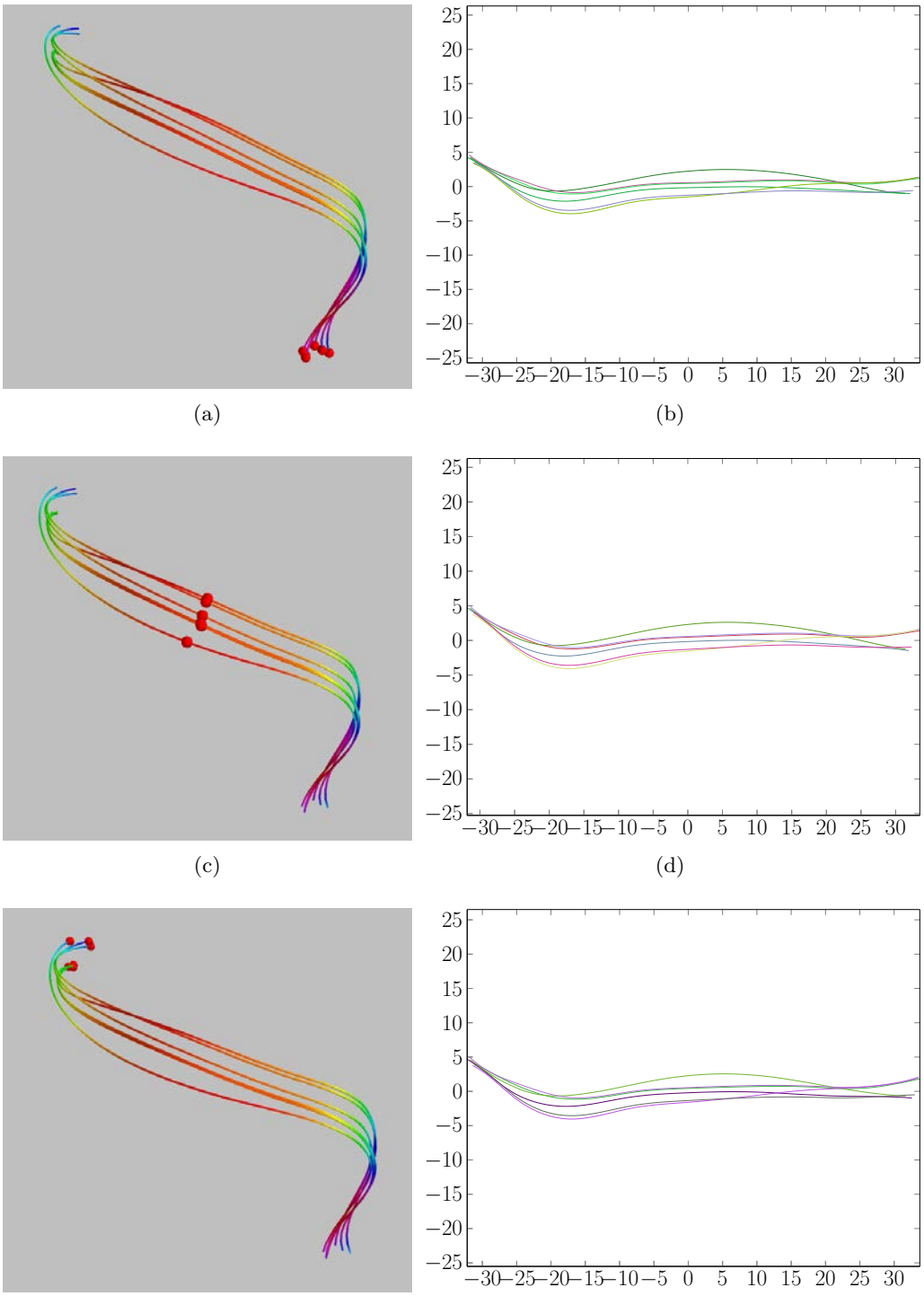

Figure 5.14: Fibers and corresponding embeddings obtained with reference points set at different locations. The three fibers in (a) (c) and (e) are the same, but reference points (the small red points set) respectively at the start, in the middle, and at the end of the fibers. The lines in (b), (d), and (f) are the corresponding embeddings in random colors.

To compare the embeddings quantitatively, we calculate the value of $d_{\mathbf{Y}}$ between every pair of points in the embedding for each experiment. For any two points, among all three experiments, the difference of $d_{\mathbf{Y}}$ is below one, and the absolute difference on average are 0.1018, 0.0741, and 0.1634 between one another experiments. The small difference of $d_{\mathbf{Y}}$ indicates that the architecture of the three embeddings are similar. On the other hand, these results also show that the choice of reference point locations does not affect much the unfolding results.

The unfolding results on somewhat more complicated fiber structures Fig. 5.15 are shown in Fig. 5.16, with the following corresponding normalized eigenvalues of the Gram matrix: 0.9926, 0.0026, 0.0012, 0.0007, and 0.0004. Though the original fiber architecture configuration of Fig. 5.15 seems complicated, the embeddings in Fig. 5.16 visually show simple fiber architecture on a 2D plan.

An even more complicated fiber structure is shown in Fig. 5.17 where are shown different views of ten fibers that pass a small ROI. The fiber points falling in the ROI are denoted by the red points. Before unfolding, fibers are resampled with a step length equal to one voxel size. From Fig. 5.17, it is hard to describe the fiber architecture, and we can only observe that all these fibers exhibit, around the red points, short segments which propagate in parallel. The apex view in Fig. 5.17d shows that there seems to exist spiral fibers, while the change of fiber patterns in the curling plan is hard to observe directly. Fig. 5.18 shows the unfolding results (with $k = 15$), and the top five normalized eigenvalues of the Gram matrix are respectively 0.9639, 0.0251, 0.0043, 0.0018, and 0.0010. The first two normalized eigenvalues account up to 98.90, implying that data variation occurs mainly in the first two dimensions. From the embedding in Fig. 5.18 we can clearly observe the change of fiber patterns during the propagation of fibers. To look into the details, we select four fibers from these ten fibers, and cut off the well-aligned part (see Fig. 5.5 for a 3D view). The unfolding results on these short fiber segments are shown in Fig. 5.19 and the top five normalized eigenvalues of the Gram matrix are respectively 0.9546, 0.0379, 0.0023, 0.0018, and 0.0008 (obtained with $k = 15$). After unfolding, fiber patterns are observed much easily compared to the original fibers in 3D views. We can remark that the fibers passing the ROI go parallel first, then expand on the heart wall, and finally tend to end in the same area. The propagation of fibers occurs mainly in the first two dimensions, as indicated by the sum of the first two normalized eigenvalues, which amount to 0.9925.

Effect of parameter k

In this experiment, we study the effect of parameter k on unfolding fibers.

In Fig. 5.21a, eighteen fibers are selected by a range of points (colored in purple), and they are manually separated into two groups according to their shape and the pattern

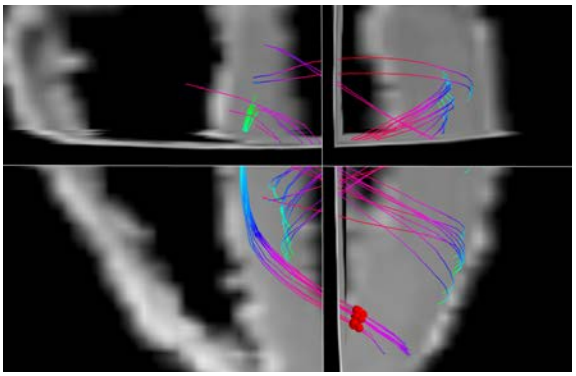

(a)

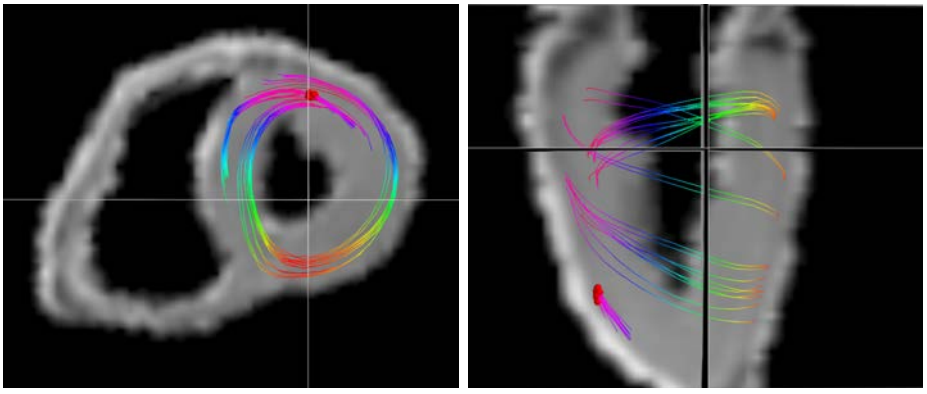

(b) (c)

Figure 5.15: Three views of fibers.

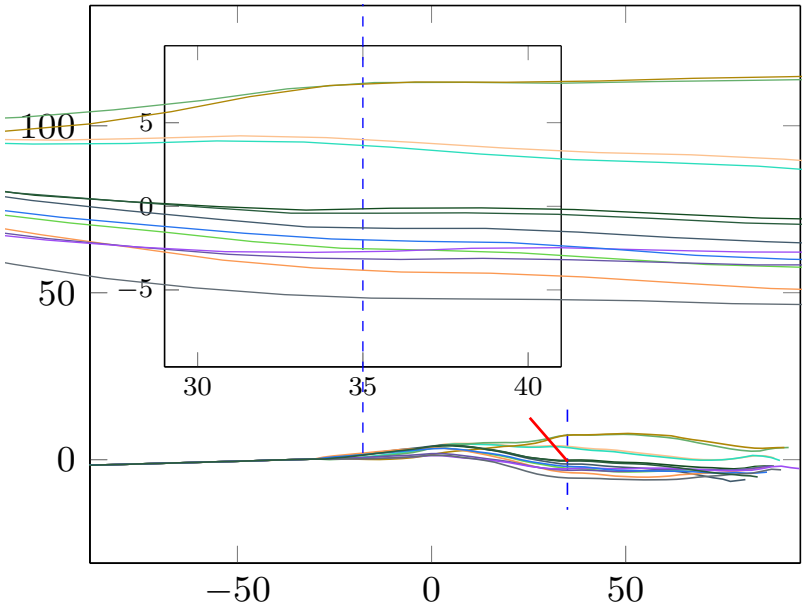

Figure 5.16: Unfolding results on Fig. 5.15.

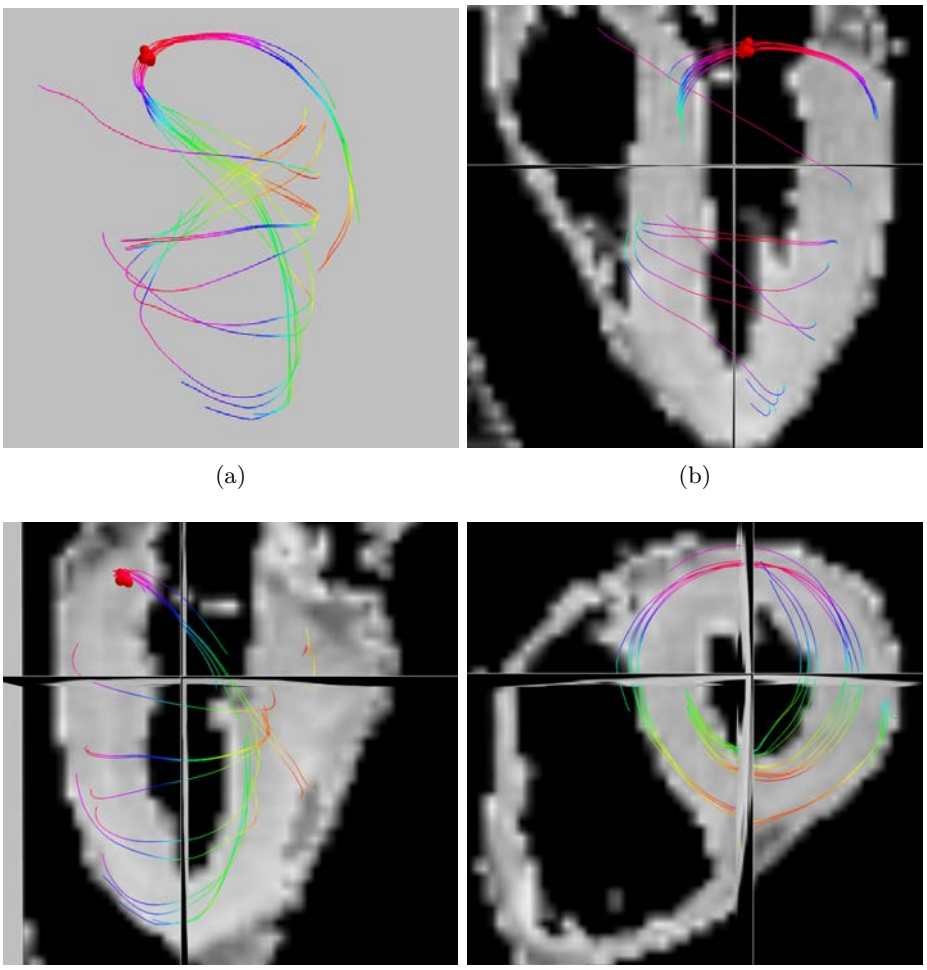

(a) (b)

(c) (d)

Figure 5.17: Different views of ten fibers selected by a small ROI. The fiber points falling in the ROI are denoted by the red points.

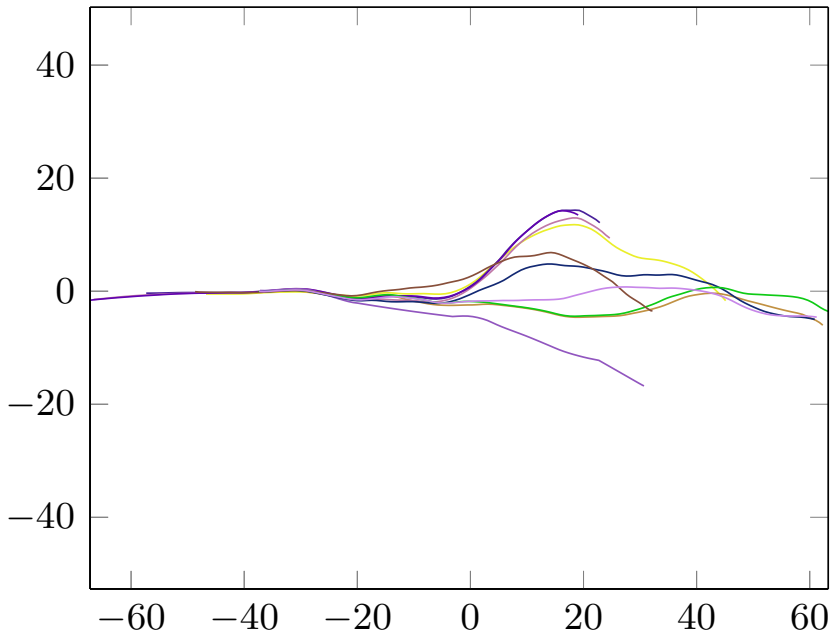

Figure 5.18: Unfolding results on Fig. 5.17.

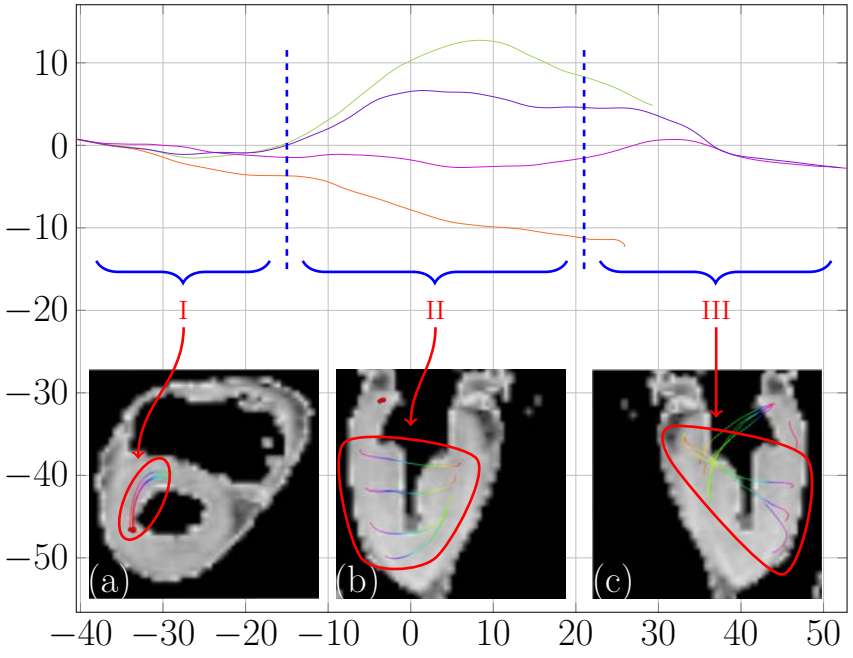

Figure 5.19: Unfolding result of the short cut fibers in Fig. 5.5. The unfolded curves are roughly divided into three parts by the vertical dashed lines: (I) fibers go parallel ; (II) fibers expand in the heart wall; (III) three fibers tend to end in the same direction. The associated original fiber segments are shown in different views in (a), (b), and (c).

(see Fig. 5.21b and Fig. 5.21c). Reference points (in red) are selected near a vertical plan (in red, see Fig. 5.22b). Fibers are resampled with step length equal to 2 times voxel size.

Fig. 5.22 shows the unfolding results obtained with different vaules of k. Embeddings can be divided into two groups by their appearance. We can observe that the embeddings in Fig. 5.22a, Fig. 5.22b and Fig. 5.22c are similar, and appear a trisector-like point in the middle. The embeddings in Fig. 5.22d, Fig. 5.22e and Fig. 5.22f also look like one another, and show up a ring. In both embedding groups, the bigger k is, the larger local isometry is assumed, and the more fiber configuration details in a larger area is preserved in the embedding. Comparing the two groups, the appearance of the embeddings obtained with $k = 20$ and $k = 25$ change greatly. Eigenvalue spectrum in Fig. 5.20 also shows a shift in the first eigenvalues from $k = 20$ and $k = 25$. Thus by changing the parameter k and observing the leading normalized eigenvalues we can get insight into the group behavior of fibers.

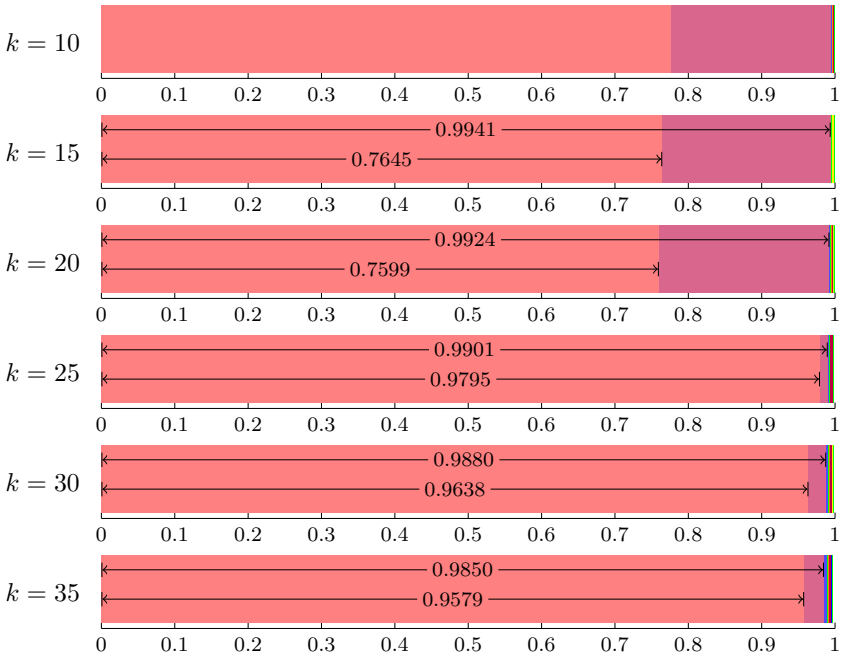

Figure 5.20: Eigenvalues spectrum of the Gram matrix K for the unfolding results with different parameter k. The first two accumulated normalized eigenvalues are denoted on the spectrum.

5.6 Discussion

As a first step towards quantitative description of fiber architecture, it is necessary to well define the distance between fiber points both on the same fiber and across fibers, which can be a problem for helix fibers that largely exist in heart. Rather than finding a proper

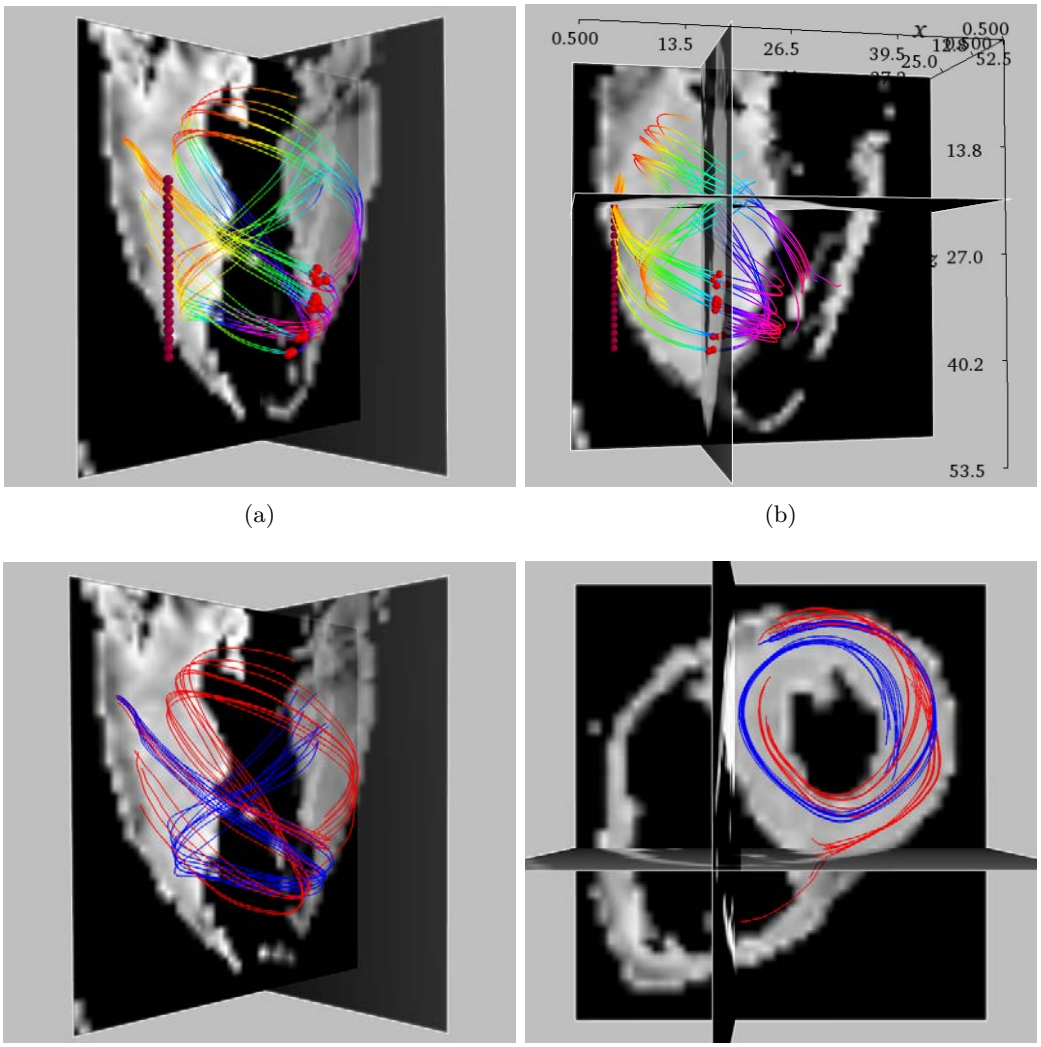

(a) (b)

(c) (d)

Figure 5.21: Eighteen fibers selected for studying the behavior of unfolding process on different parameter k on fibers with complicated configuration. (a) Fibers are selected by the vertically aligned purple points, with red points denoting the reference points. (b) Reference points are selected near a user defined vertical plan. (c) (d) Fibers are divided into two nine-fiber groups manually, and are colored in red and blue.

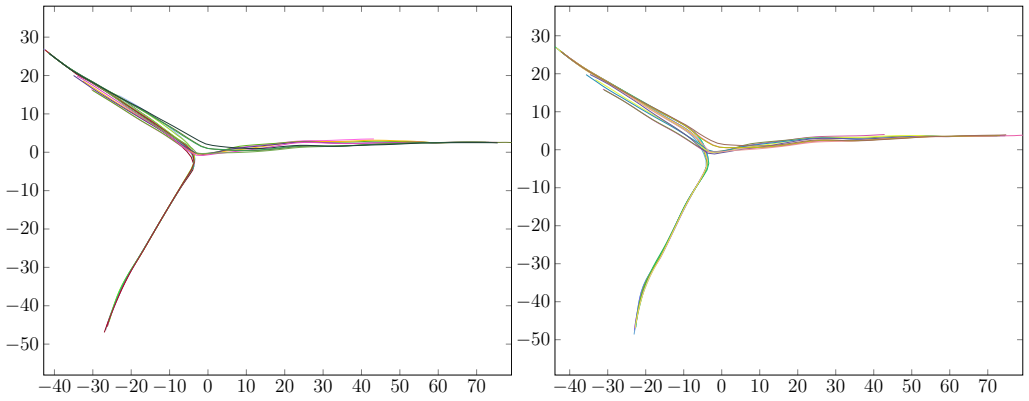

(a) $k = 10$ (b) $k = 15$

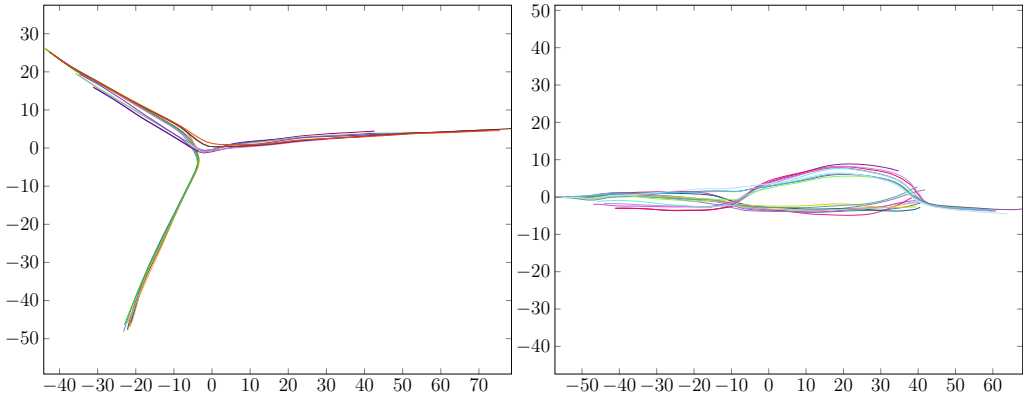

(c) $k = 20$ (d) $k = 25$

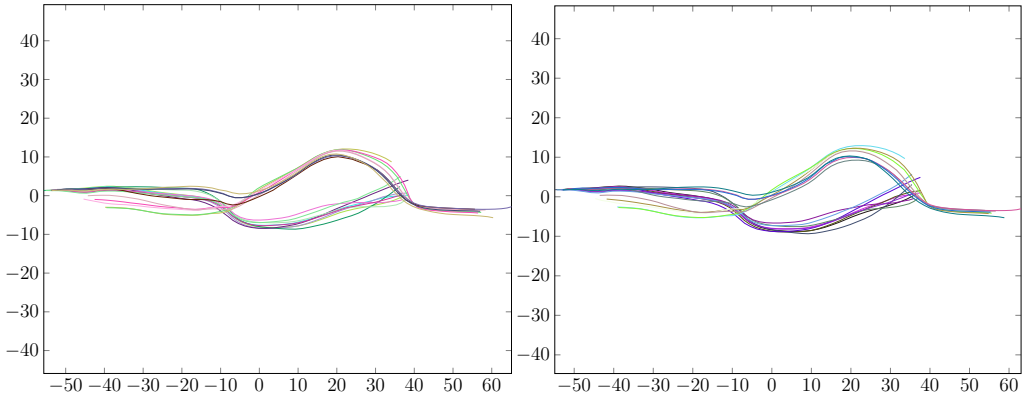

(e) $k = 30$ (f) $k = 35$

Figure 5.22: Embedding of fibers in Fig. 5.21 obtained with parameter $k = 10$, 15, 20, 25, 30, and 35.

metric $d_{\mathbf{X}}$ on original fiber points $\mathbf{X}$, we map fibers onto a plan by fiber unfolding, and then we study the fiber architecture of $\mathbf{X}$ on $\mathbf{Y}$ with $d_{\mathbf{Y}}$. The unfolding map is not defined explicitly and are performed implicitly by maximizing the total squared distance between outputs. We preserve fiber geometry locally in the embedding by adding local isometry graph constraint E. We allow fibers to change shape globally during the unfolding.

In unfolding, we assume that fibers lie on or near a manifold. Experiments on synthetic spiral (Fig. 5.9) and synthetic helix fibers (Fig. 5.11) demonstrate the ability of our unfolding approach to reveal the intrinsic structure of these synthetic fibers of simple structure.

In the present fiber unfolding, we selected fibers in a small ROI and took only about one thousand and two hundred points as inputs (which corresponds to about twenty fibers at most) due to the memory limitation in formulating the unfolding problem into a semidefinite programming problem. Of course, using a small ROI ensures us that the selected fibers lie on or near a manifold. The fiber points that fall in the ROI are usually treated as reference points, but users can chose other fiber points as reference points as well. It would be also interesting to unfold fibers selected in a large ROI, e.g., selecting fibers across the heart wall, though it may be hard to ensure that the fibers lie on a plan manifold in this condition.

The calculation of $d_{\mathbf{X}}$ is subject to errors. With different reference point locations, the amount of errors will be different. Nevertheless, since $d_{\mathbf{X}}$ is only used in constructing local fiber isometry graph E, and the distance preserved in unfolding process is the original local fiber distance, the errors on the final embeddings would be negligible.

The parameter k controls how large the local isometry is. With a bigger k (so assuming a larger local isometry), we can study the global configuration of fiber groups. Note that we selected k-nearest neighbors in a subset of $\mathbf{X}$ rather than in the whole set of $\mathbf{X}$. The subset was constructed by first selecting nearest three points along each fiber. Then along the fiber $\mathbf{X}^{(p)}$, for a fiber point $\mathbf{x}_i^{(p)}$, these three points are $\mathbf{x}_i^{(p)}$ and the two adjacent points $\mathbf{x}_{i-1}^{(p)}$ and $\mathbf{x}_{i+1}^{(p)}$. By keeping the distance between adjacent points along a fiber $\mathbf{X}^{(p)}$, we keep the corresponding curve $\mathbf{Y}^{(p)}$ in the embedding having the same length as the original fiber $\mathbf{X}^{(p)}$. In constructing the subset for $\mathbf{x}_i^{(p)}$, we could probably select less points along fibers $\mathbf{X}^{(q)}$ ($q \neq p$, $p, q \in \{1, ..., N\}$), e.g., two or even only one. Then we potentially just need a smaller k in constructing local fiber isometry graph E. With a smaller k there will be less constraints and consequently less memory consuming in solving the unfolding problem.

We notice radish shape-like fiber propagation patterns in the endocardium. The fibers selected in a small ROI like the ones in the endocardium (Fig. 5.17 and Fig. 5.5) propagate and expand in the heart wall, and finally trend to end in a similar area. The fibers selected in the epicardium do not involve much expansion during the propagation in the heart wall. More experiments would be needed to confirm whether such fiber propagation patterns

are common to all the human hearts.

5.7 Conclusion

We have proposed a framework for unfolding cardiac fibers; the unfolding has been achieved by maximizing the total squared point distance under local fiber isometry constraints. With this framework, it is possible to achieve quantitative description of complicated 3D fiber architecture of the human heart. The results showed that the proposed fiber unfolding allow the cardiac fiber patterns to be observed, which suggests a new way to further study and better understand the cardiac fiber architecture of the human heart, and opens interesting perspectives for clinical applications such as comparative study of various possible human hearts.

In the future work, it would be also interesting to first automatically classify fibers that potentially lie on the same manifold into different clusters, and then study fiber architecture by unfolding fibers in a cluster-wise manner.

Chapter 6

Towards a simplified cardiac fiber architecture - multiscale fiber merging

6.1 Résumé

La tractographie cardiaque consiste à générer un grand nombre de fibres pour représenter et visualiser l'architecture cardiaque. Pour que les fibres couvrent tout le myocarde, les points des graines sont initialisés de manière large, par exemple, à chaque voxel de l'ensemble de données, pour éviter de rater des fibres potentielles. Cependant, avec ce genre de stratégie, le processus de tractographie produit trop de fibres. Il y aura des doublons lorsque les graines sont initialisées sur la même fibre. Physiquement, un grand nombre de fibres sont difficiles à faire des rendus et à visualiser. Il est également difficile d'observer la structure des fibres cardiaques à partir de fibres denses. Des fibres doublons peuvent constituer une lourde charge pour les analyses quantitatives. Une représentation simplifiée de la structure de fibres cardiaques est alors nécessaire afin de visualiser et d'analyser de manière efficace l'architecture de fibres du cœur.

Dans ce chapitre, nous proposons une approche, fusion de fibres, pour générer une architecture simplifiée de fibres cardiaques. La fusion de la fibre est obtenue en faisant la moyenne des fibres, selon une grille. Les résultats montrent que l'architecture simplifiée de fibres permet l'observation de la configuration des fibres cardiaques d'une manière plus facile.

6.2 Abstract

Cardiac tractography usually involves in generating a large number of fibers for representing and visualizing the cardiac fiber architecture. In order to make fibers cover all the myocardium, seeds are initialized largely, e.g., at every voxel in the data set, to avoid missing potential fibers. However with such kind of seeding strategy, the tractography process produces too many fibers. And there will be duplicated ones when seeds are initialized along the same fiber. Physically, a large number of dense fibers are hard to render and visualize. It is also hard to observe cardiac fiber structure from dense fibers. Potential duplicated fibers can be a burden for further quantitative analysis. A sparse/simplified cardiac fiber structure representation that highlights the main heart architecture is needed for effective visualization and quantitative analysis.

In this chapter, we propose a fiber oriented approach, fiber merging, to provid simplified cardiac fiber architecture. Merging fiber is achieved by averaging fibers according to a cell grid. The produced simplified fiber architecture can highlight the cardiac fiber configuration.

6.3 Introduction

Cardiac tractography in diffusion tensor imaging (DTI) usually involves in generating a large number of fibers for representing and visualizing the cardiac fiber architecture. In order to cover the entire myocardium, we need to generate potential fibers throughout the heart. That is, we need to initialize seeds largely in the myocardium, often at every voxel to avoid missing potential fibers, instead of initializing seeds in random manner [Cheng *et al.* (2012)]. But with this seeding strategy, it may produce too many fibers. For example, for an adult human heart DTI data set with a size of $2 \times 2 \times 2$ mm^3, by initializing seeds at every voxel in the tractography process, we would generate about twenty thousand fibers. And there will be duplicated ones when seeds are initialized along the same fiber.

This seeding problem arises in most tractography algorithms developed based on line propagation techniques, e.g., streamlining [Basser *et al.* (2000)] and tensor line [Lazar *et al.* (2003)]. There are few tractography algorithms that do not need to initialize seeds. The graph based tractography algorithm proposed in [Frindel *et al.* (2010)] initializes the tracking process with a graph covering the whole data set instead of explicitly initializing seeds. Though it may avoid generating duplicated fibers, it is not practical in terms of time and memory consuming aspects. For most tractography algorithms, we cannot avoid this seeding problem.

We can express the goal of tractography process as generating potential fibers that represent the whole structure of the object in study. We also would like the number of

fibers to be as small as possible in order to facilitate further qualitative and quantitative analysis.

Large number of dense fibers with potential duplicated ones cause several problems. Visually it is hard to observe cardiac fiber structure from dense fibers, e.g., fibers in the epicardium may hinder the visualization of the fibers in endocardium. Physically rendering duplicated fibers consumes additional memory and can make it harder to visualize them. Duplicated fibers can be a burden for further quantitative analysis.

A simplified cardiac fiber structure representation is needed for effective visualization and quantitative analysis. There exist one approach in the literature that provides simplified cardiac fiber architecture [Poveda *et al.* (2011)] [Poveda *et al.* (2012)]. The simplification is performed on DW data, which involves in down sampling the data set to lower resolution. Fibers are generated by streamlining tractography algorithm on this low resolution data set, and are served as the simplified cardiac fiber architecture. This approach is still inherent in the seeding problem as it employs the streamlining tractography algorithm.

In this work, we propose a fiber oriented approach for providing simplified cardiac fiber architecture. Fibers are first generated on DW data set, and are taken as input of a fiber merging process. In the fiber merging process, we first define a grid with a grid size representing the scale at which we would like to simplify the fiber architecture. Then we find and merge the common fiber segments between fibers with the aide of the grid. Finally we connect fiber segments into longer fibers to obtain the simplified fiber architecture.

6.4 Method

6.4.1 Fiber representation

A fiber can be modeled as a sequence of points (see Fig. 6.1). We use the notation $\mathbf{X}^{(p)} = \{\mathbf{x}_1^{(p)}, ..., \mathbf{x}_{n^{(p)}}^{(p)}\}$ for such a fiber tract, where $p \in \{1, ..., N_f\}$ designates the p-th fiber with N_f representing the total number of fibers we process, and $n^{(p)}$ is the number of fiber points that form the p-th fiber.

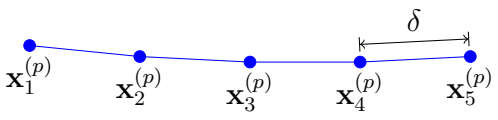

Figure 6.1: A fiber tract $\mathbf{X}^{(p)}$ is represented by a sequence of points. The distance between any two adjacent points is fixed to be a constant, δ, and is referred to as step length.

6.4.2 Grid cell mapping

We define a three-dimentional cell grid set $\boldsymbol{C} = \{\mathbf{c}\}$, with $\mathbf{s} = [s_x, s_y, s_z]'$ denoting the size of each cell in x, y, and z dimension. We set $\mathbf{s}$ according to the voxel size of DW data set $\mathbf{v}$ with a scale factor d

$$\mathbf{s} = d\mathbf{v}. \tag{6.1}$$

When $\mathbf{s}$ is equal to the data spacing (with $d = 1$), the grid cell set is analogous to the set of data voxel.

We define a map $f : \mathbf{x} \to \mathbf{c}$, which finds the cell $\mathbf{c}$ of a fiber point $\mathbf{x}$,

$$f(\mathbf{x}) = \lfloor \mathbf{S}\mathbf{x} \rfloor, \tag{6.2}$$

where $\lfloor\rfloor$ is the floor function that maps a real number to the largest previous integer, and

$$\mathbf{S} = \begin{bmatrix} \frac{1}{s_x} & & \\ & \frac{1}{s_y} & \\ & & \frac{1}{s_z} \end{bmatrix}. \tag{6.3}$$

By performing (6.2) point by point along a fiber $\mathbf{X}^{(p)}$, we obtain an ordered sequence of cells $\mathbf{C}^{(p)} = \{\mathbf{c}_1, ..., \mathbf{c}_{n^{(p)}}\}$, namely a "cell-fiber". Fig 6.2 illustrates the mapping (6.2) for two fibers $\mathbf{X}^{(p)}$ and $\mathbf{X}^{(q)}$.

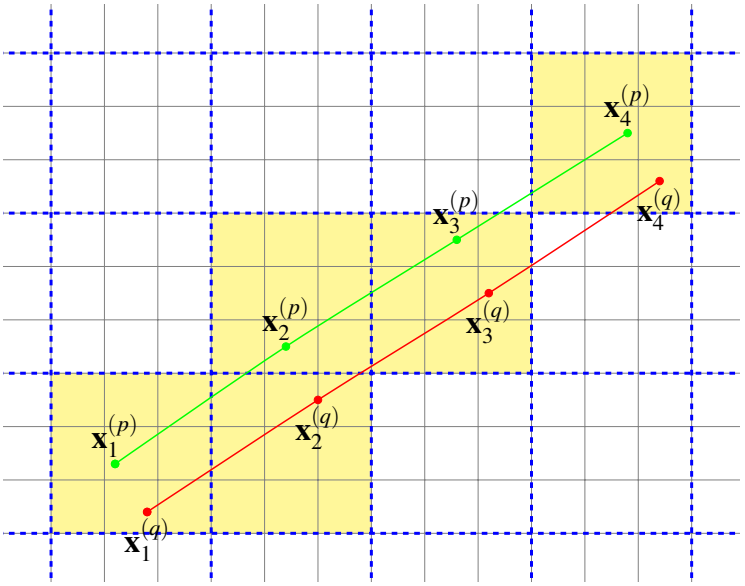

Figure 6.2: The cell mapping of two fibers $\mathbf{X}^{(p)}$ and $\mathbf{X}^{(q)}$: $\mathbf{C}^{(p)} = \{\mathbf{c}_{11}, \mathbf{c}_{22}, \mathbf{c}_{32}, \mathbf{c}_{43}\}$, and $\mathbf{C}^{(q)} = \{\mathbf{c}_{11}, \mathbf{c}_{21}, \mathbf{c}_{32}, \mathbf{c}_{43}\}$, denoted by the yellow blocks. The gray lines denotes the data voxel grid. The dashed blue lines indicate the cell grid, with $d = 3$.

6.4.3 Common cell-fiber segment between fibers

After obtaining the grid mapping $\mathbf{C}^{(p)}$ and $\mathbf{C}^{(q)}$ of fibers $\mathbf{X}^{(p)}$ and $\mathbf{X}^{(q)}$, we find the common cell-fiber segments between them

$$\mathbf{C}^{(p,q)} = \mathbf{C}^{(p)} \cap \mathbf{C}^{(q)} \tag{6.4}$$

And we denote the corresponding original fiber segments along fiber $\mathbf{X}^{(p)}$ as $\mathbf{X}_{c,q}^{(p)}$, and the one along fiber $\mathbf{X}^{(q)}$ as $\mathbf{X}_{c,p}^{(q)}$.

In Fig 6.2, for the fibers $\mathbf{X}^{(p)}$ and $\mathbf{X}^{(q)}$, we have $\mathbf{C}^{(p)} = \{\mathbf{c}_{11}, \mathbf{c}_{22}, \mathbf{c}_{32}, \mathbf{c}_{43}, \}$, and $\mathbf{C}^{(q)} = \{\mathbf{c}_{11}, \mathbf{c}_{21}, \mathbf{c}_{32}, \mathbf{c}_{43}, \}$, and $\mathbf{C}^{(p,q)} = \{\mathbf{c}_{11}\} \bigcup \{\mathbf{c}_{32}, \mathbf{c}_{43}\}$. Notice that $\mathbf{C}^{(p,q)}$ is composed of two segments $\{\mathbf{c}_{11}\}$ and $\{\mathbf{c}_{32}, \mathbf{c}_{43}\}$, because the grid cell mappings of $\mathbf{x}_2^{(p)}$ and $\mathbf{x}_2^{(q)}$ are different. We say that there is a "first-order discontinuity" in $\mathbf{C}^{(p,q)}$. That is, we define the order of discontinuity as the number of different cell mappings.

In our merging process, we break a fiber into segments when the order of discontinuity is second or above (we ignore the first order discontinuity). In the case of Fig 6.2, we consider that $\mathbf{x}_2^{(p)}$ and $\mathbf{x}_2^{(q)}$ fall in the same grid cell.

6.4.4 Similarity between fiber segments

We define similarity between two fiber segments $\mathbf{X}_{c,q}^{(p)}$ and $\mathbf{X}_{c,p}^{(q)}$ as a function of the average of dot product of step directions $\mathbf{v}_i^{(p)}$ and $\mathbf{v}_i^{(q)}$.

$$E(\mathbf{X}_{c,p}^{(q)}, \mathbf{X}_{c,p}^{(q)}) = \arccos \frac{1}{n} \sum_{i=1}^{n} | < \mathbf{v}_i^{(p)}, \mathbf{v}_i^{(q)} > |, \tag{6.5}$$

where n is the number of elements of set $\mathbf{C}^{(p,q)}$.

6.4.5 Merging fiber segments

If the similarity of two fiber segments is above a threshold E-th=10°, we average them grid wise according to $\mathbf{C}^{(p,q)}$. A new fiber points $\overline{\mathbf{x}}$ for cell $\mathbf{c} \in \mathbf{C}^{(p,q)}$ is obtained by averaging the fiber points in $\{\mathbf{x} | \mathbf{x} \in \mathbf{X}_{c,q}^{(p)} \cup \mathbf{X}_{c,p}^{(q)}, f(\mathbf{x}) = \mathbf{c}\}$.

The new average fiber segment and the non common fiber segments are treated as new fibers for further averaging. We continue the merging process until there is no common grid segments between any two fibers.

6.4.6 Connect fibers

After the merging process, we connect two short fibers into longer one if the fiber segments meet each other end to end in one grid cell, and the angle change of the two fiber step directions is bellow a threshold θ-th=30°. In Fig. 6.3 we illustrate the condition in which we connect two fiber segments.

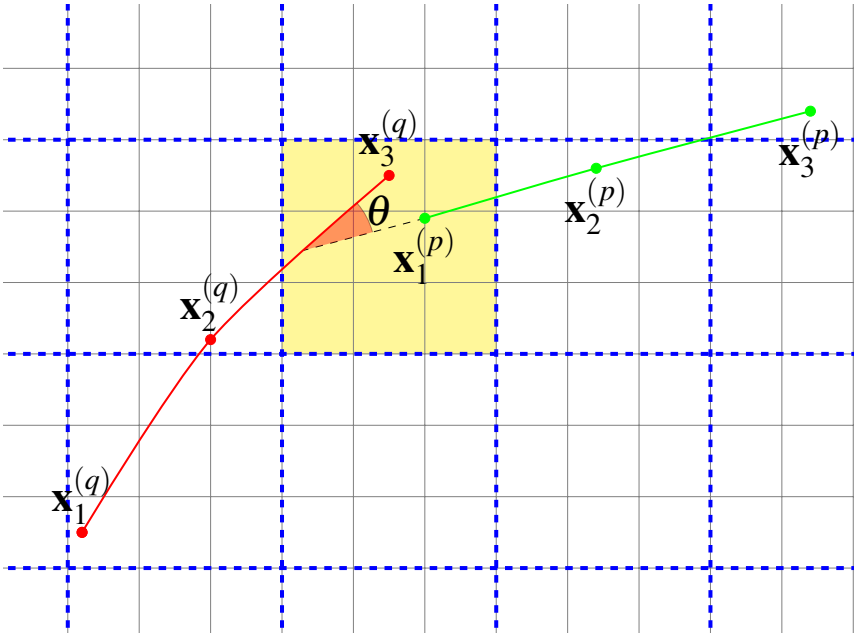

Figure 6.3: Conditions for connecting two fiber segments. Fibers meeting in the same grid cell are connected if the angle θ that indicates the direction change is bellow a threshold θ-th=30°.

6.5 Results

Fig. 6.5 to 6.7 show the merging results with different scale factors. Original fibers are selected by a set of points lying on the xy plan (see Fig. 6.4). Table 6.1 shows statistic on total number of voxels that contains fibers, and the average number of fibers passing these voxels.

After merging, the number of fibers is much smaller, and merging results obtained with large scale factor highlight the global cardiac fiber architecture.

Table 6.1: Statistic N_v and N_f on original fibers and merged fibers with different scale factors. N_v, total number of voxels that have fibers passing; N_v, number of fibers per voxel.

scale	original	1	1/2	1/4	1/8
N_f	9.3343	3.2418	1.4017	1.1109	1.1363
N_v	3422	2601	1439	559	433

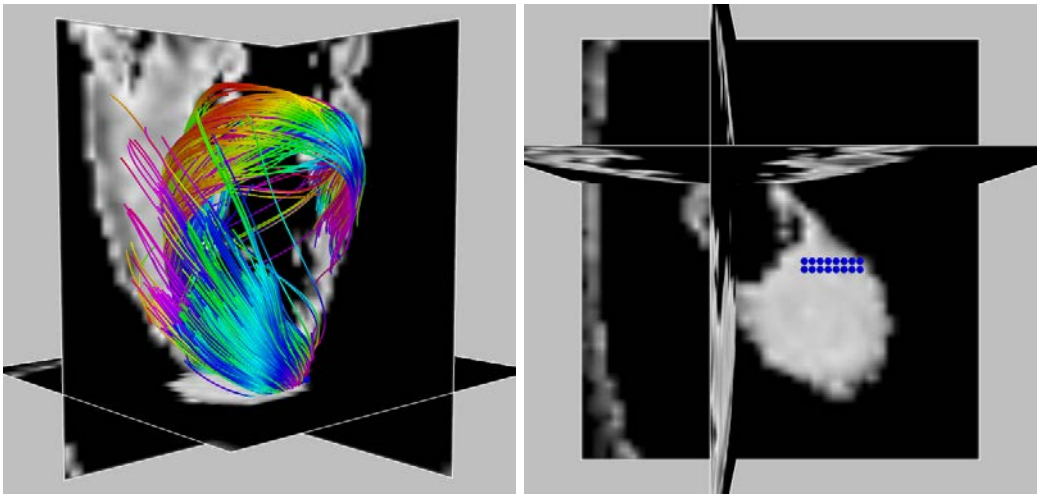

(a) (b)

Figure 6.4: Fibers in (a) are selected by sixteen points of interest, which are indicated in (b) by the blue points.

6.6 Conclusion

In this work, we propose a fiber merging approach which provides multi-scale simplified cardiac fiber architecture by averaging common fiber point sequences according to a predefined grid. Our merging approach takes fiber tracts as input, and provides merged fiber tracts as output. It does not make specific assumption on tractography algorithms, and the only requirement is that the tractography provides fibers in the form of points sequences, which is normally true.

Experimental results show that it is easier to observe main fiber architecture with the proposed fiber merging approach. The size of grid cell d is a parameter for controlling the scale at which we merge fibers. When d equals the size of the data voxel, the merged fibers are at the same scale as original fibers, and represent the same fiber architecture as the original fibers but with redundant fibers averaged. Merging fibers at larger scale provides a fiber representation that highlights more global configuration of cardiac fiber architecture.

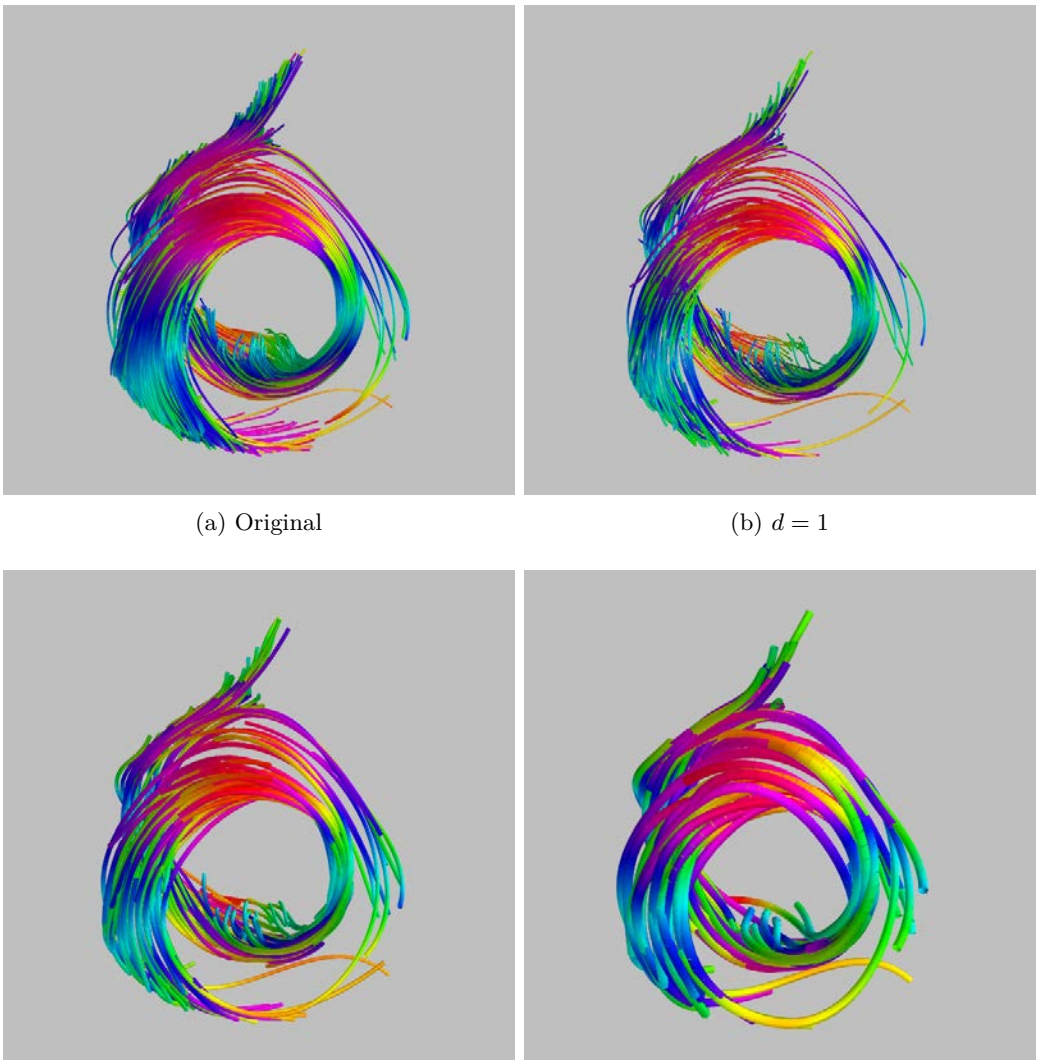

(a) Original (b) $d = 1$

(c) $d = 2$ (d) $d = 4$

Figure 6.5: Merging results viewed from apex.

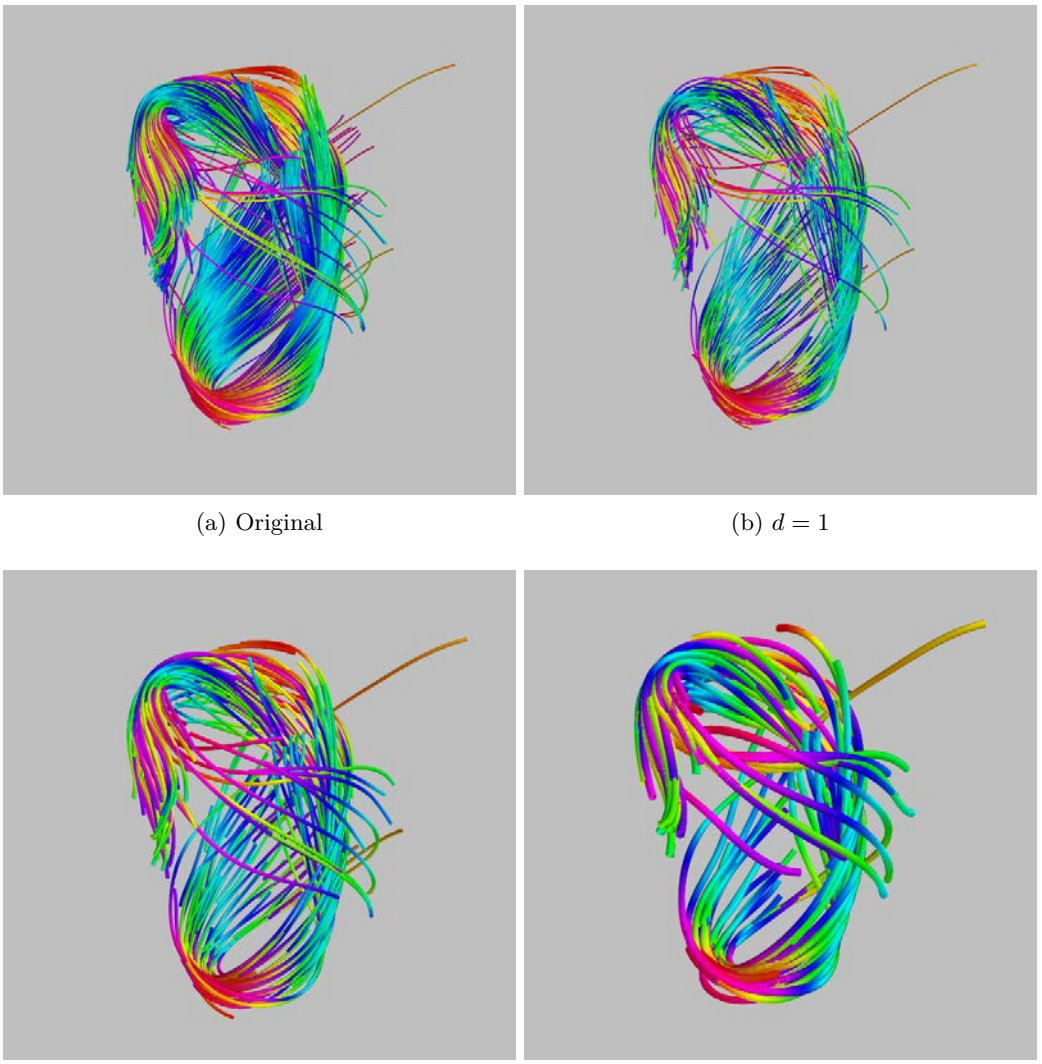

(a) Original (b) $d = 1$

(c) $d = 2$ (d) $d = 4$

Figure 6.6: The same merging results as in Fig. 6.5, but with a different viewing angle.

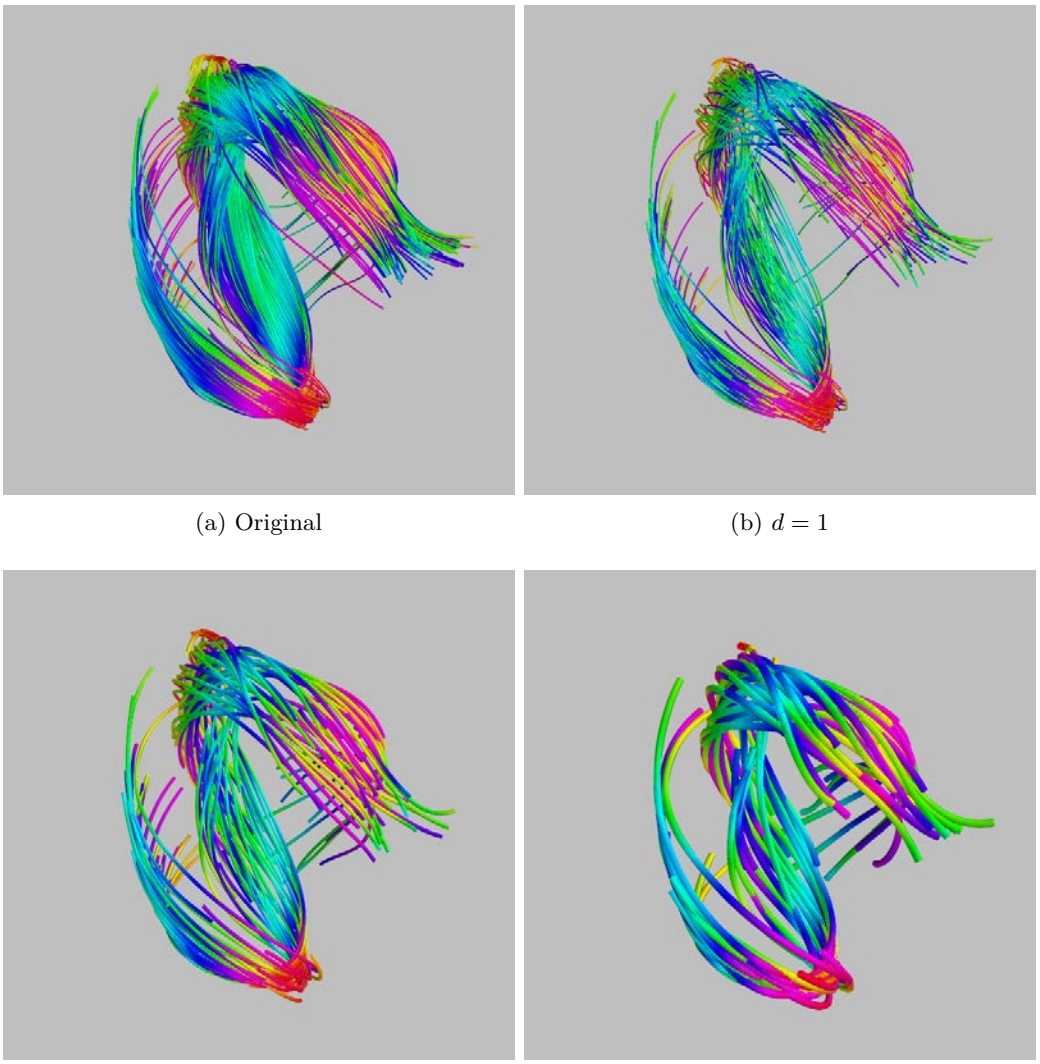

(a) Original (b) $d = 1$

(c) $d = 2$ (d) $d = 4$

Figure 6.7: The same merging results as in Fig. 6.5, but with a different viewing angle.

In the current implementation, fibers are merged pair-wise (i.e., two by two), another alternative approach may first find similar fibers and then merge them in a group-wise manner. In the step of connecting fibers, further improvements could be made by connecting using global optimization according to DW data set.

Chapter 7

Conclusion and perspectives

7.1 Synthesis of contributions

The research work presented in this thesis deals with the tracking of fibers and the description of cardiac fiber architecture from fiber tracts provided by tractography process.

Our first contribution is the development of a probabilistic tractography algorithm. In the tracking process, the proposed algorithm exploits spatial correlation to better account for data uncertainty in human cardiac DTI data. The method is based on the estimation of a weighted mean likelihood over the spatial neighborhood of the current fiber position. Experimental results on both synthetic and real human cardiac DTI data showed that the proposed method is significantly more robust to noise than the streamlining method, and that it produces more regular and smoother fibers, which enables cardiac fiber configurations to be more clearly observed.

Our second contribution is the proposition of a new framework, cardiac fiber unfolding, to describe the complex 3D fiber architecture of the human heart. Our framework takes three-dimensional (3D) fibers as inputs and generates two-dimensional (2D) curves, the embedding, as outputs. It is an isometric mapping achieved by maximizing the total squared point distance under the local fiber isometry constraints. After unfolding, the geodesic distance between original fiber points can be directly calculated by Euclidean distance on the 2D plan. Our fiber unfolding framework allows for the quantitative description of 3D cardiac fiber architecture in a 2D plan. We found that there exist several

cardiac fiber patterns, and that these fiber patterns can be observed more easily after unfolding them in a plane.

Our third contribution is about fiber architecture simplification. We propose a fiber merging approach which provides simplified cardiac fiber architecture at different scales. The simplified fiber architecture highlights global fiber configuration and facilitates both the qualitative and quantitative analysis of cardiac fiber architecture.

Our contributions on cardiac fiber unfolding and fiber merging are two generic post-processing methods on fiber tracts, and they do not rely on any particular tractography algorithm.

7.2 Discussion and perspectives

7.2.1 Cardiac tractography

Is it time to say *"The king is dead, long live the king!"* (originally in French: *"Le roi est mort, vive le roi!"*)?

It has been more than ten years since the proposition of the first tractography in neuroimaging and about ten years since the first cardiac tractography experiment. We have been following the general process of tractography both in neuroimaging and cardiac imaging: calculate local fiber orientations from DWI; connect local fiber orientations into fiber tracts. In recent developments of cardiac diffusion MRI, many efforts were made in improving image quality in in vivo DTI and developing tractography algorithms to better reconstruct fibers, but there are few studies on the description of cardiac fiber architecture, which however should be the ultimate goal of cardiac DTI studies.

We may say "long live the king", because cardiac diffusion MRI study is not just about visualizing cardiac fibers, and is more about learning the heart structure and function. But "the king is not dead", because in attempt to describe cardiac fiber architecture, one question in cardiac tractography arises and even takes our back to the starting point: are 3D curves reasonable for representing cardiac fiber architecture?

7.2.2 Fiber unfolding

The unfolding framework provide a window for studying fiber architecture in 2D. It facilitate the visualization of the cardiac fiber architecture. After unfolding, geodesic distance between original fiber points is directly accessible from the Euclidean distance in 2D. Thus the unfolding framework also provides a quantitative assessment of fiber architecture, For example, we can calculate distance map of fiber points, and define fiber similarity on the embedding.

Studying the architecture of epicardium fibers in 2D would directly have benefits for the designing of biomedical textiles such as heart support devices. When in vivo cardiac diffusion MRI is possible, it would also be useful in studying fiber pattern change during heart circle.

7.2.3 Fiber merging

A simplified representation is necessary in learning the cardiac fiber architecture. Our fiber-wise simplification approach can provide simplified fiber architecture at different scales, and thus it serves as a uniform tool for studying fiber architecture from imaging resolution scale to macro scale.

7.3 Publications

- **Hongying Li**, Marc Robini, Feng Yang, Pierre Croisille, Isabelle Magnin, Yuemin Zhu. Cardiac fiber unfolding by manifold learning. IEEE Transactions on Biomedical Engineering, submitted.
- **Li, H.**, Robini, M., Yang, F., and Zhu, Y. (2012). A neighborhood-based probabilistic approach for fiber tracking in human cardiac DTI. In 2012 9th IEEE International Symposium on Biomedical Imaging (ISBI), pages 9 –13.
- Wang, L., Zhu, Y., **Li, H.**, Liu, W., and Magnin, I. (2012). Multiscale modeling and simulation of the cardiac fiber architecture for DMRI. IEEE Transactions on Biomedical Engineering, 59(1):16 –19.
- Wang, L., Zhu, Y.-M., **Li, H.**, Liu, W., and Magnin, I. E. (2011). Simulation of diffusion anisotropy in DTI for virtual cardiac fiber structure. Functional Imaging and Modeling of the Heart, volume 6666, pages 95–104. Springer Berlin Heidelberg, Berlin, Heidelberg.

Bibliography

[Anderson *et al.* (2009)] Anderson, R. H., Smerup, M., Sanchez-Quintana, D., Loukas, M., and Lunkenheimer, P. P. (2009). The three-dimensional arrangement of the myocytes in the ventricular walls. *Clinical Anatomy*, 22(1):64–76.

[Arsigny *et al.* (2005)] Arsigny, V., Fillard, P., Pennec, X., and Ayache, N. (2005). Fast and simple calculus on tensors in the log-euclidean framework. In *Medical Image Computing and Computer-Assisted Intervention–MICCAI 2005*, page 115–122. Springer.

[Basser (1998)] Basser, P. J. (1998). Fiber-tractography via diffusion tensor MRI (DT-MRI). In *Proceedings of the 6th Annual Meeting ISMRM, Sydney, Australia*, volume 1226.

[Basser *et al.* (1994)] Basser, P. J., Mattiello, J., and LeBihan, D. (1994). Estimation of the effective self-diffusion tensor from the NMR spin echo. *Journal of Magnetic Resonance. Series B*, 103(3):247–254. PMID: 8019776.

[Basser *et al.* (2000)] Basser, P. J., Pajevic, S., Pierpaoli, C., Duda, J., and Aldroubi, A. (2000). In vivo fiber tractography using DT-MRI data. *Magnetic Resonance in Medicine*, 44(4):625–632.

[Basser and Le Bihan (1992)] Basser, P. J. and Le Bihan, D. (1992). Fiber orientation mapping in an anisotropic medium with NMR diffusion spectroscopy. In *11th Annual Meeting of the SMRM, Berlin*, volume 1221.

[Batchelor *et al.* (2006)] Batchelor, P. G., Calamante, F., Tournier, J.-D., Atkinson, D., Hill, D. L. G., and Connelly, A. (2006). Quantification of the shape of fiber tracts. *Magnetic Resonance in Medicine*, 55(4):894–903.

[Behrens *et al.* (2003)] Behrens, T. E. J., Woolrich, M. W., Jenkinson, M., Johansen-Berg, H., Nunes, R. G., Clare, S., Matthews, P. M., Brady, J. M., and Smith, S. M. (2003). Characterization and propagation of uncertainty in diffusion-weighted MR imaging. *Magnetic Resonance in Medicine*, 50(5):1077–1088.

[Behrens and Jbabdi (2009)] Behrens, T. E. and Jbabdi, S. (2009). Chapter 15 - MR diffusion tractography. In Heidi Johansen-Berg and Timothy E.J. Behrens, editors, *Diffusion MRI*, pages 333–351. Academic Press, San Diego.

[Belkin and Niyogi (2001)] Belkin, M. and Niyogi, P. (2001). Laplacian eigenmaps and spectral techniques for embedding and clustering. *Advances in neural information processing systems*, 14:585–591.

[Brown (1828)] Brown, R. (1828). XXVII. a brief account of microscopical observations made in the months of june, july and august 1827, on the particles contained in the

pollen of plants; and on the general existence of active molecules in organic and inorganic bodies. *Philosophical Magazine Series 2*, 4(21):161–173.

[Cayton (2005)] Cayton, L. (2005). Algorithms for manifold learning. *University of California, San Diego, Tech. Rep. CS2008-0923*.

[Celebi *et al.* (2010)] Celebi, A. S., Yalcin, H., and Yalcin, F. (2010). Current cardiac imaging techniques for detection of left ventricular mass. *Cardiovascular Ultrasound*, 8(1):19. PMID: 20515461.

[Chavhan (2007)] Chavhan, G. B. (2007). *MRI Made Easy*. Anshan Publishing.

[Chen *et al.* (2003)] Chen, J., Song, S.-K., Liu, W., McLean, M., Allen, J. S., Tan, J., Wickline, S. A., and Yu, X. (2003). Remodeling of cardiac fiber structure after infarction in rats quantified with diffusion tensor MRI. *American Journal of Physiology - Heart and Circulatory Physiology*, 285(3):H946 –H954.

[Cheng *et al.* (2012)] Cheng, H., Wang, Y., Sheng, J., Sporns, O., Kronenberger, W. G., Mathews, V. P., Hummer, T. A., and Saykin, A. J. (2012). Optimization of seed density in DTI tractography for structural networks. *Journal of Neuroscience Methods*, 203(1):264–272.

[Chung *et al.* (2007)] Chung, C.-Y., Bien, H., and Entcheva, E. (2007). The role of cardiac tissue alignment in modulating electrical function. *Journal of cardiovascular electrophysiology*, 18(12):1323–1329.

[Conturo *et al.* (1999)] Conturo, T. E., Lori, N. F., Cull, T. S., Akbudak, E., Snyder, A. Z., Shimony, J. S., McKinstry, R. C., Burton, H., and Raichle, M. E. (1999). Tracking neuronal fiber pathways in the living human brain. *Proceedings of the National Academy of Sciences*, 96(18):10422 –10427.

[Cook *et al.* (2004)] Cook, P. A., Alexander, D. C., and Parker, G. J. (2004). Modelling noise-induced fibre-orientation error in diffusion-tensor MRI. In *Biomedical Imaging: Nano to Macro, 2004. IEEE International Symposium on*, page 332–335.

[Dietrich *et al.* (2007)] Dietrich, O., Raya, J. G., Reeder, S. B., Reiser, M. F., and Schoenberg, S. O. (2007). Measurement of signal-to-noise ratios in MR images: Influence of multichannel coils, parallel imaging, and reconstruction filters. *Journal of Magnetic Resonance Imaging*, 26(2):375–385.

[Dou *et al.* (2002)] Dou, J., Reese, T. G., Tseng, W.-Y. I., and Wedeen, V. J. (2002). Cardiac diffusion MRI without motion effects. *Magnetic Resonance in Medicine*, 48(1):105–114.

[Einstein (1956)] Einstein, A. (1956). *Investigations on the Theory of the Brownian Movement*. Courier Dover Publications.

[Fick (1855)] Fick, A. (1855). V. on liquid diffusion. *The London, Edinburgh, and Dublin Philosophical Magazine and Journal of Science*, 10(63):30–39.

[Fillard *et al.* (2009)] Fillard, P., Poupon, C., and Mangin, J. F. (2009). A novel global tractography algorithm based on an adaptive spin glass model. *Medical Image Computing and Computer-Assisted Intervention–MICCAI 2009*, page 927–934.

[Fillard *et al.* (2011)] Fillard, P., Descoteaux, M., Goh, A., Gouttard, S., Jeurissen, B., Malcolm, J., Ramirez-Manzanares, A., Reisert, M., Sakaie, K., Tensaouti, F., Yo, T.,

Mangin, J.-F., and Poupon, C. (2011). Quantitative evaluation of 10 tractography algorithms on a realistic diffusion MR phantom. *NeuroImage*, In Press, Uncorrected Proof.

[Friman *et al.* (2006)] Friman, O., Farnebäck, G., and Westin, C.-F. (2006). A bayesian approach for stochastic white matter tractography. *IEEE Transactions on Medical Imaging*, 25(8):965–978. PMID: 16894991.

[Friman and Westin (2005)] Friman, O. and Westin, C.-F. (2005). Uncertainty in white matter fiber tractography. *Medical Image Computing and Computer-Assisted Intervention: MICCAI ... International Conference on Medical Image Computing and Computer-Assisted Intervention*, 8(Pt 1):107–114. PMID: 16685835.

[Frindel *et al.* (2009)a] Frindel, C., Robini, M., Croisille, P., and Zhu, Y. (2009a). Comparison of regularization methods for human cardiac diffusion tensor MRI. *Medical Image Analysis*, 13(3):405–418.

[Frindel *et al.* (2009)b] Frindel, C., Robini, M., Schaerer, J., Croisille, P., and Zhu, Y.-M. (2009b). Cardiac fibre trace clustering for the interpretation of the human heart architecture. In Ayache, N., Delingette, H., and Sermesant, M., editors, *Functional Imaging and Modeling of the Heart*, number 5528 in Lecture Notes in Computer Science, pages 39–48. Springer Berlin Heidelberg.

[Frindel *et al.* (2010)] Frindel, C., Robini, M., Schaerer, J., Croisille, P., and Zhu, Y.-M. (2010). A graph-based approach for automatic cardiac tractography. *Magnetic Resonance in Medicine*, 64(4):1215–1229.

[Garrido *et al.* (1994)] Garrido, L., Wedeen, V. J., Kwong, K. K., Spencer, U. M., and Kantor, H. L. (1994). Anisotropy of water diffusion in the myocardium of the rat. *Circulation Research*, 74(5):789–793.

[Garth *et al.* (2007)] Garth, C., Gerhardt, F., Tricoche, X., and Hagen, H. (2007). Efficient computation and visualization of coherent structures in fluid flow applications. *Visualization and Computer Graphics, IEEE Transactions on*, 13(6):1464–1471.

[Gilbert *et al.* (2007)] Gilbert, S. H., Benson, A. P., Li, P., and Holden, A. V. (2007). Regional localisation of left ventricular sheet structure: integration with current models of cardiac fibre, sheet and band structure. *Eur J Cardiothorac Surg*, 32(2):231–249.

[Helm *et al.* (2005)] Helm, P., Beg, M. F., Miller, M. I., and Winslow, R. L. (2005). Measuring and mapping cardiac fiber and laminar architecture using diffusion tensor MR imaging. *Annals of the New York Academy of Sciences*, 1047:296–307. PMID: 16093505.

[Hlawatsch *et al.* (2011)] Hlawatsch, M., Vollrath, J. E., Sadlo, F., and Weiskopf, D. (2011). Coherent structures of characteristic curves in symmetric second order tensor fields. *IEEE Transactions on Visualization and Computer Graphics*, 17(6):781–794.

[Hlawitschka *et al.* (2010)] Hlawitschka, M., Garth, C., Tricoche, X., Kindlmann, G., Scheuermann, G., Joy, K., and Hamann, B. (2010). Direct visualization of fiber information by coherence. *International journal of computer assisted radiology and surgery*, 5(2):125–131.

[Hsu *et al.* (1998)] Hsu, E. W., Muzikant, A. L., Matulevicius, S. A., Penland, R. C., and Henriquez, C. S. (1998). Magnetic resonance myocardial fiber-orientation mapping with

direct histological correlation. *American Journal of Physiology - Heart and Circulatory Physiology*, 274(5):H1627–H1634.

[Iturria-Medina *et al.* (2007)] Iturria-Medina, Y., Canales-Rodríguez, E., Melie-García, L., Valdés-Hernández, P., Martínez-Montes, E., Alemán-Gómez, Y., and Sánchez-Bornot, J. (2007). Characterizing brain anatomical connections using diffusion weighted MRI and graph theory. *NeuroImage*, 36(3):645–660.

[Jbabdi *et al.* (2007)] Jbabdi, S., Woolrich, M., Andersson, J., and Behrens, T. (2007). A bayesian framework for global tractography. *NeuroImage*, 37(1):116–129.

[Jolliffe (2005)] Jolliffe, I. (2005). *Principal component analysis*. Wiley Online Library.

[Jones (2003)] Jones, D. K. (2003). Determining and visualizing uncertainty in estimates of fiber orientation from diffusion tensor MRI. *Magnetic Resonance in Medicine*, 49(1):7–12.

[Jones (2010)] Jones, D. K. (2010). Challenges and limitations of quantifying brain connectivity in vivo with diffusion MRI. *Imaging*, 2(3):341–355.

[Jones and Pierpaoli (2005)] Jones, D. K. and Pierpaoli, C. (2005). Confidence mapping in diffusion tensor magnetic resonance imaging tractography using a bootstrap approach. *Magnetic Resonance in Medicine*, 53(5):1143–1149.

[Jouk *et al.* (1995)] Jouk, P.-S., Usson, Y., Michalowicz, G., and Parazza, F. (1995). Mapping of the orientation of myocardial cells by means of polarized light and confocal scanning laser microscopy. *Microscopy Research and Technique*, 30(6):480–490.

[Jouk *et al.* (2000)] Jouk, P.-S., Usson, Y., Michalowicz, G., and Grossi, L. (2000). Three-dimensional cartography of the pattern of the myofibres in the second trimester fetal human heart. *Anatomy and Embryology*, 202(2):103–118.

[Kingsley (2006)a] Kingsley, P. B. (2006a). Introduction to diffusion tensor imaging mathematics: Part II. anisotropy, diffusion-weighting factors, and gradient encoding schemes. *Concepts in Magnetic Resonance Part A*, 28(2):123–154.

[Kingsley (2006)b] Kingsley, P. B. (2006b). Introduction to diffusion tensor imaging mathematics: Part III. tensor calculation, noise, simulations, and optimization. *Concepts in Magnetic Resonance Part A*, 28(2):155–179.

[Kocica *et al.* (2006)] Kocica, M. J., Corno, A. F., Carreras-Costa, F., Ballester-Rodes, M., Moghbel, M. C., Cueva, C. N., Lackovic, V., Kanjuh, V. I., and Torrent-Guasp, F. (2006). The helical ventricular myocardial band: global, three-dimensional, functional architecture of the ventricular myocardium. *European Journal of Cardio-thoracic Surgery*, 29(Suppl 1):S21.

[Lazar *et al.* (2003)] Lazar, M., Weinstein, D. M., Tsuruda, J. S., Hasan, K. M., Arfanakis, K., Meyerand, M. E., Badie, B., Rowley, H. A., Haughton, V., Field, A., *et al.* (2003). White matter tractography using diffusion tensor deflection. *Human Brain Mapping*, 18:306–321.

[Lazar and Alexander (2003)] Lazar, M. and Alexander, A. L. (2003). An error analysis of white matter tractography methods: synthetic diffusion tensor field simulations. *Neuroimage*, 20(2):1140–1153.

[Lazar and Alexander (2005)] Lazar, M. and Alexander, A. L. (2005). Bootstrap white matter tractography (BOOT-TRAC). *NeuroImage*, 24(2):524–532.

[Le Bihan *et al.* (1986)] Le Bihan, D., Breton, E., Lallemand, D., Grenier, P., Cabanis, E., and Laval-Jeantet, M. (1986). MR imaging of intravoxel incoherent motions: application to diffusion and perfusion in neurologic disorders. *Radiology*, 161(2):401–407.

[Li *et al.* (2012)] Li, H., Robini, M., Yang, F., and Zhu, Y. (2012). A neighborhood-based probabilistic approach for fiber tracking in human cardiac DTI. In *2012 9th IEEE International Symposium on Biomedical Imaging (ISBI)*, pages 9 –13.

[Lombaert *et al.* (2012)] Lombaert, H., Peyrat, J.-M., Croisille, P., Rapacchi, S., Fanton, L., Cheriet, F., Clarysse, P., Magnin, I., Delingette, H., and Ayache, N. (2012). Human atlas of the cardiac fiber architecture: study on a healthy population. *IEEE transactions on medical imaging*, 31(7):1436–1447. PMID: 22481815.

[Mangin *et al.* (2002)] Mangin, J.-F., Poupon, C., Cointepas, Y., Rivière, D., Papadopoulos-Orfanos, D., Clark, C. A., Régis, J., and Le Bihan, D. (2002). A framework based on spin glass models for the inference of anatomical connectivity from diffusion-weighted MR data – a technical review. *NMR in Biomedicine*, 15(7-8):481–492.

[Mangin *et al.* (2013)] Mangin, J.-F., Fillard, P., Cointepas, Y., Le Bihan, D., Frouin, V., and Poupon, C. (2013). Towards global tractography. *NeuroImage*.

[Mardia and Jupp (2009)] Mardia, K. V. and Jupp, P. E. (2009). *Directional statistics*, volume 494. Wiley.

[Mathers and Loncar (2006)] Mathers, C. D. and Loncar, D. (2006). Projections of global mortality and burden of disease from 2002 to 2030. *PLoS medicine*, 3(11):e442.

[Mattiello *et al.* (1997)] Mattiello, J., Basser, P. J., and Le Bihan, D. (1997). The b matrix in diffusion tensor echo-planar imaging. *Magnetic resonance in medicine*, 37(2):292–300.

[Mekkaoui *et al.* (2012)] Mekkaoui, C., Huang, S., Chen, H. H., Dai, G., Reese, T. G., Kostis, W. J., Thiagalingam, A., Maurovich-Horvat, P., Ruskin, J. N., Hoffmann, U., Jackowski, M. P., and Sosnovik, D. E. (2012). Fiber architecture in remodeled myocardium revealed with a quantitative diffusion CMR tractography framework and histological validation. *Journal of Cardiovascular Magnetic Resonance*, 14(1):70.

[Mori *et al.* (1999)] Mori, S., Crain, B. J., Chacko, V. P., and Van Zijl, P. C. M. (1999). Three-dimensional tracking of axonal projections in the brain by magnetic resonance imaging. *Annals of Neurology*, 45(2):265–269.

[Mori and van Zijl (2002)] Mori, S. and van Zijl, P. C. M. (2002). Fiber tracking: principles and strategies - a technical review. *NMR in Biomedicine*, 15(7-8):468–480.

[Mukherjee *et al.* (2008)] Mukherjee, P., Chung, S. W., Berman, J. I., Hess, C. P., and Henry, R. G. (2008). Diffusion tensor MR imaging and fiber tractography: technical considerations. *American Journal of Neuroradiology*, 29(5):843.

[Nichols *et al.* (2012)] Nichols, M., Townsend, N., Scarborough, P., Luengo-Fernandez, R., Leal, J., Gray, A., and Rayner, M. (2012). European cardiovascular disease statistics 2012. *European Heart Network, Brussels, European Society of Cardiology, Sophia Antipolis*, page P104.

[Organization (2011)] Organization, W. H. (2011). *Global status report on noncommunicable diseases 2010*. World Health Organization.

[Parker *et al.* (2003)] Parker, G. J., Haroon, H. A., and Wheeler-Kingshott, C. A. (2003). A framework for a streamline-based probabilistic index of connectivity (PICo) using a structural interpretation of MRI diffusion measurements. *Journal of Magnetic Resonance Imaging*, 18(2):242–254.

[Peelers *et al.* (2006)] Peelers, T., Vilanova, A., Strijkerst, G. J., ter Haar Romeny, B. M., Dolech, D., and Eindhoven, N. (2006). Visualization of the fibrous structure of the heart. In *Vision, modeling, and visualization 2006: proceedings, November 22-24, 2006, Aachen, Germany*, page 309.

[Peeters *et al.* (2006)] Peeters, T., Vilanova, A., and ter Haar Romeny, R. B. M. (2006). Visualization of DTI fibers using hair-rendering techniques. In *Proc ASCI*, page 66–73.

[Peeters *et al.* (2009)] Peeters, T. H. J. M., Vilanova, A., and Romeny, B. M. t. H. (2009). Interactive fibre structure visualization of the heart. *Computer Graphics Forum*, 28(8):2140–2150.

[Pipe (2009)] Pipe, J. (2009). Chapter 2 - pulse sequences for diffusion-weighted MRI. In Heidi Johansen-Berg and Timothy E.J. Behrens, editors, *Diffusion MRI*, pages 11–35. Academic Press, San Diego.

[Poveda *et al.* (2011)] Poveda, F., Gil, D., Andaluz, A., and Marti, E. (2011). Multiscale tractography for representing heart muscular architecture. In *Workshop on Computational Diffusion MRI, MICCAI*.

[Poveda *et al.* (2012)] Poveda, F., Martí, E., Gil, D., Carreras, F., and Ballester, M. (2012). Helical structure of ventricular anatomy by diffusion tensor cardiac MR tractography. *JACC: Cardiovascular Imaging*, 5(7):754–755.

[Reese *et al.* (1995)] Reese, T. G., Weisskoff, R. M., Smith, R. N., Rosen, B. R., Dinsmore, R. E., and Wedeen, V. J. (1995). Imaging myocardial fiber architecture in vivo with magnetic resonance. *Magnetic Resonance in Medicine*, 34(6):786–791.

[Reisert *et al.* (2009)] Reisert, M., Mader, I., and Kiselev, V. (2009). Global reconstruction of neuronal fibres. *Diffusion Modeling and Fiber Cup (in MICCAI)*, page 70–81.

[Rohmer *et al.* (2006)a] Rohmer, D., Sitek, A., and Gullberg, G. T. (2006a). Reconstruction and visualization of fiber and sheet structure with regularized tensor diffusion MRI in the human heart.

[Rohmer *et al.* (2006)b] Rohmer, D., Sitek, A., and Gullberg, G. T. (2006b). Visualization of fiber structure in the left and right ventricle of a human heart.

[Rohmer *et al.* (2007)] Rohmer, D., Sitek, A., and Gullberg, G. T. (2007). Reconstruction and visualization of fiber and laminar structure in the normal human heart from ex vivo diffusion tensor magnetic resonance imaging (DTMRI) data. *Investigative Radiology*, 42(11):777–789. PMID: 18030201.

[Roweis and Saul (2000)] Roweis, S. T. and Saul, L. K. (2000). Nonlinear dimensionality reduction by locally linear embedding. *Science*, 290(5500):2323–2326.

[Salvador *et al.* (2005)] Salvador, R., Pena, A., Menon, D. K., Carpenter, T. A., Pickard, J. D., and Bullmore, E. T. (2005). Formal characterization and extension of the linearized diffusion tensor model. *Human brain mapping*, 24(2):144–155.

[Saul and Roweis (2003)] Saul, L. K. and Roweis, S. T. (2003). Think globally, fit locally: unsupervised learning of low dimensional manifolds. *The Journal of Machine Learning Research*, 4:119–155.

[Scollan *et al.* (1998)] Scollan, D. F., Holmes, A., Winslow, R., and Forder, J. (1998). Histological validation of myocardial microstructure obtained from diffusion tensor magnetic resonance imaging. *American Journal of Physiology - Heart and Circulatory Physiology*, 275(6):H2308–H2318.

[Seung and Daniel D. Lee (2000)] Seung, H. S. and Daniel D. Lee (2000). The manifold ways of perception. *Science*, 290(5500):2268–2269.

[Spach *et al.* (1988)] Spach, M. S., Dolber, P. C., and Heidlage, J. F. (1988). Influence of the passive anisotropic properties on directional differences in propagation following modification of the sodium conductance in human atrial muscle. a model of reentry based on anisotropic discontinuous propagation. *Circulation research*, 62(4):811–832.

[Stejskal and Tanner (1965)] Stejskal, E. O. and Tanner, J. E. (1965). Spin diffusion measurements: spin echoes in the presence of a time-dependent field gradient. *The journal of chemical physics*, 42(1):288.

[Stoeck *et al.* (2012)] Stoeck, C. T., Toussaint, N., Boesiger, P., and Kozerke, S. (2012). Dual heart-phase cardiac DTI using local-look STEAM. In *Proc. Intl. Soc. Mag. Reson. Med. 20 (2012)*, page 227.

[Streeter (1979)] Streeter, D. (1979). Gross morphology and fiber geometry of the heart. In Bethesda, B., editor, *Handbook of Physiology: The Cardiovascular System*, volume 1, pages 61–112. American Physiology Society.

[Sun *et al.* (2006)] Sun, J., Boyd, S., Xiao, L., and Diaconis, P. (2006). The fastest mixing markov process on a graph and a connection to a maximum variance unfolding problem. *SIAM review*, 48(4):681–699.

[Taccardi *et al.* (1994)] Taccardi, B., Macchi, E., Lux, R. L., Ershler, P. R., Spaggiari, S., Baruffi, S., and Vyhmeister, Y. (1994). Effect of myocardial fiber direction on epicardial potentials. *Circulation*, 90(6):3076–3090.

[Tenenbaum *et al.* (2000)] Tenenbaum, J. B., De Silva, V., and Langford, J. C. (2000). A global geometric framework for nonlinear dimensionality reduction. *Science*, 290(5500):2319–2323.

[Torrent-Guasp *et al.* (2001)] Torrent-Guasp, F., Ballester, M., Buckberg, G. D., Carreras, F., Flotats, A., Carrió, I., Ferreira, A., Samuels, L. E., and Narula, J. (2001). Spatial orientation of the ventricular muscle band: physiologic contribution and surgical implications. *Journal of thoracic and cardiovascular surgery*, 122(2):389–392.

[Torrent-Guasp *et al.* (2005)] Torrent-Guasp, F., Kocica, M. J., Corno, A. F., Komeda, M., Carreras-Costa, F., Flotats, A., Cosin-Aguillar, J., and Wen, H. (2005). Towards new understanding of the heart structure and function. *European Journal of Cardio-Thoracic Surgery*, 27(2):191–201.

[Tournier *et al.* (2003)] Tournier, J.-D., Calamante, F., Gadian, D. G., and Connelly, A. (2003). Diffusion-weighted magnetic resonance imaging fibre tracking using a front evolution algorithm. *NeuroImage*, 20(1):276–288.

[Tournier *et al.* (2004)] Tournier, J.-D., Calamante, F., Gadian, D. G., and Connelly, A. (2004). Direct estimation of the fiber orientation density function from diffusion-weighted MRI data using spherical deconvolution. *NeuroImage*, 23(3):1176–1185.

[Tournier *et al.* (2011)] Tournier, J.-D., Mori, S., and Leemans, A. (2011). Diffusion tensor imaging and beyond. *Magnetic Resonance in Medicine*, 65(6):1532–1556.

[Toussaint *et al.* (2010)] Toussaint, N., Sermesant, M., Stoeck, C. T., Kozerke, S., and Batchelor, P. G. (2010). In vivo human 3D cardiac fibre architecture: reconstruction using curvilinear interpolation of diffusion tensor images. In *Medical Image Computing and Computer-Assisted Intervention–MICCAI 2010*, page 418–425. Springer.

[Toussaint *et al.* (2013)] Toussaint, N., Stoeck, C. T., Schaeffter, T., Kozerke, S., Sermesant, M., and Batchelor, P. G. (2013). In vivo human cardiac fibre architecture estimation using shape-based diffusion tensor processing. *Medical image analysis*.

[Tseng *et al.* (2006)] Tseng, W. I., Dou, J., Reese, T. G., and Wedeen, V. J. (2006). Imaging myocardial fiber disarray and intramural strain hypokinesis in hypertrophic cardiomyopathy with MRI. *Journal of Magnetic Resonance Imaging*, 23(1):1–8.

[Tuch (2002)] Tuch, D. S. (2002). *Diffusion MRI of complex tissue structure*. Thesis, Massachusetts Institute of Technology. Thesis (Ph. D.)–Harvard–Massachusetts Institute of Technology Division of Health Sciences and Technology, 2002.

[Tuch *et al.* (2003)] Tuch, D. S., Reese, T. G., Wiegell, M. R., and Van J, W. (2003). Diffusion MRI of complex neural architecture. *Neuron*, 40(5):885–895.

[Vandenberghe and Boyd (1996)] Vandenberghe, L. and Boyd, S. (1996). Semidefinite programming. *SIAM review*, 38(1):49–95.

[Van der Maaten *et al.* (2009)] Van der Maaten, L. J. P., Postma, E. O., and Van Den Herik, H. J. (2009). Dimensionality reduction: A comparative review. *Journal of Machine Learning Research*, 10:1–41.

[Varray *et al.* (2013)] Varray, F., Wang, L., Fanton, L., Zhu, Y.-M., and Magnin, I. E. (2013). High resolution extraction of local human cardiac fibre orientations. In *Functional Imaging and Modeling of the Heart*, page 150–157. Springer.

[Vilanova *et al.* (2006)] Vilanova, A., Zhang, S., Kindlmann, G., and Laidlaw, D. (2006). An introduction to visualization of diffusion tensor imaging and its applications. In *Visualization and Processing of Tensor Fields*, page 121–153. Springer.

[Wei *et al.* (2013)] Wei, H., Viallon, M., Delattre, B., Wang, L., Pai, V., Wen, H., Xue, H., Guetter, C., Croisille, P., and Zhu, Y. (2013). Assessment of cardiac motion effects on the fiber architecture of the human heart in vivo. *IEEE transactions on medical imaging*.

[Weinberger and Saul (2004)] Weinberger, K. and Saul, L. (2004). Unsupervised learning of image manifolds by semidefinite programming. In *Proceedings of the 2004 IEEE Computer Society Conference on Computer Vision and Pattern Recognition, 2004. CVPR 2004*, volume 2, pages II–988 – II–995 Vol.2.

[Weinberger and Saul (2006)a] Weinberger, K. Q. and Saul, L. K. (2006a). An introduction to nonlinear dimensionality reduction by maximum variance unfolding. In *Proceedings of the National Conference on Artificial Intelligence*, volume 21, page 1683.

[Weinberger and Saul (2006)b] Weinberger, K. Q. and Saul, L. K. (2006b). Unsupervised learning of image manifolds by semidefinite programming. *International Journal of Computer Vision*, 70(1):77–90.

[Weinstein *et al.* (1999)] Weinstein, D., Kindlmann, G., and Lundberg, E. (1999). Tensorlines: Advection-diffusion based propagation through diffusion tensor fields. In *Proceedings of IEEE Visualization 1999*, page 249–253.

[Westin *et al.* (2002)] Westin, C. F., Maier, S. E., Mamata, H., Nabavi, A., Jolesz, F. A., and Kikinis, R. (2002). Processing and visualization for diffusion tensor MRI. *Medical Image Analysis*, 6(2):93–108.

[Wu *et al.* (2007)] Wu, E. X., Wu, Y., Tang, H., Wang, J., Yang, J., Ng, M. C., Yang, E. S., Chan, C. W., Zhu, S., Lau, C.-P., and Tse, H.-F. (2007). Study of myocardial fiber pathway using magnetic resonance diffusion tensor imaging. *Magnetic Resonance Imaging*, 25(7):1048–1057.

[Wu *et al.* (2009)] Wu, M.-T., Su, M.-Y. M., Huang, Y.-L., Chiou, K.-R., Yang, P., Pan, H.-B., Reese, T. G., Wedeen, V. J., and Tseng, W.-Y. I. (2009). Sequential changes of myocardial microstructure in patients postmyocardial infarction by diffusion-tensor cardiac MR: correlation with left ventricular structure and function. *Circulation. Cardiovascular Imaging*, 2(1):32–40, 6 p following 40. PMID: 19808562.

[Yang *et al.* (2012)] Yang, F., Zhu, Y.-M., Magnin, I. E., Luo, J.-H., Croisille, P., and Kingsley, P. B. (2012). Feature-based interpolation of diffusion tensor fields and application to human cardiac DT-MRI. *Medical Image Analysis*, 16(2):459–481.

[Zalesky (2008)] Zalesky, A. (2008). DT-MRI fiber tracking: a shortest paths approach. *Medical Imaging, IEEE Transactions on*, 27(10):1458–1471.

[Zhang *et al.* (2008)] Zhang, S., Correia, S., and Laidlaw, D. H. (2008). Identifying white-matter fiber bundles in DTI data using an automated proximity-based fiber clustering method. *IEEE transactions on visualization and computer graphics*, 14(5):1044–1053. PMID: 18599916 PMCID: 2757786.

[Zhukov and Barr (2002)] Zhukov, L. and Barr, A. H. (2002). Oriented tensor reconstruction: tracing neural pathways from diffusion tensor MRI. In *IEEE Visualization, 2002. VIS 2002*, pages 387–394. IEEE.

[Zhukov and Barr (2003)] Zhukov, L. and Barr, A. H. (2003). Heart-muscle fiber reconstruction from diffusion tensor MRI. In *Proceedings of the 14th IEEE Visualization 2003 (VIS'03)*, page 79.

[Francisco Torrent-Guasp and Mladen J. Kocica (2006)] Francisco Torrent-Guasp and Mladen J. Kocica (2006). HELICAL VENTRICULAR MYOCARDIAL BAND - DISSECTION TECHNIQUE.

[LeGrice *et al.* (1995)] LeGrice, I. J., Smaill, B. H., Chai, L. Z., Edgar, S. G., Gavin, J. B., and Hunter, P. J. (1995). Laminar structure of the heart: ventricular myocyte arrangement and connective tissue architecture in the dog. *American Journal of Physiology - Heart and Circulatory Physiology*, 269(2):H571 –H582.

[LeGrice *et al.* (2001)] LeGrice, I., Hunter, P., Young, A., and Smaill, B. (2001). The architecture of the heart: a data–based model. *Philosophical Transactions of the Royal Society of London. Series A: Mathematical, Physical and Engineering Sciences*, 359(1783):1217–1232.

[LeGrice *et al.* (2005)] LeGrice, I., Pope, A., and Smaill, B. (2005). The architecture of the heart: Myocyte organization and the cardiac extracellular matrix. In Villarreal, F. J., editor, *Interstitial Fibrosis in Heart Failure*, volume 253, pages 3–21. Springer-Verlag, New York.

[O'Donnell *et al.* (2006)] O'Donnell, L., Kubicki, M., Shenton, M., Dreusicke, M., Grimson, W., and Westin, C. (2006). A method for clustering white matter fiber tracts. *AJNR Am J Neuroradiol*, 27(5):1032–1036.

Folio Administratif
Thèse soutenue devant l'Institut National des Sciences Appliquées de Lyon

Nom : LI **Date de soutenance :** 21 novembre 2013

Prénom : Hongying

Titre : Fiber tracking and fiber architecture description in cardiac DT-MRI

Nature : Doctorat **Numéro d'ordre :** 2013-ISAL-???

École doctorale : École Doctorale Électronique, Électrotechnique, Automatique

Spécialité : Système et Image

Cote B.I.U. Lyon : **Classe :**

Résumé : La connaissance de l'architecture tridimensionnelle (3D) des fibres est cruciale dans la compréhension de la fonction du cœur humain. L'imagerie par résonance magnétique du tenseur de diffusion (IRM-DT) est une technique permettant de mesurer la diffusion des molécules d'eau dans des tissus humains, et donc d'étudier de manière non-invasive l'architecture 3D des fibres du cœur humain. Dans l'IRM-TD cardiaque, la tractographie des fibres est essentielle pour représenter et visualiser l'architecture des fibres, mais souvent utilisée qualitativement comme une dernière étape qui consiste à visualiser sur l'écran l'architecture myocardique obtenue à partir des données IRM-TD. Cependant, cette visualisation qualitative n'est pas suffisante pour décrire de manière objective et complète l'architecture des fibres. L'objectif de cette thèse est de développer de nouvelles approches pour la tractographie et pour la description quantitative de l'architecture des fibres cardiaques du cœur humain en IRM-TD cardiaque.

Les travaux de cette thèse se focalisent sur trois axes. Le premier est le développement d'un algorithme de tractographie probabiliste, qui prend en compte la corrélation spatiale des fibres pendant le suivi des fibres myocardiques. Les résultats expérimentaux montrent que la méthode proposée est robuste au bruit. Les fibres produites sont plus régulières et plus lisses, et la configuration des fibres cardiaques est plus facile à observer. Le second axe concerne une nouvelle notion de dépliement de fibres pour décrire les fibres du cœur humain, qui sont souvent complexes dans l'espace 3D. L'idée est d'analyser cette architecture 3D dans un espace réduit à deux dimensions (2D), en utilisant une technique d'apprentissage de variété. L'approche de dépliement proposée permet la description quantitative de l'architecture 3D de fibres cardiaques dans un plan 2D. Les résultats montrent qu'il est beaucoup plus facile d'observer et d'étudier les caractéristiques des fibres cardiaques après les avoir dépliées, et qu'il semble exister des formes de fibres caractéristiques du cœur humain. Le dernier axe consiste en la fusion de fibres, qui est obtenue en moyennant les fibres selon une grille. Cette approche fournit des architectures de fibres simplifiée à différentes échelles, et permet de mieux mettre en évidence la configuration des fibres cardiaques.

Mots-clés : Imagerie cardiaque, Analyse d'images, IRM du tenseur de diffusion, Fibres cardiaques, Architecture des fibres cardiaques, Tractographie, Apprentissage de variété, Fusion de fibres.

Laboratoire de Recherches : CREATIS (CNRS UMR 5520, INSERM U630)

Directeurs de Thèse : M. Yue-Min ZHU et M. Marc ROBINI

Président du Jury : ??

Composition du Jury : Nicole VINCENT, Michel DESVIGNES, Pierre-Simon JOUK, Yves Usson, Pierre CROISILLE, Isabelle E. MAGNIN, Marc ROBINI, Yue-Min ZHU